

Authors' final response on manuscript "Submesoscale CO₂ variability across an upwelling front off Peru"

Eike E. Köhn¹, Sören Thomsen¹, Damian L. Arévalo-Martínez¹, and Torsten Kanzow²

¹GEOMAR Helmholtz Centre for Ocean Research Kiel, Kiel, Germany

²Alfred-Wegener-Institute Helmholtz Centre for Polar and Marine Research, Bremerhaven, Germany

Correspondence to: Eike E. Köhn (ekoehn@geomar.de)

Dear Editor, dear referees,

we would like to thank you for the evaluation of the manuscript "Submesoscale CO₂ variability across an upwelling front off Peru". We fully appreciate the generally positive feedback from both referees and the fruitful comments helped to improve
5 the manuscript. This document consists of three parts:

1. In the first part you can find our response to every comment brought forward. It is structured in such a way, that a referee's comment is repeated (blue/red font) with our reaction regarding every issue following below (black font). The reaction is split into the authors' response (AR) and the manuscript changes (MC).
2. The second part consists of the revised manuscript version. The stated page and line numbers in part 1 refer to this
10 version.
3. In part 3 another version of the manuscript is provided showing all the changes made in the document using *latexdiff*. These also include some minor changes to improve the readability of the manuscript.

In the revised version of the manuscript the figure order has been changed by moving Fig. 6 in front of Fig. 4. Now the wind evolution is shown as Fig. 4, the CTD transect as Fig. 5 and the Hovmoeller plots as Fig. 6.

Anonymous Referee #1:

Received and published: 28 July 2017

Kohn et al. observe and address the drivers of CO₂ flux variability at small time (hours) and space (km) scales off coastal Peru. Eastern boundary upwelling zones such as this region can be a large source of CO₂ to the atmosphere, so understanding the mechanisms that drive CO₂ flux from these regions is critical to reducing the uncertainty in the global carbon cycle. This paper provides an important contribution to understanding the driving mechanisms of CO₂ flux from eastern boundary upwelling zones, and I recommend publication in *Ocean Sciences* after the authors consider some comments below on methodology clarity and how these results relate to other modeling and observational work.

10 Major comments:

1) Comparison to studies at broader time and space scales: Most observational- and modeling-based studies of CO₂ flux do not constrain the influence of submesoscale processes as done here by Kohn et al. In order to make a stronger connection to existing research and provide valuable insight for future studies, this manuscript would benefit from additional analyses that link small to broader scale processes. For example, Kohn et al. compare their observations to the observations presented by Friederich et al. (2008) for the month of February (in section 6). What is the seasonal context for this comparison, i.e., how does February compare to the range of seasonal patterns in CO₂ flux and wind forcing in this region? Are submesoscale processes more dominant during certain times of year or certain phases of ENSO? In addition, there have been more recent assessments of broad-scale CO₂ flux (Landschützer et al., 2014) that likely utilize more recent underway observations off coastal Peru (Bakker et al., 2014). How do these compare to Friederich et al. and the results presented here? Finally, are there lessons learned as a result of this research on submesoscale processes that may be useful to improving observational design and model parameterizations?

AR: The measurements from the Meteor 93 (M93) research expedition were taken in February 2013, i.e. during austral summer. This period is generally marked by moderate northward wind stress and correspondingly only moderate coastal upwelling. However, the surface Chl-*a* concentrations and cross-shelf temperature gradients are at their maximum during this period (Echevin et al., 2008; Vazquez-Cuervo et al., 2013). The Takahashi et al. (2014) climatology shows all year round elevated surface *p*CO₂ values in the area spanning from the equatorial Pacific to the Peruvian upwelling region (Fig. AR1). During January/February they are at their minimum, while peak surface CO₂ concentrations are observed from August to October. However, the grid (5° in longitude, 4° in latitude) hardly resolves the near-shore region. The increased surface CO₂ concentration and the predominantly oceanic CO₂ outgassing signal (Takahashi et al., 2009) implicate that the Peruvian upwelling regime is an important region for the air-sea CO₂ flux. Only few measurements document the high surface concentrations in the intense coastal upwelling region.

Using the most up to date version of the SOCAT data set (version 3-5) (Bakker et al., 2016) reveals a scarce *f*CO₂ data coverage in the Peruvian upwelling region (Fig. AR2). In fact no data is available for the exact region investigated in our

study. Further, Fig. AR3 shows a general lack of data in certain months, including February, the month corresponding to the period of our study. Based on the SOCAT data, it is still not possible to identify a robust mean surface CO_2 signal, let alone a seasonal pattern in the coastal Peruvian region. The data set presented in Friederich et al. (2008) is unique in its coverage as well as its temporal and spatial resolution. Most of the comparisons are therefore made with respect to their data set. The newly presented climatology of Landschützer et al. (2017) with a 1° resolution (Fig. AR4) is based on the SOCAT data set and yields a comparable $p\text{CO}_2$ pattern as Takahashi et al. (2014). It becomes obvious, that the study area is located at the transition between the high equatorial values and the lower offequatorial concentrations. In Landschützer et al. (2017), the grid point closest to our study region shows a semi-annual cycle in the surface $p\text{CO}_2$ content, with its maximum of $440 \mu\text{atm}$ in April and September (Fig. AR5). In February $p\text{CO}_2$ values are close to the annual average value of about $420 \mu\text{atm}$. However, the scarce data availability in the Peruvian upwelling region shown in Fig. AR3 points towards the large uncertainties associated with the climatology constructed by Landschützer et al. (2017). Further complicating any comparison with the climatology, the conditions observed in our study are not necessarily representative for February. Multiple processes drive the variability in the surface temperature and $f\text{CO}_2$ field in the Peruvian upwelling region in a broad range of timescales. In February 2013 the Pacific Ocean was governed by neutral to weak La Niña conditions, associated with a moderately strong upwelling front. These conditions are found to enhance CO_2 outgassing in the eastern equatorial Pacific (Feely et al., 2006; Landschützer et al., 2014), and to affect air-sea fluxes in other ocean basins as well (Lefèvre et al. 2013). The impact of the El Niño Southern

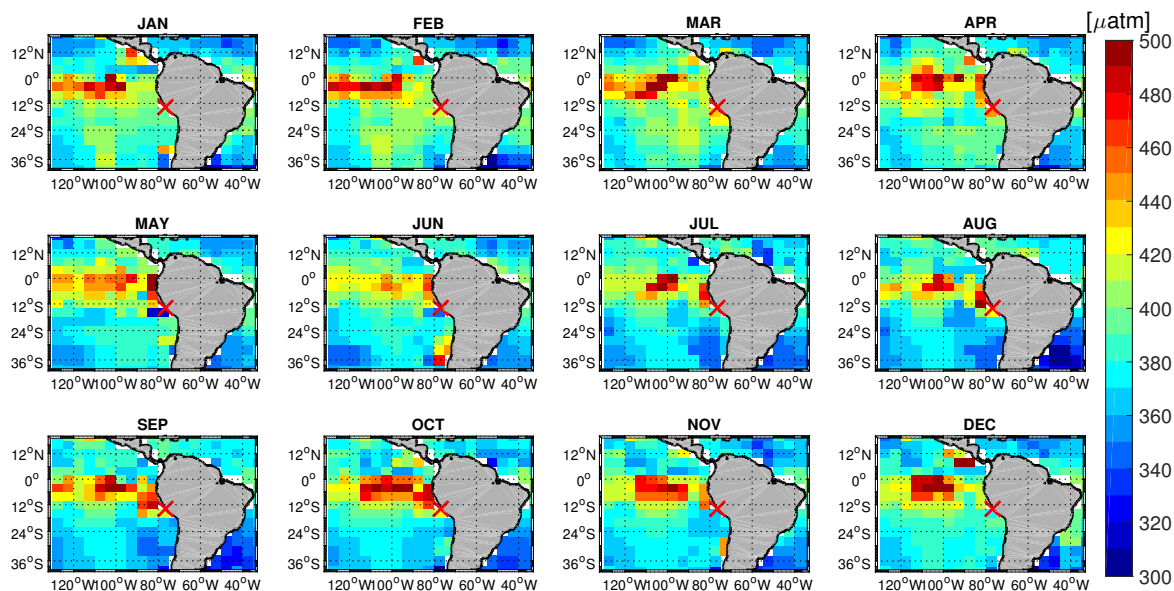


Figure AR1. Monthly $p\text{CO}_2$ climatology of Takahashi et al. (2014) on a $5^\circ \times 4^\circ$ grid in μatm . The red cross shows the location of our study area.

Oscillation (ENSO) on the near-shore CO₂ fluxes in the Peruvian upwelling region is still somewhat obscured. Further, the propagation of coastally trapped waves (Pietri et al., 2014) or the curl and variability of the near-coastal wind field (Albert et al., 2010) can largely impact the situation off the coast of Peru. As shown in our study, the location and movement of intensified upwelling fronts is strongly linked to the synoptic wind field. Thus, especially on the observed short timescales, the observations might represent an extreme situation.

The lesson that can be learned from our study is that high variability of surface CO₂ induced by physical processes on short timescales can occur in the Peruvian upwelling region. The question whether this variability affects the overall CO₂ budget is however not answered. Global data products, as for instance the SOCAT data set, do not have a sufficient coverage of CO₂ measurements in this region to allow for analyses that link the local to broader scales.

Here is also worth saying that in order to define such fine-scale features such as those described in this study as well as their overall relevance, a way forward is the establishment of multi-platform observation networks in which continuous in situ data is complemented by satellite observations and measurements from autonomous platforms such as e.g. gliders. A successful example of this approach is given by Ohman et al. (2013) who show how linking different platforms helps relating changes in the physical and biogeochemical conditions of the California Current Ecosystem over scales ranging from days to years

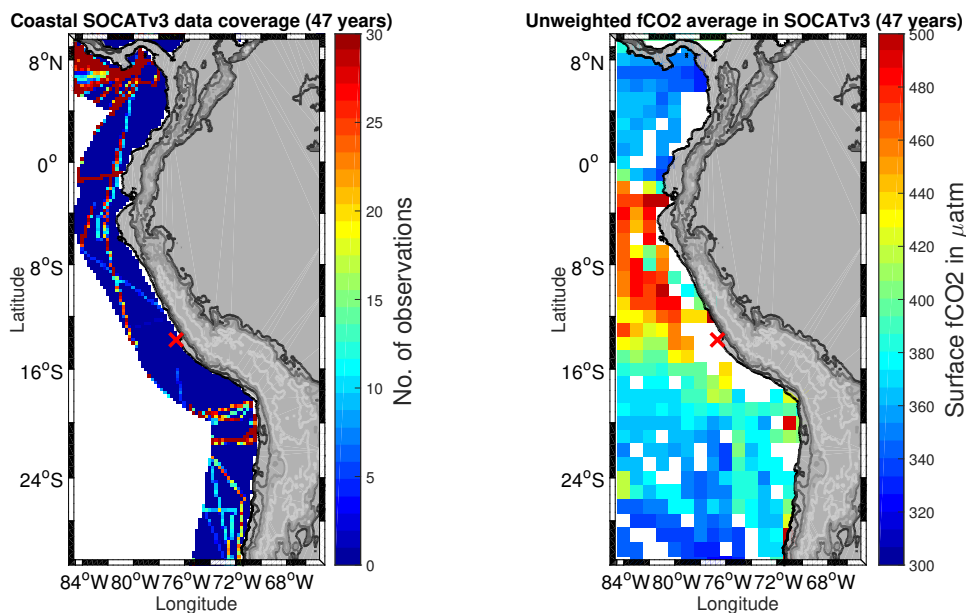


Figure AR2. The SOCAT surface fCO₂ data set shows only scarce data coverage in the Peruvian upwelling region. The number of datapoints collected over 47 years mapped onto a 0.25 degree grid (only for the coastal area) is shown in (a). A 47 year average surface fCO₂ distribution on a 1 degree grid constructed from the data in (a) and from data further offshore is given in (b) in μatm. The red X represents the location of our study.

(and longer). Having such an observational framework is most likely the best way to understand the large impact of short-term variability of an upwelling ecosystem such as the one off Peru. A further example are the moored CO_2 observations from Lefèvre et al. (2008) and Lefèvre and Merlivat (2012) which beyond helping to constrain regional budgets and variability of CO_2 for the Eastern Tropical Atlantic could also be used to reliably estimate the net carbon community production in this area.

- 5 We aim to bring attention to the occurrence of submesoscale variability of surface CO_2 , and how it has the potential to influence our current view of its distribution and emissions from coastal upwelling ecosystems. Upon publication we will ensure the upload of the CO_2 dataset to SOCAT.

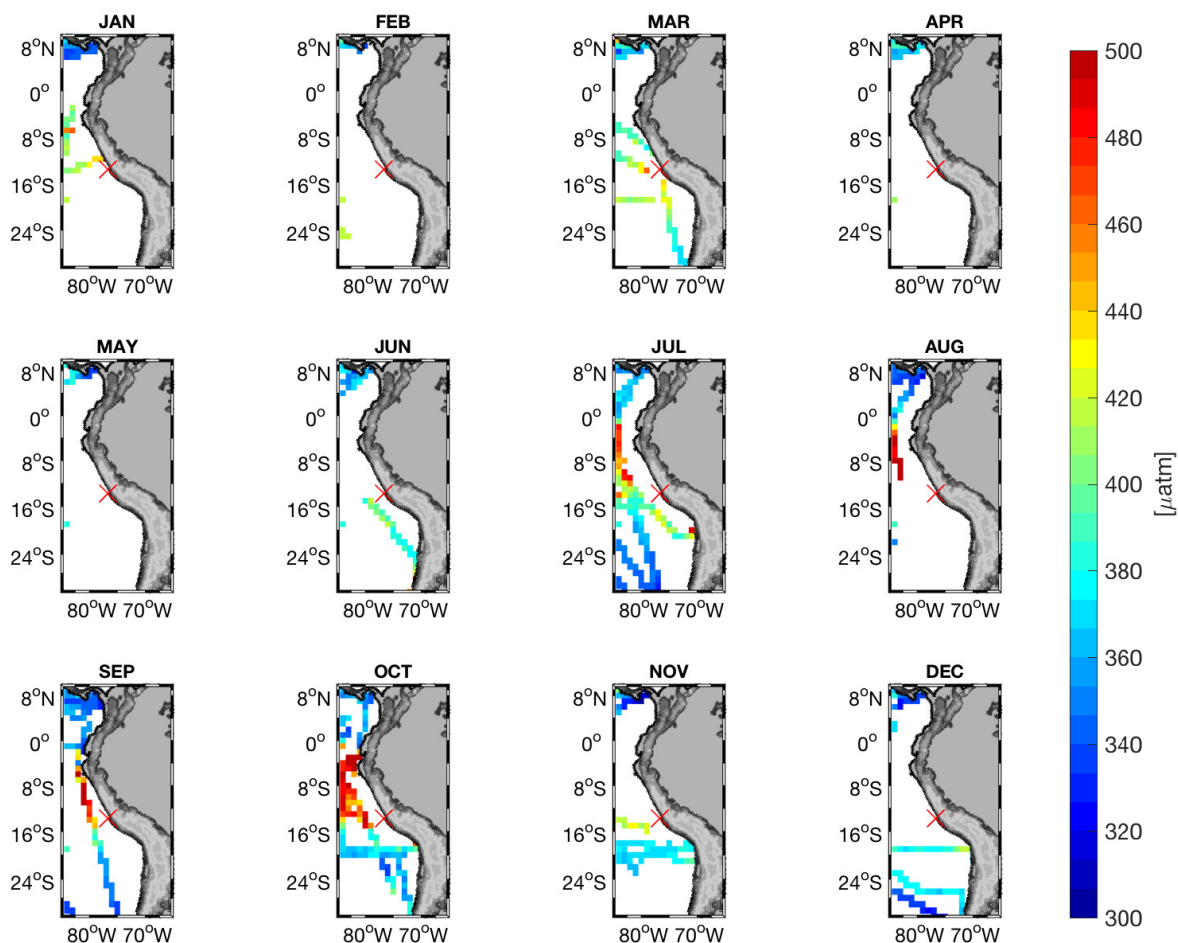


Figure AR3. Monthly composites from 47 years of the SOCATv3 $f\text{CO}_2$ gridded values (1°) in μatm .

MC:

1. In Section 6 the following sentence is included (p. 15 l. 15-20): “The conditions observed in this study are not necessarily representative for February conditions. Many processes on different timescales can alter the upwelling frontal structure and intensity off Peru, for instance the state of the El Niño Southern Oscillation (Espinoza-Morriberón et al., 2017) or coastally trapped waves propagating along the Peruvian coast (Pietri et al., 2014). The aim of this study is rather

5

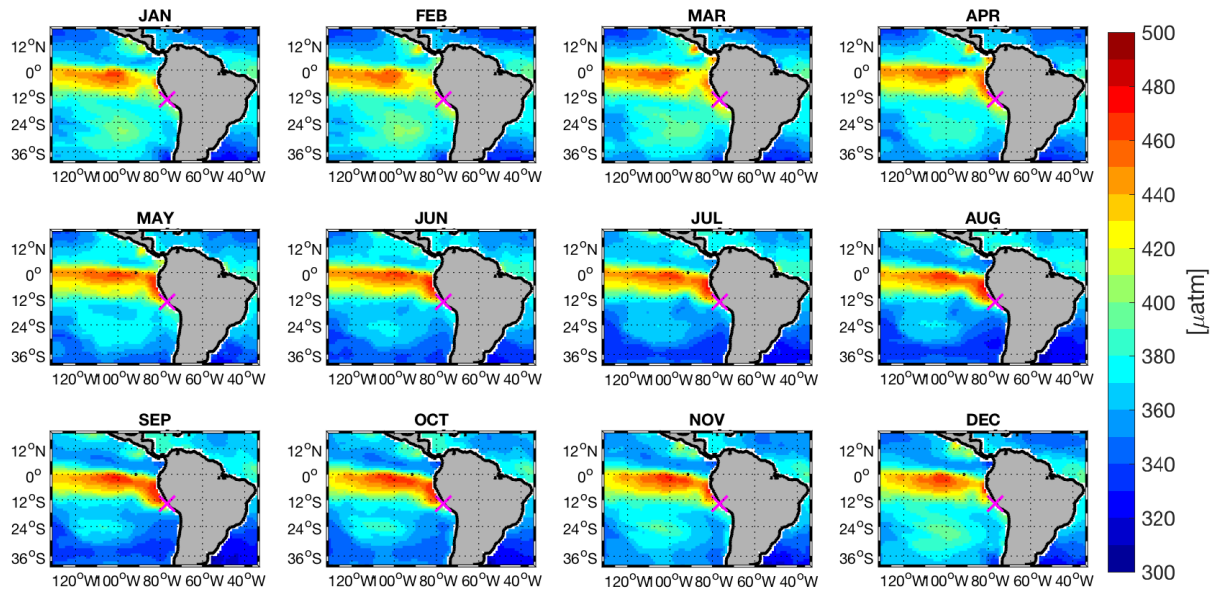


Figure AR4. Monthly $p\text{CO}_2$ climatology of Landschützer et al. (2017) on a 1° grid in μatm . The magenta cross shows the location of our study area.

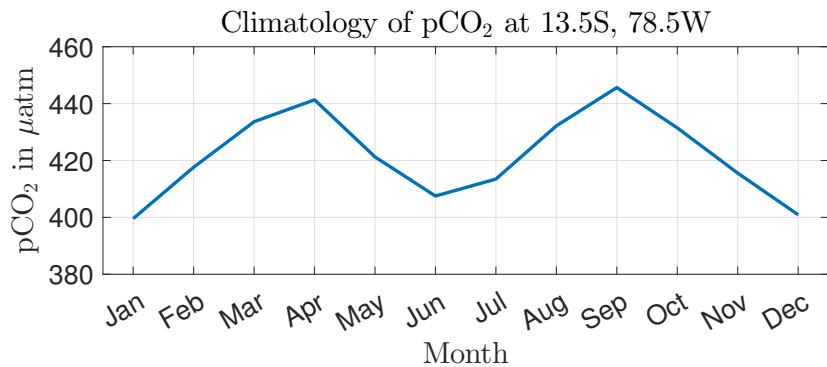


Figure AR5. Monthly $p\text{CO}_2$ climatology of Landschützer et al. (2017) at 13.5°S and 78.5°W , i.e. closest grid point to study location.

to analyze a suite of processes involved in the evolution of the upwelling front and surface $f\text{CO}_2$ on short space and timescales ($\mathcal{O}(1 \text{ km})$, $\mathcal{O}(0.5 \text{ day})$). ”

2. *In Section 7 the following is now included (p. 17 l. 26-31):* “At present, a low CO_2 data coverage within the Peruvian upwelling region (e.g. in SOCAT, Bakker et al. (2016)) complicates the establishment of a reliable climatology, as done by Takahashi et al. (2014) or more recently Landschützer et al. (2017). From our study the importance of the wind and temperature variability on timescales of $\mathcal{O}(\text{hours})$ in setting the strength of sea-air CO_2 fluxes becomes obvious. When coupled with CO_2 measurements the use of sea surface temperature and wind products, which capture the high temporal and spatial variability, could lead to improved future estimates of a CO_2 flux climatology off Peru.”

3. *The end of Section 7 now reads as (p. 17 l. 31 - p. 18 l. 3):* “In order to understand the large scale impact of short-term variability of an upwelling ecosystem, a way forward would be the establishment of multi-platform observation networks in which continuous in situ data is complemented by satellite observations and measurements from autonomous platforms such as e.g. gliders, as for example conducted by Ohman et al. (2013) in the California Current System. A further example are the moored CO_2 observations from Lefèvre et al. (2008) and Lefèvre and Merlivat (2012) which help to constrain regional budgets and variability of CO_2 for the Eastern Tropical Atlantic and could also be used to reliably estimate the net carbon community production in this area.”

2) *Methodology: Further clarification is needed to better understand the experimental design. The beginning of section 2 Data and methods requires a description of the location and timing of field work. This could be addressed by simply moving existing text from the introduction (page 2 lines 21-22) and the results (page 7 lines 2-12). Transects A-C and how they relate to zonal transects 3-7 and cross-frontal transects 1-17) also needs better explanation. Is it possible to show and label all transects in Figures 2 and/or 5 so the reader can better understand how these two figures relate? Transects B and C are mentioned in Fig 2 caption but are not labeled within the figure.*

AR: The Data and Methods part (Section 2) now contains a description of the timing, location and timeline of the experiment. To clarify the experiments procedure, the text was restructured and Figure 2 carries more information regarding the ships route during the cross-frontal transects.

MC:

1. *Changes are made to Figure 2 (labeling the individual transect), clarifying the experiment’s procedure. The caption now reads as:* “Sampling map of underway temperature (a) and $f\text{CO}_2$ (b) along the cruise track. The solid light grey line shows the CTD section (transect A) conducted prior to the seven zonal transects, with black squares indicating CTD stations. The 17 cross-frontal transects are marked by the dark grey lines (a) and dots (b). The black numbers in (a) correspond to the cross-frontal transects. Transects 12 and 14 correspond to the high-resolution subsurface temperature transects B and C. Magenta arrows show the direction of the ship’s track and magenta numbers label the zonal transects. The area presented in both panels is depicted as a red square in Fig. 1.”

2. *At the beginning of Section 2.1 the following is included (combining previous text parts from Section 1 and 3) (p. 2 l. 32 - p.3 l. 12):* “Near 14° S and 76°30’ W the Peruvian upwelling region is characterized by a strong (quasi-) permanent upwelling cell (Fig. 1). The corresponding “upwelling front” was intensively sampled from February 16 to 18 during the RV *Meteor* cruise M93 in February/March 2013. The field work was carried out within the framework of the Collaborative Research Centre SFB754 “Climate-Biogeochemistry Interactions in the Tropical Ocean” (www.sfb754.de). The experiment’s procedure was as follows: Prior to the main experiment, a CTD section (transect “A”, black squares in Fig. 2) was conducted on February 16 from 10:00 to 15:00 (time always in UTC unless stated differently) to document the horizontal circulation and the initial vertical distribution of temperature, salinity, dissolved oxygen (O₂) and chlorophyll-*a* (Chl-*a*) across the front. Starting on February 17 at 04:00, the upwelling front was mapped by seven ~10 km long zonal transects. These were conducted from north to south in 1.8 km spacing (Fig. 2). Each zonal transect took about 45 minutes. From the highest and lowest surface temperature recorded, a cross-frontal axis was estimated. Subsequently, 17 cross-frontal transects were conducted along this axis to study the variability of the front on timescales of several hours. Among these, two high-resolution temperature sections “B” and “C” were conducted as cross-frontal transects 12 and 14. The high-resolution transects took 4.5 hours each to complete, while a regular cross-frontal transect was completed in 40 minutes. The cross-frontal transects were conducted within a 1.8 km wide corridor on three parallel tracks (Fig. 2).”
3. *The end of Section 1 now reads as (p. 2 l. 22-29):* “This paper is structured as follows: In section 2 we present the experiment, the physical and biogeochemical datasets used for this study, as well as the methods employed for their analysis. Section 3 contains a description of the initial state of the front. Observations from the following frontal evolution are presented in section 4. Subsequently, the changes across the temperature front are analyzed in the context of various possible underlying dynamics, such as surface heating (Section 4.1), Ekman buoyancy fluxes (Section 4.2), submesoscale mixed layer instabilities (Section 4.3) or pressure driven gravity currents (Section 4.4). In section 5 these mechanisms are compared with respect to their associated buoyancy fluxes. Section 6 contains a discussion of the different mechanisms which possibly drive the observed variability. The conclusions drawn from this study follow in section 7.”
4. *In Section 6 the following is included (p. 16 l. 1-3):* “Further, the fact that the cross-frontal transects show coherent signals, even though not all cross-frontal transects were performed on the exact same track, but about 1 km apart, points towards a weak along-frontal flow variability.”

Minor comments/edits:

- 30 **Page 1 line 5: Here and at key points throughout it would be useful to mention the direction (N-E-S-W) of downfrontal, along-frontal, etc winds.**

AR: It is dynamically more important that the wind is blowing constantly downfrontal than its absolute direction, but at key points throughout the manuscript the direction (e.g. “equatorward”) is added to clarify the meaning of along-frontal or

downfrontal.

Page 2 lines 3-5: Some rephrasing necessary here. Processes **are** difficult to observe? By "their importance" do you mean submesoscale processes or models? Do you mean altering, not altering?

5

AR: This part is rephrased for more clarity. The typo regarding "altering" is also corrected.

MC: In Section 1 the rephrased sentence reads as (p. 2 l. 2-5): "However, submesoscale frontal processes are difficult to observe due to their small spatial and temporal scales. At the same time the importance of these dynamics for physical-
10 biogeochemical coupling has been put forward by model studies, e.g. by altering the vertical transports of nutrients and organic carbon ..."

Page 5 section 2.2: What is the estimated uncertainty in $f\text{CO}_2$ measurements and resulting CO_2 flux? How does using mean salinity during the field study impact the $f\text{CO}_2$ uncertainty?

15

AR: The uncertainty of the CO_2 measurements was about $\pm 2 \mu\text{atm}$. The $f\text{CO}_2$ is mostly dependent on temperature with an isochemical dependence of $15 \mu\text{atm per } ^\circ\text{C}$ (this means that a $1 ^\circ\text{C}$ error in temperature measurements can lead to a bias as high as $15 \mu\text{atm}$ in $f\text{CO}_2$, see e.g. Körtzinger et al. (2000); Pierrot et al. (2009)). The effect of salinity is rather marginal in comparison with the one of temperature both for the $f\text{CO}_2$ computation as well as for the flux estimates since both viscosity and
20 the molecular diffusion coefficients used for the calculations vary only slightly with salinity changes (see eg. Pilson (2012)). To illustrate this point we calculated the $f\text{CO}_2$ with $s_{34} = 34.0406$ and $s_{36} = 36.0406$ and compared the mean differences to the values we used for this study. As can be seen in Figure AR6, changing salinities did not considerably affect $f\text{CO}_2$ values (mean difference for $s_{34} = 0.0055$ and for $s_{36} = -0.0055$).

25 MC: In Section 2.2 the following sentence is added (p. 6 l. 11-14): "A change in the mean salinity by 1 leads to a mean offset of $0.0055 \mu\text{atm}$ and has thus a small influence compared to temperature with an isochemical dependence of $15 \mu\text{atm per } ^\circ\text{C}$ (e.g. Körtzinger et al. (2000); Pierrot et al. (2009)). The uncertainty of the CO_2 measurements was hence about $\pm 2 \mu\text{atm}$."

Figure 4: Be consistent in presenting units (e.g., either kg^{-1} or $/\text{kg}$). State in the caption what the contour lines represent.

30

AR: The units of Fig. 5 (previously Fig. 4) are changed to consistently use the exponential form. It is stated in the caption, that the white contour lines represent isopycnals calculated from the CTD data. The thin white lines present before due to rendering issues are removed in the revised version.

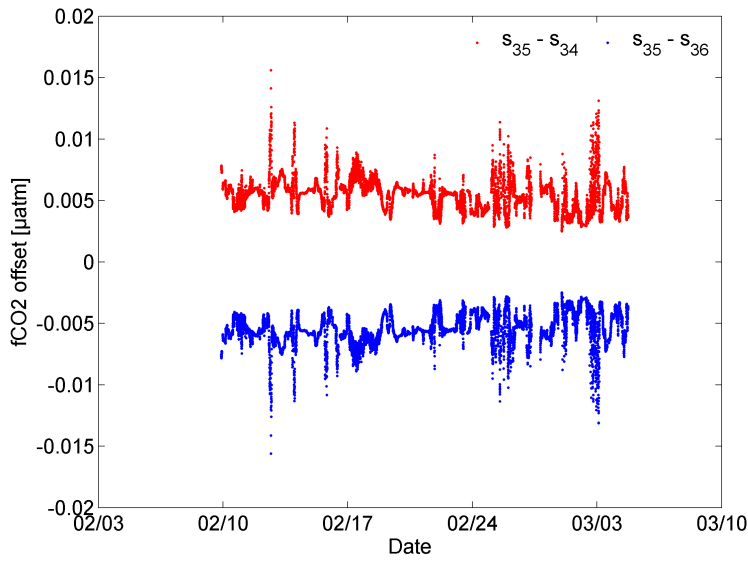


Figure AR6. Influence of salinity on $f\text{CO}_2$ during the entire M93 expedition.

Page 7 line 4: Does Feb 16 10:00-15:00 represent the main experiment or the CTD transect?

AR: The time information given in parentheses is shifted further back in the sentence to clarify the association of this time period with the CTD transect.

5

MC: The sentence is now included in Section 2.1 and reads as follows (p. 3 l. 3-5): “Prior to the main experiment, a CTD section (transect “A”, black squares in Fig. 2) was conducted on February 16 from 10:00 to 15:00 (time always in UTC unless stated differently) to document the horizontal circulation and the initial vertical distribution of temperature, salinity, dissolved oxygen (O_2) and chlorophyll-a (Chl-*a*) across the front.”

10

Figure 5 caption: In panel (e) clarify that velocities are represented by lines and vorticity by circles.

AR: Symbols are clarified.

15

MC: The beginning of the caption of Fig. 6 (previously Fig. 5) now reads as: “Hovmoeller diagrams of the cross-frontal surface temperature gradient (a), underway surface temperatures (b), surface $f\text{CO}_2$ (c), ocean-atmosphere CO_2 fluxes (d), mean current velocities in the upper 40 m (black lines) and vorticity (colored circles) (e) and diabatic surface heating (f) for the last

five zonal transects and the subsequent 17 cross-frontal transects.”

Page 10 line 6: Spell out local time or define acronym.

5 AR: LT changed to “local time”.

MC:

1. *The sentence in Section 4.1 now reads as (p. 9 l. 9-10): “The wind begins to drop at 11:00 on February 17 (06:00 local time) and the temperature gradient fully vanishes 14 hours later at 01:00 on February 18 (Fig. 6a).”*
2. *In the description of the diurnal cycle of surface heat fluxes (Section 4.1) the local time is added at a few instances for better readability.*

10

Page 10 line 25: Is a comma meant after anomalies?

AR: comma inserted.

15

MC: *The sentence in Section 4.1 now reads as (p. 9 l. 29-30): “Even though this roughly corresponds to the amplitude of the temperature anomalies, the lateral homogeneity of the net surface heat flux prohibits to attribute the development of the anomalies to surface heating.”*

20 Page 11 line 2: Present consistent # of significant digits.

AR: The salinity is changed to be consistently given with one digit.

MC: *The sentence in Section 4.1 now reads as (p. 10 l. 5-6): “The initial CTD section shows a surface salinity varying*
25 *between 35.1 and 35.2 (Fig. 5c)”*

Page 12 line 8: The weakening of the front is not caused by Ekman transport as demonstrated by what?

AR: This sentence is restructured to clarify its function of summarizing the above results.

30

MC: *The sentence in Section 4.2 now reads as (p. 11 l. 11): “The results above show, that the weakening of the temperature front is not directly caused by onshore Ekman transport.”*

Figure 9 caption: Is the uncertainty range represented by the shaded areas around the lines? Add "(green)" after introducing Rb ratio. Why are the Rb ratio errors omitted? Also, consider defining the Rb ratio before presenting Fig 9.

AR: It is now clarified in the caption that the uncertainty range is represented by the shaded areas. The error is also included for the Rb ratio. Introducing the Rb ratio before referencing the Fig. 9 would be helpful, but it is only important in the comparison of buoyancy fluxes and could lead to confusion if introduced while discussing the individual physical processes.

MC: The caption of Figure 9 now reads as: "Vertical buoyancy fluxes associated with surface heating (blue), Ekman transport (red) and mixed layer instabilities (magenta). The shaded areas around the Ekman buoyancy flux (EBF) and the buoyancy flux associated with mixed layer instabilities (MLI) are accounting for uncertainties in the surface salinity gradient (see text for more details). The shaded uncertainty range for vertical buoyancy fluxes due to surface heating is given as one standard deviation obtained from sectional averaging. The sum of the three processes is given by the black line. The uncertainty is given as the maximum error resulting from the three processes. The R_b ratio (green) and its uncertainty are treated similarly. For cross-frontal transect 13 and 14 no R_b value or error can be stated due to the vanishing denominator in the definition of R_b . $\log_{10}(R_b) > 0$ points towards a net restratification, while $\log_{10}(R_b) < 0$ indicates a destabilization of the water column. For calculation details of all quantities see text. Time is given in UTC. The small black numbers on top indicate the respective zonal or cross-frontal transect number."

Figure 10 caption: Explain what 200 and 8.7 km represents in panel (a).

AR: It is now highlighted in the caption of Fig. 10, that the labels show the length scales associated with the local maxima for better readability. The length scales are now also explicitly stated in the figure caption in brackets.

MC: The caption of Figure 10 now reads as: "(a) Initial growth rate of barolinic instabilities obtained from linear stability analysis, applied to the frontal state during the CTD section (transect A). The local maxima of the growth rate are labeled by their corresponding length scale in km. The smoothed stratification and geostrophic along-frontal velocity profiles used as the background state, are shown in panels (b) and (c). A deep mode at large horizontal scales (200 km) and a shallow mode, associated with mixed layer instabilities and short horizontal length scales (8.7 km) are present. The corresponding anomalies for the cross-front (u) and along-front (v) velocities are shown in panels (d) and (e) for the deep and shallow modes, respectively."

Page 17 line 12: Development misspelled.

AR: Typo corrected.

MC: The sentence in Section 5 now reads as (p. 13 l. 31 - p. 14 l. 1): “During the time of the development of the coherent surface temperature anomalies (cross-frontal transects 7-11), the combination of the three processes favor a restratification of the mixed layer (Fig. 9).”

5 Page 18 lines 16-17: Wouldn't the difference between delta pCO₂ and fCO₂ be insignificant compared to measurement uncertainty?

AR: Normally the difference between pCO₂ and fCO₂ is about 3%. However regardless of the uncertainty of Friederich et al. (2008) estimates, we opted for using the same magnitude in order to compare both studies.

10

MC: The sentence in Section 6 now reads as (p. 15 l. 4-6): “Our observations show CO₂ outgassing rates between 3.5 and 30 mol m⁻² yr⁻¹ which are in line with the outgassing signals observed by Friederich et al. (2008), even after accounting for the difference in converting our values from partial pressures to fugacities (difference usually about 3%).”

15 Page 18 line 22: How much does the parameterization of Friederich et al. overestimate CO₂ flux compared to the parameterization used here?

AR: The Wanninkhof (1992) (W92) parameterization which was used on the study by Friederich et al. (2008) is known to overestimate the gas transfer velocities (and therefore the air-sea fluxes; see Garbe et al. (2014)). Since the authors of that study used a slightly different methodology to ours and employed monthly wind products instead of instantaneous, it is difficult to provide an accurate estimate of how much their values overestimate CO₂ with respect to ours, which are based on the Nightingale et al. (2000) parameterization (N00). However, computing our fluxes with both parameterizations resulted in a mean flux density difference (W92-N00) of 0.802 mmol m⁻² d⁻¹, which in turn equates to about 17% difference. Hence, had we used the same parameterization as Friederich et al. (2008), our flux density calculations would have resulted in even higher values compared to those from their study.

MC: The part in Section 6 now reads as (p. 15 l. 9-13): “The results from Friederich et al. (2008) were re-scaled to a much larger area (5° S - 15° S), have been subject of spatial extrapolation and smoothing, and were calculated with the sea-air gas exchange parameterization by Wanninkhof (1992) which tends to overestimate the gas transfer velocities (see Wanninkhof (2014)). Simply using the Wanninkhof (1992) parameterization instead of the Nightingale et al. (2000) parameterization yields 17% higher fluxes, already indicating that it is difficult to draw a direct comparison between both data sets.”

Page 21 line 2: Rephrase "responsible for fast the observed changes"

AR: Swapped the words “fast” and “the” to correct the sentence.

MC: The sentence in Section 7 now reads as (p. 17 l. 24-25): “In addition, our analysis shows that multiple processes act simultaneously and are likely to interact, thus complicating the identification of a single, dominant mechanism responsible for the fast observed changes in surface $f\text{CO}_2$.”

References:

Bakker, D.C.E., Pfeil, B., Smith, K., Hankin, S., Olsen, A., Alin, S.R., Cosca, C., Harasawa, S., Kozyr, A., Nojiri, Y., O’Brien, K.M., Schuster, U., Telszewski, M., Tilbrook, B., Wada, C., Akl, J., Barbero, L., Bates, N.R., Boutin, J., Bozec, Y., Cai, W.-J., Castle, R.D., Chavez, F.P., Chen, L., Chierici, M., Currie, K., de Baar, H.J.W., Evans, W., Feely, R.A., Fransson, A., Gao, Z., Hales, B., Hardman-Mountford, N.J., Hoppema, M., Huang, W.-J., Hunt, C.W., Huss, B., Ichikawa, T., Johannessen, T., Jones, E.M., Jones, S.D., Jutterstrom, S., Kitidis, V., Koertzing, A., Landschuetzer, P., Lauvset, S.K., Lefevre, N., Manke, A.B., Mathis, J.T., Merlivat, L., Metzl, N., Murata, A., Newberger, T., Omar, A.M., Ono, T., Park, G.-H., Paterson, K., Pierrot, D., Rios, A.F., Sabine, C.L., Saito, S., Salisbury, J., Sarma, V.V.S.S., Schlitzer, R., Sieger, R., Skjelvan, I., Steinhoff, T., Sullivan, K.F., Sun, H., Sutton, A.J., Suzuki, T., Sweeney, C., Takahashi, T., Tjiputra, J., Tsurushima, N., van Heuven, S.M.A.C., Vandemark, D., Vlahos, P., Wallace, D.W.R., Wanninkhof, R., Watson, A.J. (2014) An update to the Surface Ocean CO₂ Atlas (SOCAT version 2). Earth System Science Data 6, 69-90.

Friederich, G.E., Ledesma, J., Ulloa, O., Chavez, F.P. (2008) Air–sea carbon dioxide fluxes in the coastal southeastern tropical Pacific. Progress In Oceanography 79, 156- 166.

Landschützer, P., Gruber, N., Bakker, D.C.E., Schuster, U. (2014) Recent variability of the global ocean carbon sink. Global Biogeochemical Cycles, 2014GB004853.

Anonymous Referee #2:

Received and published: 29 July 2017

This paper offers valuable insight into the impact of eastern boundary upwelling systems on CO₂ fluxes. The data is unique and the analysis potentially very useful to the community. I recommend publication after the authors address the comments
5 below.

There is ambiguity and uncertainty with the wind speed and flux estimates that I believe the authors should address:
The authors state that the wind speed was recorded at 35.3 m (Figure 6) and at 35.5 m (section 2.1). Which is it?

AR: 35.5 m was a typo. Changed to 35.3 m.

MC: The sentence in Section 2.1 now reads as (p. 3 l. 16 - p. 4 l. 1): “Wind velocity and direction were measured at a height
10 of 35.3 m above the sea surface at a temporal resolution of 60 seconds.”

The authors state that they followed Smith (1988) to calculate U₁₀ (section 4.5) and also state that Garratt (1997) is used to
15 standardize the wind speed to 10 m height (section 2.2). If the authors are using two different methods, it should be justified.
The method used will certainly impact the estimated 10 m wind speed. The authors use U₁₀ to determine the wind stress, the
Eckman velocity, and the air-sea CO₂ fluxes, therefore accurate estimation of the 10 m wind speed is essential to this paper.
However, many studies have shown that the boundary layer profile is impacted by the swell/wind sea conditions and their rela-
20 tionship to the wind direction (e.g., Nilsson et al. 2002). Therefore, there is inherent uncertainty in U₁₀ when not accounting
these conditions. With a difference between measured U and U₁₀ of over 20 m, there is certain to be error in the U₁₀ estimate
which will feed into the parameterizations previously mentioned. This should be addressed.

AR: Thank you for pointing out the inconsistency in the manuscript, which was due to historical reasons in the manuscript
preparation. To overcome the inconsistency, the wind speed was scaled to 10 m height using both schemes (Garratt, 1977;
25 Smith, 1988). Both amplitudes are shown in Figure AR7. As the difference is only very minor, the Smith (1988) scheme is
used in all calculations, including the CO₂ flux, which on average only changes by 0.8%. Thus, in the manuscript, Fig. 6d
(previously Fig. 5d) is changed accordingly.

Multiple studies have put forward the need for a parameterization of the drag coefficient incorporating a dependency on
the sea state (e.g. Donelan et al. (1997); Drennan et al. (1999)). The studies of Donelan et al. (1997) and Pan et al. (2005)
30 show that especially in cases of counter swell (i.e. swell directed opposite to the wind direction) and low wind speeds, the drag
coefficient is strongly increased. Meanwhile, in the presence of wind-following swell Nilsson et al. (2012) link stronger near
surface wind speeds to a lowered surface drag coefficient. Our study was carried out in a region of stable southerly winds with
wind speeds most of the time above 5 m s⁻¹. Synoptic measurements taken by the ship’s meteorologist every three hours show
swell conditions with an average wave height of 1.5 ± 0.5 m and a southerly origin propagating northward (180-200°). Hence,

the swell was generally wind-following and of similar height as the wind sea with a significant wave height of 1 ± 0.5 m. As a result, the sea state during the experiment period cannot be classified as wind sea or swell dominated. In the study of Dobson et al. (1994) and Pan et al. (2005) the estimates of the drag coefficient for the mixed sea conditions at wind speeds at least larger than 5 m s^{-1} agree quite well with the relationship given by Smith (1988), despite some existing data scatter. Thus, as
5 wind speeds were most of the time higher than 5 m s^{-1} with mixed sea conditions we followed Smith (1988) in estimating the drag coefficient and scaling the wind measurements to 10 m height.

MC:

1. *The sentence in Section 2.2 now reads as (p. 6 l. 14-16): “The air-sea flux of CO_2 was computed by using $F = kK_0(f\text{CO}_{2\text{sw}} - f\text{CO}_{2\text{air}})$, where k is the air-sea gas exchange coefficient, calculated using the parameterization of Nightingale et al. (2000) with wind speeds standardized to 10 m height (Smith, 1988).”*
10
2. *Figure 6d (previously Figure 5d) now shows the CO_2 flux data using Smith (1988).*
3. *In Section 2.1 the description of wind speed measurements now reads as (p. 3 l. 16 - p. 4 l. 2): “Wind velocity and direction were measured at a height of 35.3 m above the sea surface at a temporal resolution of 60 seconds. The surface wind stress was estimated from these measurements following Smith (1988).”*
15
4. *A plotting error concerning the wind direction in Figure 4 (previously Figure 6) is corrected. The caption carries a more thorough explanation: “Time series of total wind speed (grey) and wind direction (black) from underway measurements at 35.3 m height. Blue rectangles show mean total wind speed for each zonal and cross-frontal transect. The dashed red line shows the (initial) frontal orientation deduced from the frontal mapping. The angle of 163.44° implicates the front running from south-south-east to north-north-west. The vertical dashed grey line indicates the transition from zonal to cross-frontal transects. Time is given in UTC.”*
20

There is significant uncertainty in the parameterization of the drag coefficient, especially at low wind speeds, i.e. $< 5 \text{ m/s}$ (e.g., Figure 7 of Pan et al., 2005). During this experiment, wind speeds dropped below 5 m/s on several occasions. Therefore inherent uncertainty in estimates of wind stress (Ekman transport) must exist. This should be addressed.

25

AR: The uncertainty in the drag coefficient especially at low wind speeds discussed by Pan et al. (2005) indeed produces an uncertainty in the estimate of the surface wind stress and hence the Ekman transport. However, the estimates of the Ekman transport already carry a quite large error, for example due to the uncertain mixed layer depth. Further, the main signal of the wind drop by almost 70% from about 12 m s^{-1} to 4 m s^{-1} should translate into a significant change in wind stress, despite the
30 inherent uncertainty of the drag coefficient. Thus, we followed the procedure according to Smith (1988).

MC: No manuscript changes.

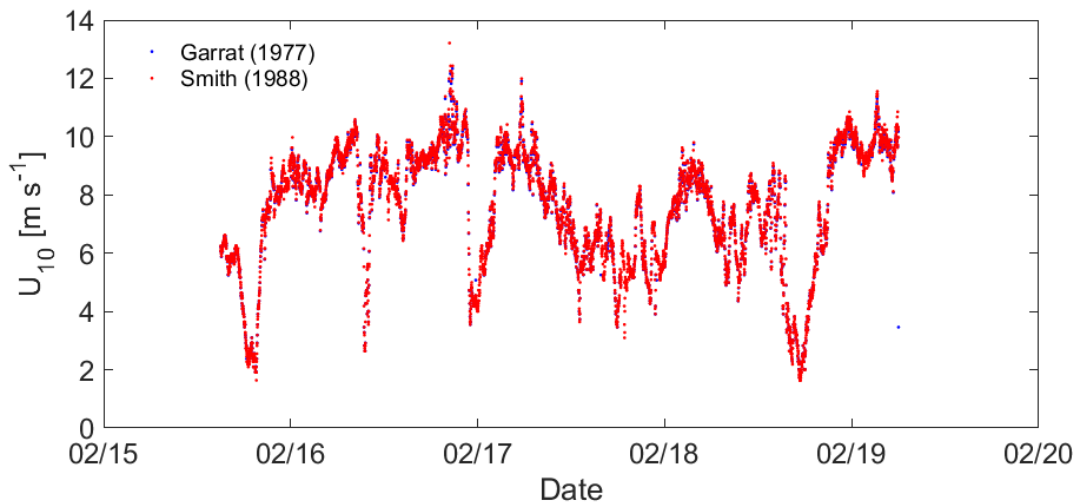


Figure AR7. Wind speed normalized to 10 m height, using the Garratt (1977) and Smith (1988) scheme. The difference is only minor.

Finally, I wonder if the authors explored flow distortion on the R/V which may also have impacted measured wind speed and therefore U_{10} . This would feed into parameterized variables already mentioned. While the wind direction was generally constant, the R/V travel direction changed throughout the experiment, this would have impacted flow around the R/V, potentially impacting the measured wind speed. This should be addressed.

5

AR: Very little is known about flow distortion on RV *Meteor*. A study on flow distortion on the somewhat bigger RV *Polarstern* has been carried out by Berry et al. (2001). They only analyzed perfect head wind conditions with a lattice mast positioned well in front of the bow. Using their findings, Bumke et al. (2014) conclude, that the effect of flow distortion around RV *Polarstern* is mainly a deceleration/acceleration along the ship's axis and that a vertical displacement of the wind is negligible for measurements taken over 30 m height. This picture will of course change if the wind does not reach the ship from the bow but more from star- or portboard, but little is known about these situations. The wind sensor is located on the highest platform of RV *Meteor*. With no other object on the same height, the wind sensor is very exposed, so that no great disturbance should be expected. A tail wind situation could lead to larger issues with the wind crossing the ship's aft and chimney, before reaching the sensor. However, during the experiment, the wind blew mostly from south-south-east (Fig. 4 (previously Fig. 6) in manuscript). The cross-frontal axis and correspondingly the ship's heading is roughly in a right angle to the wind direction (see Fig. AR8a). Thus, when crossing the front, the wind reached the sensor directly from port or starboard (Fig. AR8b), without crossing other parts of the ship. With a maximal width of 16.5 m, the wind had to cover a distance of maximal 10 m above the ship, before reaching the sensor. Over this distance, the influence of the ship's hull or lower lying instruments is presumably not very strong. No significant systematic error in the wind speed data can be identified between the transects directed towards and away from the shore. To reduce the impact of flow distortion Bumke et al. (2014) limited their data analysis to a relative

10

15

20

wind coming from within a corridor of $\pm 60^\circ$ around perfect bow-on wind. Fig. AR8b shows that $\sim 35\%$ of the wind data were measured in a wind corridor of $\pm 60^\circ$, but that $\sim 80\%$ of the wind data was measured in a somewhat wider wind corridor of $\pm 90^\circ$.

5 While the ship's flow distortion produces some error in the estimation of the wind speed through deceleration/acceleration and vertical displacement, it is unlikely that it can obscure the dominant signal of the wind speed decrease. The high and exposed location of the measurement platform are expected to keep the error at a minimum level.

MC: No manuscript changes.

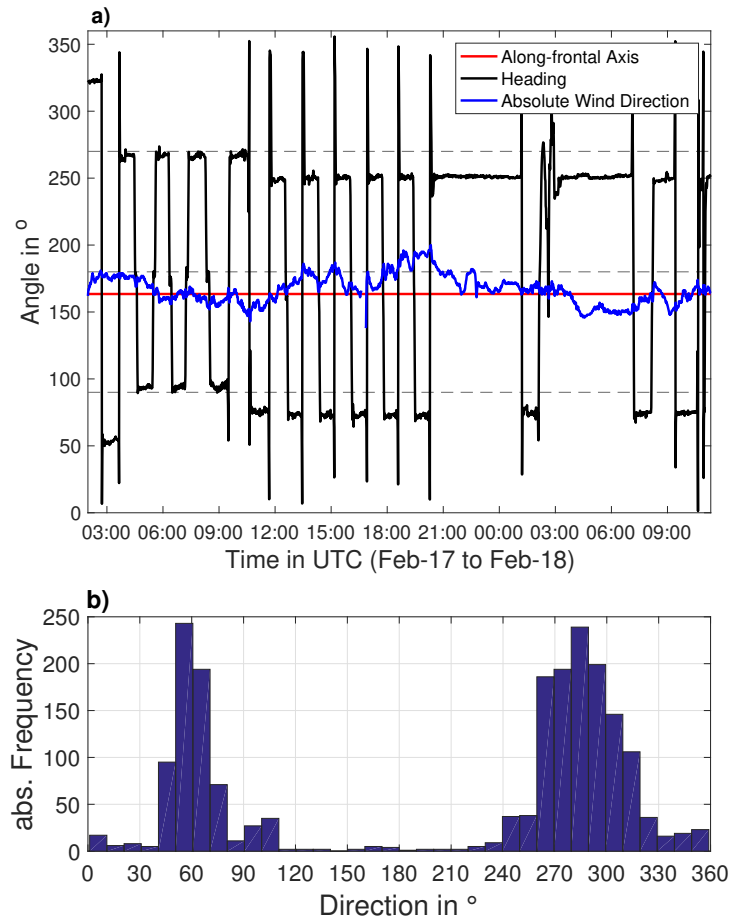


Figure AR8. a) Timeseries of the ship’s heading (black) during the zonal and cross-frontal transects. 270° correspond to westward heading, 180° to southward and 90° to eastward heading. The direction of the predominantly southerly (180°) winds is given in blue, which is approximately parallel to the along-frontal axis (red). Throughout the transects there exists a difference between the wind direction and heading of around 90°, indicating their orthogonality. b) Histogram of the relative wind direction. A direction of 0°/360° corresponds to head wind, while 180° corresponds to tail wind and 90° corresponds to wind coming from starboard.

References

- Albert, A., Echevin, V., Lévy, M., and Aumont, O.: Impact of nearshore wind stress curl on coastal circulation and primary productivity in the Peru upwelling system, *Journal of Geophysical Research: Oceans*, 115, C12033, doi:10.1029/2010JC006569, 2010.
- 5 Bakker, D. C. E., Pfeil, B., Landa, C. S., Metzl, N., O’Brien, K. M., Olsen, A., Smith, K., Cosca, C., Harasawa, S., Jones, S. D., Nakaoka, S.-I., Nojiri, Y., Schuster, U., Steinhoff, T., Sweeney, C., Takahashi, T., Tilbrook, B., Wada, C., Wanninkhof, R., Alin, S. R., Balestrini, C. F., Barbero, L., Bates, N. R., Bianchi, A. A., Bonou, F., Boutin, J., Bozec, Y., Burger, E. F., Cai, W.-J., Castle, R. D., Chen, L., Chierici, M., Currie, K., Evans, W., Featherstone, C., Feely, R. A., Fransson, A., Goyet, C., Greenwood, N., Gregor, L., Hankin, S.,

- Hardman-Mountford, N. J., Harlay, J., Hauck, J., Hoppema, M., Humphreys, M. P., Hunt, C. W., Huss, B., Ibáñez, J. S. P., Johannessen, T., Keeling, R., Kitidis, V., Körtzinger, A., Kozyr, A., Krasakopoulou, E., Kuwata, A., Landschützer, P., Lauvset, S. K., Lefèvre, N., Lo Monaco, C., Manke, A., Mathis, J. T., Merlivat, L., Millero, F. J., Monteiro, P. M. S., Munro, D. R., Murata, A., Newberger, T., Omar, A. M., Ono, T., Paterson, K., Pearce, D., Pierrot, D., Robbins, L. L., Saito, S., Salisbury, J., Schlitzer, R., Schneider, B., Schweitzer, R., 5 Sieger, R., Skjelvan, I., Sullivan, K. F., Sutherland, S. C., Sutton, A. J., Tadokoro, K., Telszewski, M., Tuma, M., van Heuven, S. M. A. C., Vandemark, D., Ward, B., Watson, A. J., and Xu, S.: A multi-decade record of high-quality $f\text{CO}_2$ data in version 3 of the Surface Ocean CO_2 Atlas (SOCAT), *Earth System Science Data*, 8, 383–413, 2016.
- Berry, D. I., Moat, B. I., and Yelland, M. J.: Airflow distortion at instrument sites on the FS Polarstern, Southampton Oceanography Centre Internal Document No. 69, pp. 1–36, 2001.
- 10 Bumke, K., Schlundt, M., Kalisch, J., Macke, A., and Kleta, H.: Measured and Parameterized Energy Fluxes Estimated for Atlantic Transects of R/V Polarstern, *J. Phys. Oceanogr.*, 44, 482–491, doi:10.1175/jpo-d-13-0152.1, 2014.
- Dobson, F. W., Smith, S. D., and Anderson, R. J.: Measuring the relationship between wind stress and sea state in the open ocean in the presence of swell, *Atmosphere-Ocean*, 32, 237–256, doi:10.1080/07055900.1994.9649497, 1994.
- Donelan, M. A., Drennan, W. M., and Katsaros, K. B.: The Air–Sea Momentum Flux in Conditions of Wind Sea and Swell, *Journal of* 15 *Physical Oceanography*, 27, 2087–2099, doi:10.1175/1520-0485(1997)027<2087:TASMFI>2.0.CO;2, 1997.
- Drennan, W. M., Graber, H. C., and Donelan, M. A.: Evidence for the Effects of Swell and Unsteady Winds on Marine Wind Stress, *Journal of Physical Oceanography*, 29, 1853–1864, doi:10.1175/1520-0485(1999)029<1853:EFTEOS>2.0.CO;2, 1999.
- Echevin, V., Aumont, O., Ledesma, J., and Flores, G.: The seasonal cycle of surface chlorophyll in the Peruvian upwelling system: A modelling study, *Progress in Oceanography*, 79, 167–176, 2008.
- 20 Espinoza-Morriberón, D., Echevin, V., Colas, F., Tam, J., Ledesma, J., Vásquez, L., and Graco, M.: Impacts of El Niño events on the Peruvian upwelling system productivity, *Journal of Geophysical Research: Oceans*, 122, 5423–5444, doi:10.1002/2016JC012439, 2017.
- Feely, R., Takahashi, T., Wanninkhof, R., McPhaden, M., Cosca, C., Sutherland, S., and Carr, M.-E.: Decadal variability of the air-sea CO_2 fluxes in the equatorial Pacific Ocean, *Journal of Geophysical Research: Oceans*, 111, 2006.
- Friederich, G. E., Ledesma, J., Ulloa, O., and Chavez, F. P.: Air-sea carbon dioxide fluxes in the coastal southeastern tropical Pacific, *Progress* 25 *in Oceanography*, 79(2-4), 156–166, doi:10.1016/j.pocean.2008.10.001, 2008.
- Garbe, C. S., Rutgersson, A., Boutin, J., De Leeuw, G., Delille, B., Fairall, C. W., Gruber, N., Hare, J., Ho, D. T., Johnson, M. T., et al.: Transfer across the air-sea interface, in: *Ocean-Atmosphere Interactions of Gases and Particles*, edited by Liss, P. S. and Johnson, M. T., pp. 55–112, Springer, 2014.
- Garratt, J. R.: Review of Drag Coefficients over Oceans and Continents, *Monthly Weather Review*, 105, 915–929, doi:10.1175/1520- 30 0493(1977)105<0915:RODCOO>2.0.CO;2, 1977.
- Körtzinger, A., Mintrop, L., Wallace, D. W., Johnson, K. M., Neill, C., Tilbrook, B., Towler, P., Inoue, H. Y., Ishii, M., Shaffer, G., et al.: The international at-sea intercomparison of $f\text{CO}_2$ systems during the R/V Meteor Cruise 36/1 in the North Atlantic Ocean, *Marine Chemistry*, 72, 171–192, 2000.
- Landschützer, P., Gruber, N., Bakker, D., and Schuster, U.: Recent variability of the global ocean carbon sink, *Global Biogeochemical Cycles*, 35 28, 927–949, 2014.
- Landschützer, P., Gruber, N., and C. E. Bakker, D.: An updated observation-based global monthly gridded sea surface pCO_2 and air-sea CO_2 flux product from 1982 through 2015 and its monthly climatology (NCEI Accession 0160558). Version 2.2. NOAA National Centers for Environmental Information. Dataset. [2017-07-11], 2017.

- Lefèvre, N. and Merlivat, L.: Carbon and oxygen net community production in the eastern tropical Atlantic estimated from a moored buoy, *Global biogeochemical cycles*, 26, 2012.
- Lefèvre, N., Guillot, A., Beaumont, L., and Danguy, T.: Variability of $f\text{CO}_2$ in the Eastern Tropical Atlantic from a moored buoy, *Journal of Geophysical Research: Oceans*, 113, 2008.
- 5 Nightingale, P. D., Malin, G., Law, C. S., Watson, A. J., Liss, P. S., Liddicoat, M. I., Boutin, J., and Upstill-Goddard, R. C.: In situ evaluation of air-sea gas exchange parameterizations using novel conservative and volatile tracers, *Global Biogeochemical Cycles*, 14(1), 373–387, doi:10.1029/1999GB900091, 2000.
- Nilsson, E. O., Rutgersson, A., Smedman, A.-S., and Sullivan, P. P.: Convective boundary-layer structure in the presence of wind-following swell, *Quarterly Journal of the Royal Meteorological Society*, 138, 1476–1489, doi:10.1002/qj.1898, 2012.
- 10 Ohman, M. D., Rudnick, D. L., Chekalyuk, A., Davis, R. E., Feely, R. A., Kahru, M., Jim, H.-J., Landry, M. R., Martz, T. R., Sabine, C. L., and Send, U.: Autonomous ocean measurements in the California Current Ecosystem, *Oceanography*, 26, 18–25, 2013.
- Pan, J., Wang, D. W., and Hwang, P. A.: A study of wave effects on wind stress over the ocean in a fetch-limited case, *Journal of Geophysical Research: Oceans*, 110, 2005.
- Pierrot, D., Neill, C., Sullivan, K., Castle, R., Wanninkhof, R., Lüger, H., Johannessen, T., Olsen, A., Feely, R. A., and Cosca, C. E.:
 15 Recommendations for autonomous underway pCO_2 measuring systems and data-reduction routines, *Deep Sea Research Part II: Topical Studies in Oceanography*, 56, 512–522, 2009.
- Pietri, A., Echevin, V., Testor, P., Chaigneau, A., Mortier, L., Grados, C., and Albert, A.: Impact of a coastal-trapped wave on the near-coastal circulation of the Peru upwelling system from glider data, *Journal of Geophysical Research: Oceans*, 119, 2109–2120, 2014.
- Pilson, M. E.: *An Introduction to the Chemistry of the Sea*, Cambridge Univ. Press, 2 edn., 2012.
- 20 Smith, S. D.: Coefficients for sea surface wind stress, heat flux, and wind profiles as a function of wind speed and temperature, *Journal of Geophysical Research: Oceans*, 93(C12), 15 467–15 472, doi:10.1029/JC093iC12p15467, 1988.
- Takahashi, T., Sutherland, S. C., Wanninkhof, R., Sweeney, C., Feely, R. A., Chipman, D. W., Hales, B., Friederich, G., Chavez, F., Sabine, C., Watson, A., Bakker, D. C., Schuster, U., Metzl, N., Yoshikawa-Inoue, H., Ishii, M., Midorikawa, T., Nojiri, Y., Körtzinger, A., Steinhoff, T., Hoppema, M., Olafsson, J., Arnarson, T. S., Tilbrook, B., Johannessen, T., Olsen, A., Bellerby, R., Wong, C., Delille, B., Bates, N., and
 25 de Baar, H. J.: Climatological mean and decadal change in surface ocean pCO_2 , and net sea–air CO_2 flux over the global oceans, *Deep Sea Research Part II: Topical Studies in Oceanography*, 56, 554 – 577, doi:http://dx.doi.org/10.1016/j.dsr2.2008.12.009, surface Ocean CO_2 Variability and Vulnerabilities, 2009.
- Takahashi, T., Sutherland, S. C., Chipman, D. W., Goddard, J. G., Newberger, T., and Sweeney, C.: Climatological distributions of pH, pCO_2 , total CO_2 , alkalinity, and CaCO_3 saturation in the global surface ocean. ORNL/CDIAC-160, NDP-094., Carbon Dioxide Information
 30 Analysis Center, Oak Ridge National Laboratory, U.S. Department of Energy, Oak Ridge, Tennessee, doi:10.3334/CDIAC/OTG.NDP094, 2014.
- Vazquez-Cuervo, J., Dewitte, B., Chin, T. M., Armstrong, E. M., Purca, S., and Alburquerque, E.: An analysis of SST gradients off the Peruvian Coast: The impact of going to higher resolution, *Remote sensing of environment*, 131, 76–84, 2013.
- Wanninkhof, R.: Relationship between wind speed and gas exchange over the ocean, *Journal of Geophysical Research: Oceans*, 97, 7373–
 35 7382, doi:10.1029/92JC00188, 1992.
- Wanninkhof, R.: Relationship between wind speed and gas exchange over the ocean revisited, *Limnology and Oceanography: Methods*, 12, 351–362, doi:10.4319/lom.2014.12.351, 2014.

Submesoscale CO₂ variability across an upwelling front off Peru

Eike E. Köhn¹, Sören Thomsen¹, Damian L. Arévalo-Martínez¹, and Torsten Kanzow²

¹GEOMAR Helmholtz Centre for Ocean Research Kiel, Kiel, Germany

²Alfred-Wegener-Institute Helmholtz Centre for Polar and Marine Research, Bremerhaven, Germany

Correspondence to: Eike E. Köhn (ekoehn@geomar.de)

Abstract. While being a major source for atmospheric CO₂, the Peruvian upwelling region exhibits strong variability in surface $f\text{CO}_2$ on short spatial and temporal scales. Understanding the physical processes driving the strong variability is of fundamental importance for constraining the effect of marine emissions from upwelling regions on the global CO₂ budget. In this study, a frontal decay on length scales of $\mathcal{O}(10 \text{ km})$ was observed off the Peruvian coast following a pronounced decrease in downfrontal (equatorward) wind speed with a time lag of 9 hours. Simultaneously, the sea-to-air flux of CO₂ on the inshore (cold) side of the front dropped from up to 80 to 10 mmol m⁻² day⁻¹, while the offshore (warm) side of the front was constantly outgassing at a rate of 10-20 mmol m⁻² day⁻¹. Based on repeated ship transects the decay of the front was observed to occur in two phases. The first phase was characterized by a development of coherent surface temperature anomalies which gained in amplitude over 6-9 hours. The second phase was characterized by a disappearance of the surface temperature front within 6 hours. Submesoscale mixed layer instabilities were present but seem too slow to completely remove the temperature gradient in this short time period. Dynamics such as a pressure driven gravity current appear to be a likely mechanism behind the evolution of the front.

1 Introduction

Although the ocean generally acts as a net sink for atmospheric CO₂ (Takahashi et al., 2009), most low latitude eastern boundary upwelling systems (EBUS) are natural sources of CO₂ to the atmosphere (Chavez et al., 2007; Capone and Hutchins, 2013; Gruber, 2015). The distribution of CO₂ in such areas is complex and results from the interaction between cooling/warming at the surface, upwelling and mixing, biological activity, and riverine carbon and nutrient input (Laruelle et al., 2014; Gruber, 2015). As one of the four major EBUS, the Peruvian upwelling region is an important area for the exchange of climate relevant gases (e.g. CO₂, N₂O) between the ocean and the atmosphere (Friederich et al., 2008; Arévalo-Martínez et al., 2015). Hence, quantification of sea-to-air fluxes of CO₂ as well as their spatial and temporal variability in the Peruvian upwelling region is essential for constraining the global budget of CO₂ in a changing climate.

High variability of surface CO₂ in the Peruvian upwelling region is observed on short time $\mathcal{O}(\text{hours-days})$ and space $\mathcal{O}(\text{km})$ scales driven by both biological and physical processes (Friederich et al., 2008). The sharp lateral temperature gradient, separating the newly upwelled, cold water from warm surface waters further offshore, allows for pronounced frontal processes, which manifest themselves in eddies and filaments (Penven et al., 2005; Chaigneau et al., 2008; McWilliams et al., 2009; Colas et al., 2012; Thomsen et al., 2016a). These submesoscale features, which go along with Rossby numbers $Ro = \mathcal{O}(1)$,

can develop strong vertical velocities in the upper ocean layer. Thus, surface fronts may enable the exchange of large amounts of heat and gas between the atmosphere and the subsurface ocean (Ferrari, 2011). However, submesoscale frontal processes are difficult to observe due to their small spatial and temporal scales. At the same time the importance of these dynamics for physical-biogeochemical coupling has been put forward by model studies, e.g. by altering the vertical transports of nutrients and organic carbon (Lapeyre and Klein, 2006; Lévy et al., 2012).

The link between the surface CO₂ distribution and the (sub-) mesoscale flow field was studied in the open ocean of the Northeast Atlantic by Merlivat et al. (2009), using both underway and lagrangian surface drifter measurements. During the measurement period, the study area was characterized by weak eddy kinetic energy. Still, submesoscale variability with large amplitude variations of surface CO₂ concentrations on horizontal length scales of $\mathcal{O}(10 \text{ km})$ was observed. This variability was successfully reproduced by the modelling study of Resplandy et al. (2009) but it does not seem to have a major effect on the model's overall CO₂ budget. The influence of submesoscale variability on the overall CO₂ budget might be stronger in the case of EBUS due to the ubiquitous existence of sharp fronts and filaments, i.e. in the case of a highly energetic (sub-) mesoscale flow field (McWilliams et al., 2009; Colas et al., 2012). However, so far no observations are available which describe the variability on the submesoscale off Peru.

In this study repeated measurements of CO₂ and physical properties across the upwelling front off Peru near 14° S are presented (see Fig. 1 for the large scale setting of the experiment). Throughout the two day experiment, we observed short-term fluctuations (timescales on $\mathcal{O}(\text{hours})$) of the surface temperature and velocity field. Simultaneously, surface CO₂ sea-to-air fluxes showed pronounced changes, implicating the importance of these timescales for the ocean-atmosphere gas exchange. The goal of this paper are to: 1) document the high-frequency variability across the upwelling front and 2) discuss possible physical driving mechanisms, improving our current understanding of the variability of surface CO₂ in the Peruvian upwelling region.

This paper is structured as follows: In section 2 we present the experiment, the physical and biogeochemical datasets used for this study, as well as the methods employed for their analysis. Section 3 contains a description of the initial state of the front. Observations from the following frontal evolution are presented in section 4. Subsequently, the changes across the temperature front are analyzed in the context of various possible underlying dynamics, such as surface heating (Section 4.1), Ekman buoyancy fluxes (Section 4.2), submesoscale mixed layer instabilities (Section 4.3) or pressure driven gravity currents (Section 4.4). In section 5 these mechanisms are compared with respect to their associated buoyancy fluxes. Section 6 contains a discussion of the different mechanisms which possibly drive the observed variability. The conclusions drawn from this study follow in section 7.

2 Data and methods

2.1 Hydrographic and meteorological measurements

Near 14° S and 76°30' W the Peruvian upwelling region is characterized by a strong (quasi-) permanent upwelling cell (Fig. 1). The corresponding “upwelling front” was intensively sampled from February 16 to 18 during the RV *Meteor* cruise M93

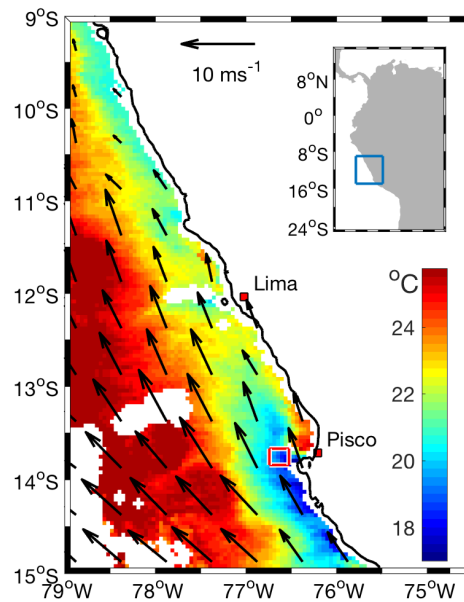


Figure 1. MODIS SST (color) and ASCAT (Advanced Scatterometer) wind field (arrows) off the Peruvian coast on February 16, 2013. The small red box shows the study region off Pisco.

in February/March 2013. The field work was carried out within the framework of the Collaborative Research Centre SFB754 “Climate-Biogeochemistry Interactions in the Tropical Ocean” (www.sfb754.de). The experiment’s procedure was as follows: Prior to the main experiment, a CTD section (transect “A”, black squares in Fig. 2) was conducted on February 16 from 10:00 to 15:00 (time always in UTC unless stated differently) to document the horizontal circulation and the initial vertical
 5 distribution of temperature, salinity, dissolved oxygen (O_2) and chlorophyll-*a* (Chl-*a*) across the front. Starting on February 17 at 04:00, the upwelling front was mapped by seven ~ 10 km long zonal transects. These were conducted from north to south in 1.8 km spacing (Fig. 2). Each zonal transect took about 45 minutes. From the highest and lowest surface temperature recorded, a cross-frontal axis was estimated. Subsequently, 17 cross-frontal transects were conducted along this axis to study the variability of the front on timescales of several hours. Among these, two high-resolution temperature sections “B” and “C”
 10 were conducted as cross-frontal transects 12 and 14. The high-resolution transects took 4.5 hours each to complete, while a regular cross-frontal transect was completed in 40 minutes. The cross-frontal transects were conducted within a 1.8 km wide corridor on three parallel tracks (Fig. 2).

The physical state of the upwelling front is mainly deduced from underway temperature, wind and velocity measurements. Underway temperature was measured by the thermosalinograph using an external SBE-38 digital thermometer at 3.5 - 4 m
 15 depth at the vessel’s port-side bow. Temperature data was gathered at 0.1 Hz and filtered by a 2nd order lowpass butterworth filter with a cutoff period of 250 seconds to remove the effect due to high frequent ship movements. Wind velocity and direction

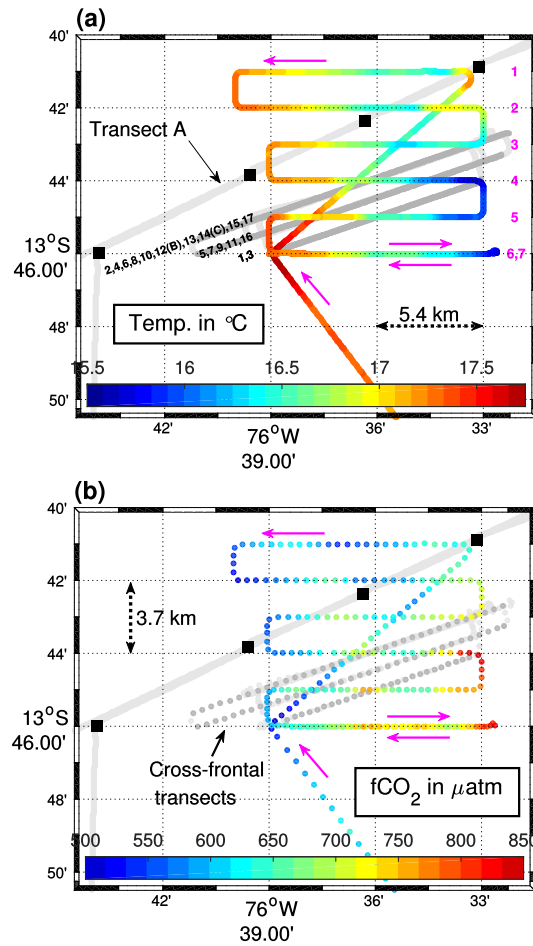


Figure 2. Sampling map of underway temperature (a) and $f\text{CO}_2$ (b) along the cruise track. The solid light grey line shows the CTD section (transect A) conducted prior to the seven zonal transects, with black squares indicating CTD stations. The 17 cross-frontal transects are marked by the dark grey lines (a) and dots (b). The black numbers in (a) correspond to the cross-frontal transects. Transects 12 and 14 correspond to the high-resolution subsurface temperature transects B and C. Magenta arrows show the direction of the ship's track and magenta numbers label the zonal transects. The area presented in both panels is depicted as a red square in Fig. 1.

were measured at a height of 35.3 m above the sea surface at a temporal resolution of 60 seconds. The surface wind stress was estimated from these measurements following Smith (1988). Underway ocean current velocity measurements with a vertical resolution of 4 m were obtained from a vessel-mounted 75 kHz ADCP (vmADCP). The shallowest vmADCP based current velocities were obtained in a bin centered at 11 m below the sea surface. The data was averaged in 1-minute-ensembles and smoothed using a 3-minute running mean. A 16.56° counterclockwise rotation is applied to transform the measured currents into along-front and cross-front velocities (note the frontal orientation in Fig. 2). As a result positive cross-front velocities are directed towards the coast and positive along-front velocities indicate an equatorward flow. Underway measurements of salinity

are unavailable as the thermosalinograph's conductivity sensor failed to produce consistent results. Likewise, temperature and vmADCP measurements taken during periods of highly variable vessel speed and heading proved to be unreliable due to the influence of the ship. Thus, current measurements immediately before and after CTD stations are neglected in the following data analysis. During the analyzed transects the vessel speed was held at approximately constant 4 m s^{-1} in order to achieve high quality ADCP data.

Hydrographic data *below* the surface were obtained from lowered conductivity, temperature and pressure (CTD) measurements. These are arranged in transect "A" consisting of four shallow CTD profiles located 7 km apart (black squares in Fig. 2). The CTD was equipped with a fluorometer and an oxygen sensor, allowing for Chl-*a* and O_2 measurements. A detailed description of the data processing, including the calibration of oxygen can be found in Thomsen et al. (2016b). As the Chl-*a* concentrations measured by the WET Labs (USA) fluorometer did not differ significantly from Chl-*a* concentrations determined from water samples (Meyer et al., 2017), no further calibration than the in-factory calibration was applied to the fluorometer data (see Loginova et al. (2016) for details). In order to obtain further subsurface hydrographic information, 53 temperature profiles organized in the two cross-frontal transects B and C with a horizontal resolution of 0.3 - 0.5 km were measured using the CTD sensors mounted on a microstructure profiler. During these measurements the speed of the vessel was reduced to about 0.75 m s^{-1} .

Surface diabatic heating was calculated from underway measurements as $Q_{net} = Q_{lw} + Q_{sw} + Q_{sh} + Q_{lh}$, i.e. the sum of longwave and shortwave radiation as well as sensible and latent heat fluxes. Net shortwave radiation into the ocean was estimated using underway measurements of downward shortwave radiation under consideration of the surface albedo effect (Payne, 1972). Net longwave radiation into the ocean was calculated as the difference between the measured downward longwave radiation and outgoing longwave radiation estimated using Stefan-Boltzman's law (with an emissivity of 0.985) applied to the thermosalinograph's temperature measurements. Latent and sensible heat fluxes along the cruise track were calculated using bulk formulae including the Webb-correction to the latent heat flux (Fairall et al., 1996b). During the experiment an average flux of latent heat of 20 W m^{-2} into the ocean was observed. This coincided with high relative humidity and partially foggy conditions. Neither a cool skin nor a warm skin correction is applied to the thermosalinograph's temperature measurements. A cool-skin would primarily form during night time, but is estimated to be on average less than 0.02 K cooler than the temperature measured by the thermosalinograph (Fairall et al., 1996a). A potentially larger warm-skin correction, which would increase outgoing longwave radiation mainly during periods of strong insolation, is not applied. This error in heatflux is however small compared to the dominant heatflux related to shortwave radiation during daytime.

The large scale sea surface temperature (SST) was retrieved from NASA's OceanColor project as daily satellite MODIS Aqua und Terra SST data (<https://oceancolor.gsfc.nasa.gov/>). For the large scale wind field Advanced Scatterometer (ASCAT) wind data (Bentamy and Fillon, 2012) was taken from the Asia-Pacific Data-Research Center at the University of Hawai'i (<http://apdrc.soest.hawaii.edu/datadoc/ascap.php>). The spatial resolution of SST was 4 km, while the wind data was available on a 0.25° grid. The ubiquitous presence of clouds during the main experiment period hindered an extensive use of remote sensing datasets.

2.2 Underway CO₂ measurements

CO₂ measurements were conducted by means of an underway system as described in Arévalo-Martínez et al. (2013). Seawater was drawn on board from a depth of about 6 m by means of a LOWARA submersible pump which was installed at the ship's moonpool. Atmospheric measurements were carried out every six hours by means of an AirCadet pump (Thermoscientific Inc., USA) which continuously brought air from 35 m height into the laboratory. Likewise, control measurements of standard gas mixtures with 201.0 and 602.4 ppm CO₂ were used in order to post-correct our data due to instrumental drift. The gas standards were prepared at Deuste Steininger GmbH (Mühlhausen, Germany) and were calibrated at the Max Planck Institute for Biogeochemistry (Jena, Germany) against the World Meteorological Organization standard scale. CO₂ data calibration as well as computation of CO₂ fugacities ($f\text{CO}_2$) was done according to the guidelines from Dickson et al. (2007). We report all seawater and atmospheric CO₂ values as 1-minute means. For this, we used a mean surface salinity from all CTD measurements of the M93 campaign (35.04), as salinity was not available from underway measurements. A change in the mean salinity by 1 leads to a mean offset of 0.0055 μatm and has thus a small influence compared to temperature with an isochemical dependence of 15 μatm per °C (e.g. Körtzinger et al. (2000); Pierrot et al. (2009)). The uncertainty of the CO₂ measurements was hence about $\pm 2 \mu\text{atm}$. The air-sea flux of CO₂ was computed by using $F = kK_0(f\text{CO}_{2\text{sw}} - f\text{CO}_{2\text{air}})$, where k is the air-sea gas exchange coefficient, calculated using the parameterization of Nightingale et al. (2000) with wind speeds standardized to 10 m height (Smith, 1988). K_0 is the solubility of CO₂ in seawater, calculated with the equations and coefficients from Weiss (1974) and Weiss and Price (1980), and $f\text{CO}_{2\text{sw}}$ and $f\text{CO}_{2\text{air}}$ are the fugacities of CO₂ in seawater and atmosphere, respectively. The strongest correlation between the underway temperature and $f\text{CO}_2$ measurements was found at a time lag of 4 minutes ($r = -0.86$) (Fig. 3), which is probably due to the travel time for the seawater from the uptake to the underway CO₂ sensor. Thus CO₂ fugacities and fluxes are corrected for this time lag.

3 Physical and biogeochemical properties of the upwelling front

The experiment period can be divided into three different wind forcing regimes. The first regime is characterized by downfrontal (equatorward) winds with speeds above 10 m s⁻¹ (Fig. 4). It lasts from the beginning of the experiment including the CTD transect (Fig. 5) until February 17 11:00, i.e. right after the beginning of the cross-frontal transects. During this phase, the front is characterized by a strong cross-frontal surface temperature gradient of about 1°C over 10 km (Fig. 6a). The CTD transect reveals the strong subsurface frontal signature in the temperature and salinity field (Fig. 5b,c). The mixed layer exhibits almost vertical isopycnals and is estimated to be about 15 m deep, using a $\Delta T = 0.2$ °C criterion. The southward flowing Peru Chile Undercurrent (PCUC) weakens from ~ 20 cm s⁻¹ at 80 meters depth towards the surface (Fig. 5a). The along-frontal velocity is low in the shallowest ADCP bin throughout the experiment (Fig. 7). As a result, lateral along-frontal advection is likely to play a minor role at the surface. In agreement with extensive upwelling of cold, nutrient rich waters during the strong wind period the Chl-*a* concentrations on the onshore side of the front were strongly enhanced with concentrations reaching 7 $\mu\text{g l}^{-1}$ in the mixed layer (Fig. 5e). Simultaneously, the subsurface O₂ minimum was drawn closer to the surface on the onshore side of the front (Fig. 5d). Concentrations below 100 $\mu\text{mol kg}^{-1}$ could be found at 15 m depth and values dropped below 20 μmol

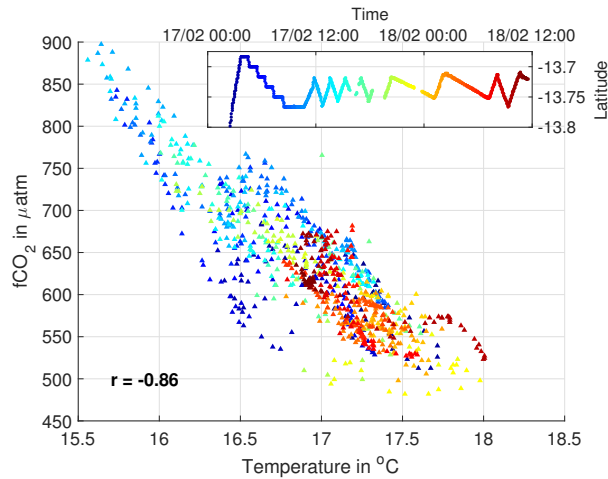


Figure 3. Correlation of surface temperature and $f\text{CO}_2$ during the main experiment. The $f\text{CO}_2$ values are corrected for a 4 minute time lag. The correlation value r is given in the bottom left corner. Data points are color-coded by their time of measurement. The top right box shows an orientation as to when the data was measured during the experiment. The color-coding carries the same information as the time axis.

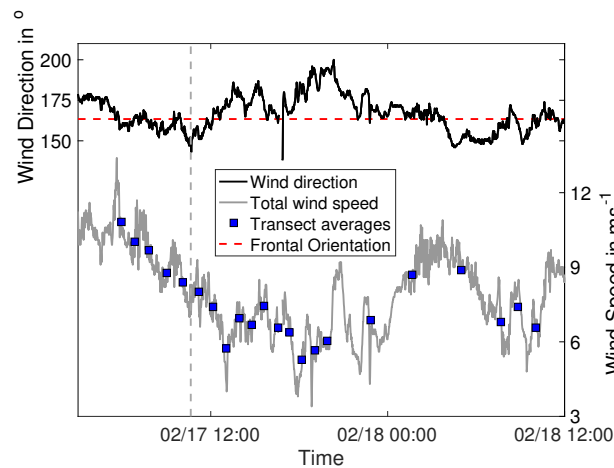


Figure 4. Time series of total wind speed (grey) and wind direction (black) from underway measurements at 35.3 m height. Blue rectangles show mean total wind speed for each zonal and cross-frontal transect. The dashed red line shows the (initial) frontal orientation deduced from the frontal mapping. The angle of 163.44° implicates the front running from south-south-east to north-north-west. The vertical dashed grey line indicates the transition from zonal to cross-frontal transects. Time is given in UTC.

kg^{-1} already beneath ~ 40 m. Further, a gradient in surface $f\text{CO}_2$ was discernible during the CTD transect (not shown) and during the zonal ship sections across the front (Fig. 2b), increasing from $600 \mu\text{atm}$ in offshore locations up to over $800 \mu\text{atm}$ on the onshore side of the front. During this period, peak sea-to-air CO_2 fluxes of over $80 \text{mmol m}^{-2} \text{d}^{-1}$ are measured on the cold side of the front (Fig. 6d).

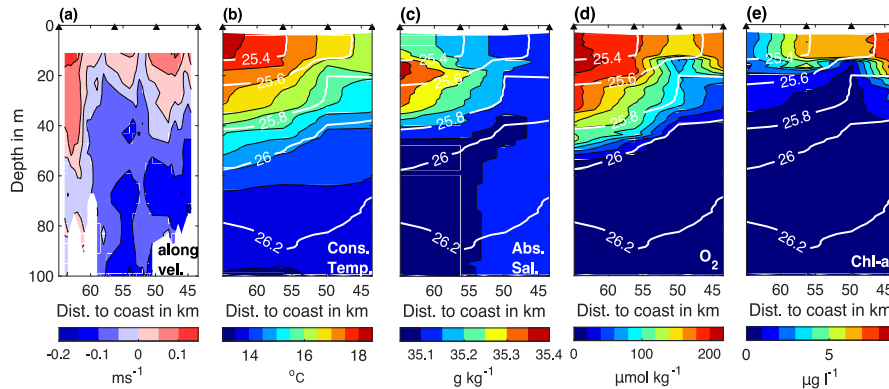


Figure 5. CTD transect across the upwelling front before the main experiment conducted on February 16, 2013. Measured quantities contain along-frontal current velocities (a), conservative temperature (b), absolute salinity (c), O₂ (d) and Chl-*a* concentrations (e). Isopycnals are given by white lines in (b) - (e). Around CTD stations the along-frontal velocity is horizontally linearly interpolated.

4 Cross-frontal changes after weakening of downfrontal winds

During the second wind period from 11:00 to 21:00 on February 17 the wind continues to blow in the downfrontal direction but drops to almost 5 m s^{-1} (Fig. 4). During this period the clear surface temperature gradient signal is disturbed by coherent anomalies appearing at 50 km off the coast (Fig. 6b). These anomalies grow in amplitude and lead to a break up of the clear temperature gradient at around 20:00. At the same time the strong outgassing of CO₂ is reduced on the onshore side of the front (Fig. 6d), while surface *f*CO₂ values remain rather high until about 18:00 (Fig. 6c). At the beginning of the transition to the low wind speed period, a strong offshore directed velocity signal is observed close to the surface on the onshore side of the front (Fig. 7a). The velocity maximum of up to 15 cm s^{-1} deepens with increasing distance from shore. During the wind minimum, maximum offshore velocities are found at 25-30 m depth, exceeding 20 cm s^{-1} (Fig. 7c). At the same time, the along-frontal velocity field exhibits a slight reduction in vertical shear (Fig. 7b,d).

At about 21:00 on February 17 the along-frontal (equatorward) wind begins to increase again and reaches about 9 m s^{-1} , defining the beginning of the third wind regime. Initially, the surface temperature gradient vanishes and even reverses slightly, before strengthening again towards February 18 09:00. Both high-resolution temperature transects (B and C) exhibit an average mixed layer depth of 3 and 5 m respectively (Fig. 8). The sections show that temperature changes are not limited to the surface layer but reach about 40-50 m deep. While the temperature field in transect B exhibits a clear frontal structure, the isotherms are close to horizontal in transect C, with exception of undulations associated with internal waves propagating onshore (e.g. at km 46 in Fig. 8b). As a result, the mean cross-frontal velocity field shows no longer any clear offshore directed velocity signal (Fig. 7e). Also the subsurface along-frontal (poleward) velocity maximum of the PCUC appears to be weaker (Fig. 7f). During this last phase the outgassing of CO₂ is at its minimum with fluxes less than $20 \text{ mmol m}^{-2} \text{ d}^{-1}$ despite the again increased wind speeds (Fig. 6d). *f*CO₂ remains at $\sim 600 \text{ } \mu\text{atm}$ during this phase and increases only slightly along the last two transects during which the front starts to reform.

Figure 3 shows the correlation of surface temperature and $f\text{CO}_2$ during the main experiment. The high negative correlation indicates the governing effect of temperature on the CO_2 field. Especially during the beginning of the experiment the high $f\text{CO}_2$ values are only found on the cold side of the front. Towards the end of the experiment the clear correlation signal breaks up. The changes in temperature and $f\text{CO}_2$ are observed over the course of $\mathcal{O}(\text{hours})$, giving phytoplankton only a short time window to react. It is thus likely that physical processes are mainly responsible for the measured variability in surface $f\text{CO}_2$. In the following part of this study, we analyze the observed changes across the upwelling front in the context of physical processes that could be responsible for driving the observed $f\text{CO}_2$ variability.

4.1 Surface heat fluxes

The changes across the front are observed within a 24 hour period. The wind begins to drop at 11:00 on February 17 (06:00 local time) and the temperature gradient fully vanishes 14 hours later at 01:00 on February 18 (Fig. 6a). As this time period matches well with the diurnal cycle of solar insolation, it could be hypothesized that differential heating throughout the day causes the reduction of the cross-frontal temperature gradient. Figure 6f shows the diurnal cycle of net surface heat flux. During the zonal transects the ocean surface is heated on average by 50 W m^{-2} . Due to the absence of solar insolation, this heatflux is mostly maintained by latent and sensible heat fluxes *into* the ocean, overcoming the ocean's weak heat loss caused by outgoing long wave radiation (individual heat flux components not shown). At around 12:00 (07:00 local time) the net heat flux into the ocean begins to strengthen, associated with an intensification of solar insolation. During the fourth and the beginning of the fifth cross-frontal transect the heat flux into the ocean is hampered due to irregularities in the incoming shortwave radiation. The net heat flux reaches its peak of 1010 W m^{-2} at 18:00 (13:00 local time) and reduces subsequently. From 23:00 (18:00 local time) onwards, the net heat flux fluctuates around 0 W m^{-2} . During the last cross-frontal transects the surface is continuously cooled by less than 50 W m^{-2} . During the phase of strongest heating, the heat flux shows only small lateral differences of mostly less than 50 W m^{-2} across the temperature front. Further, no clear pattern of slightly stronger heating on the cold side of the front is discernible. As a result, a uniform warming of the surface waters is expected. Sectional averaging of the first 13 cross-frontal transects, corresponding to the time period of incoming solar radiation, shows an increase of the transects' mean temperature of 0.8°C . From $\Delta Q = \rho_r c_p V \Delta T$ with the reference density $\rho_r = 1035 \text{ kg m}^{-3}$ and a heat capacity $c_p = 4000 \text{ J kg}^{-1} \text{ m}^{-3}$ it can be roughly estimated that over the same time period of 14.5 hours the average net heat flux causes a warming of a surface water column of volume V with unit area and 10 m depth by 0.6°C . Thus, the background temperature increase is most likely linked to the surface heat fluxes. The small scale temperature anomalies develop during the phase of strong heating (Fig. 6b). Using the same calculation as above the maximum heatflux of 1010 W m^{-2} can warm the surface water by almost 0.1°C per hour. Even though this roughly corresponds to the amplitude of the temperature anomalies, the lateral homogeneity of the net surface heat flux prohibits to attribute the development of the anomalies to surface heating.

The temperature front finally vanishes during a phase of almost no net surface heat flux. The high-resolution temperature transects B and C (Fig. 8) show, that during this phase, cooling takes place on the offshore side of the front, while the onshore side is significantly warmed over a period of 6 hours. On the onshore side, temperature changes of $\sim 2^\circ\text{C}$ occur up to ~ 40 m depth. A heatflux of $\sim 3800 \text{ W m}^{-2}$ is required to heat a water column of 40 m by 0.5°C using the rough estimate above.

Likewise, a comparably strong cooling is required on the offshore side of the front in order to explain the observed temperature changes. Neither the two heatfluxes nor the associated strong cross-frontal gradient are within the range of the observed values.

The net surface heat flux can be converted into a vertical buoyancy flux following $\langle w'b' \rangle_{Q_{net}} = \alpha g Q_{net} / (\rho c_p)$, where w' is the vertical velocity anomaly, b' is the buoyancy anomaly, g is the gravitational acceleration and α is the thermal expansion coefficient. Due to the lack of data, the calculation of the surface density ρ requires an assumption about the salinity. The initial CTD section shows a surface salinity varying between 35.1 and 35.2 (Fig. 5c). Thus, the surface water density ρ is calculated using a constant salinity of 35.1, yielding an uncertainty of density in the range of 0.1 kg m^{-3} and in vertical buoyancy fluxes of 1%. The mean values of $\langle w'b' \rangle_{Q_{net}}$ for each transect are shown in Fig. 9. During both, night and day time, the surface layer gains buoyancy. In the night this vertical buoyancy flux is weak, with a rate of less than $1 \times 10^{-8} \text{ m}^2 \text{ s}^{-3}$. During the day, vertical buoyancy fluxes of more than $5 \times 10^{-7} \text{ m}^2 \text{ s}^{-3}$ act to stratify the surface layers.

While surface heat fluxes are shown to contribute to the overall evolution of the temperature field, they cannot explain the across-frontal variability. Especially, the observed temperature changes below the surface layer seem to be unconnected to surface heating. Thus, dynamical processes are investigated in the following to understand the reduction of the cross-frontal temperature gradient.

4.2 Ekman transport

Throughout the experiment the wind speed changed significantly from almost 12 m s^{-1} to 4 m s^{-1} , while the wind direction stayed almost parallel to the front in the same direction as the frontal jet, i.e. downfrontal (Fig. 4). The cross-frontal Ekman velocity is calculated as $u_{Ek} = \tau_0 / (f \rho_0 H_{ML})$, where $\tau_0 = \rho_{air} (c_d u_{10}^2)$ is the neutral along-frontal surface wind stress. The drag coefficient c_d and the along-frontal wind speed at 10 m height u_{10} are calculated following Smith (1988). The mean density within the Ekman layer ρ_0 is approximated by the surface density ρ . Assuming a mixed layer depth $H_{ML} = 10 \text{ m}$ Ekman current velocities reach up to 0.5 m s^{-1} and are always directed offshore (figure not shown). During the period of the developing surface temperature anomalies, the Ekman velocity drops to $\sim 0.1 \text{ m s}^{-1}$, agreeing with the observed cross-front velocities close to the surface (Fig. 7a,c). The large uncertainties in surface salinity lead to only minor errors in Ekman velocity of less than 10^{-3} m s^{-1} . The choice of the mixed layer depth has a far larger impact due to the inverse proportionality. For example choosing $H_{ML} = 5 \text{ m}$ leads to Ekman velocities larger by a factor of 2. The clear offshore direction of the Ekman transport is not affected by these uncertainties.

The wind driven Ekman transport is associated with a non-geostrophic overturning circulation in the vertical/cross-frontal plane (Thomas et al., 2008). For such an overturning circulation it is possible to infer the associated vertical buoyancy flux $\langle w'b' \rangle$. The Ekman buoyancy flux (EBF) is given by $\langle w'b' \rangle_{EBF} = \tau_0 \cdot \nabla b / (\rho_0 f)$ (Thomas and Lee, 2005), where f is the Coriolis parameter. ∇b is the cross-frontal buoyancy gradient, taken as the slope from a linear fit to the surface buoyancy across the front. Buoyancy is calculated as $b = -g(\rho - \rho_r) / \rho_r$ using a reference density $\rho_r = 1035 \text{ kg m}^{-3}$.

Calculating the buoyancy gradient with a constant salinity value of 35.1 g kg^{-1} is likely to yield an error for the Ekman buoyancy fluxes as the initial CTD transect indicates a cross-frontal surface salinity gradient of $-5 \times 10^{-3} \text{ g kg}^{-1} \text{ km}^{-1}$. Hence, this salinity gradient is imposed onto the mean value of 35.1 g kg^{-1} to estimate the cross-frontal buoyancy gradient. Figure

9 shows the buoyancy fluxes calculated for each transect. The EBF is enclosed by an uncertainty range related to the surface salinity gradient. The edges of this uncertainty range stem from the case of no cross-frontal salinity gradient and of double the initially observed cross-frontal gradient.

The downfrontal wind drives a continuous Ekman transport from the cold to the warm side of the front, thus acting to keep the isopycnals strongly tilted, rather than directly transporting warm water onshore. Correspondingly, the EBF is predominantly negative, signifying a destratification within the surface layer, inhibiting the slumping of isopycnals. During the cross-frontal transects, the EBF weakens drastically from $-1 \times 10^{-6} \text{ m}^2 \text{ s}^{-3}$ to $-2 \times 10^{-7} \text{ m}^2 \text{ s}^{-3}$. Only during cross-frontal transects 13-15 the buoyancy flux changes sign, which goes along with the turnaround of the surface temperature gradient (Fig. 6a) while the Ekman velocity continues to be directed offshore. Afterwards, during the reformation of the front towards the end of the experiment on February 18, the EBF returns to negative values.

The results above show, that the weakening of the temperature front is not directly caused by onshore Ekman transport. Still, the reduction in downfrontal (equatorward) wind speed and the associated weakening in offshore Ekman transport can change the frontal stability. During most of the experiment's duration, the EBF inhibited a slumping of isopycnals. However, this flux weakened over the course of the experiment, potentially allowing other processes such as surface heat fluxes or mixed layer instabilities to become more important.

4.3 Mixed layer instabilities (MLIs)

Baroclinic instabilities confined to the mixed layer are referred to as submesoscale mixed layer instabilities (MLI) (Haine and Marshall, 1998; Boccaletti et al., 2007). They act to restratify the mixed layer by extracting potential energy from horizontal density gradients within the vertically well mixed surface layer and convert this into eddy kinetic energy, by formation of mixed layer eddies which accomplish the cross-frontal transport and exchange. With their short timescales of $\mathcal{O}(f^{-1})$ submesoscale MLI are thought to be efficient in converting lateral density fronts to a stratified mixed layer. Their horizontal scales are given by $L = NH_{ML}/f$, where $N = \sqrt{g/\rho(\partial\rho/\partial z)}$ is the small but non-vanishing stratification within the mixed layer (Thomas et al., 2008). Based on the initial CTD transect A (shown in Fig. 5) this lengthscale L is calculated to be $2.5 \pm 1.5 \text{ km}$. The large error is accounting for the uncertainties in the mean mixed layer stratification, which is estimated to be $N \approx (6 \pm 4) \times 10^{-3} \text{ s}^{-1}$. The inverse of the growth rate of MLI ($2\pi/f$) can be used as the associated timescale which amounts to ~ 2.1 days in the present case. The proximity of the study region to the equator associated with relatively long inertial timescales, makes it possible to capture well the variability by means of underway measurements.

Repeated observations of coherent surface temperature anomalies and their intensification between 15:00 and 20:00 on February 17 around 50 kilometers away from the coast might indicate the development of MLI (Fig. 6b). Preceding their appearance are small anomalies in the current field averaged over the upper 40 m (Fig. 6e). There, the mostly southbound flow is reversing and weakly flowing northward, producing large relative vorticity values (cross-frontal transects 3, 4, 5). This points towards eddying structures which could be associated with MLI. The mixed layer depth, estimated by a $\Delta T = 0.2^\circ\text{C}$ criterion, shows a shallowing throughout the experiment. While the average mixed layer depth is 15 m during the CTD transect A it reduces to 3 and 5 m during transects B and C, respectively. We applied linear stability analysis, which provides vertical

modes of the growth of baroclinic instabilities (Brüggemann and Eden, 2014; Thomsen et al., 2014) to the laterally averaged stratification and geostrophic current shear profile from the initial CTD section (Fig. 10b,c). This analysis reveals the existence of both, a deep mesoscale mode and a shallow mode, confined to the mixed layer (Fig. 10a,d,e). The horizontal length scale of the deep mode is about 200 km, while it is only 8.7 km for the shallow mode. This length scale is of the same order of magnitude as the expected mixed layer deformation radius L and the size of the observed surface temperature anomalies. The initial growth rate of the shallow mode calculated from linear stability analysis is 0.5 day^{-1} . Once the instabilities grow too large, nonlinearities dominate the instability process and linear stability analysis may not provide a useful description of the evolution of the instabilities (Thomsen et al., 2014). However, the calculated growth rate is relatively slow compared to the observed rapid decline of the cross-frontal temperature gradient. Also the inferred shallow mode is limited to $\sim 15 \text{ m}$ depth, i.e. the mixed layer (Fig. 10e). Thus, instability-induced changes of the velocity field at 30 m depth would require an interaction with the deep mode (Fig. 10d).

Similar to Ekman dynamics, a secondary overturning circulation is driven by MLI. It is important to note, that while an EBF is associated with strong diapycnal mixing, pure mixed layer instabilities are of an adiabatic nature. According to Fox-Kemper et al. (2008) the vertical buoyancy flux due to MLI given by $\langle w'b' \rangle_{MLI} = CH_{ML}^2 (\nabla b)^2 / |f|$ (where $C = 0.08$ is a constant) always tends to reduce the lateral temperature gradient. Throughout the experiment the $\langle w'b' \rangle_{MLI}$ values are positive, indicating a restratification of the mixed layer. However, the buoyancy flux associated with MLI is in general about 10 times smaller than the EBF. During the stable front the buoyancy flux associated with MLI $\langle w'b' \rangle_{MLI}$ is less than $1 \times 10^{-7} \text{ m}^2 \text{ s}^{-3}$ and reduces afterwards. Calculations are done with $H_{ML} = 15 \text{ m}$ based on the CTD transect. This is likely to be an upper bound for the mixed layer depth during the main experiment, as transects B and C show a much shallower mixed layer. Both linear stability analysis and buoyancy flux estimates imply that MLI are present, acting to restratify the mixed layer, but seem to be too slow and too confined to the surface layer, such that observed changes at depth cannot be explained by MLI alone.

4.4 Surface gravity current

In the presence of lateral density gradients, an unforced surface mixed layer is subject to pressure driven gravity currents, where lighter water spreads on top of the denser waters on timescales below the inertial period, i.e. independent of rotational effects (e.g. Kao et al. (1977)). The observed decrease in downfrontal wind speed could therefore give rise to the spreading of a buoyant plume down the temperature gradient. The rapid decline and even a slight reversal of the temperature front is captured well by transects B and C (Fig. 8). Within 6 hours the structure of both the temperature and cross-frontal velocity fields changed significantly. While transect B still shows a pronounced (subsurface) frontal signature, the isotherms in transect C are close to being horizontal. The temperature field in transect C is subject to distortion through internal waves. At km 46, the undulating isotherms go along with an oscillating signal in cross-front velocity, agreeing with internal waves propagating up the continental shelf. The strong depression of isotherms at km 57 could be the onset of another internal wave signal. In transect B, the temperature and velocity field exhibit a strong anomaly at km 52.5. There, a narrow but strong depression of the temperature field coincides with a region of strong convergence in the cross-frontal direction. Unlike in transect C, the attribution of the depression of the isotherms to an internal wave signal is not straightforward as the velocity field does not

show an oscillating behaviour in the vicinity of the depression. This might be attributed to aliasing of the signal due to too few hydrographic observations, which do not capture the short period of the internal waves.

Any density (here temperature) front is associated with a cross-frontal pressure gradient. In coastal upwelling regimes, this pressure gradient is largely in geostrophic balance manifesting itself in an along-frontal jet. However, if the wind field setting up the frontal system becomes too weak, the tilted isopycnals might start to slump, with the light surface waters offshore pushing over the denser surface water located further onshore. Thus, baroclinic temperature fronts can be eroded by gravity currents flowing down the pressure gradient across the front. Observations from river plumes show that the head of a gravity current may excite large-amplitude internal waves (Nash and Moum, 2005). These are either arrested at the leading edge of the gravity current or may propagate ahead of it if the current's advection speed is lower than that of the wave propagation speed.

Assuming that the anomaly signals in transect B (at km 52.5) and C (at km 46) belong to the same internal wave package that propagates at the leading edge of the gravity current, a propagation speed of 0.4 m s^{-1} is estimated using a time difference of 4.5 hours and a distance of 6.5 km. In a simple 2-layer model, the propagation speed of the gravity current in deep ambient fluid is given by $c = \sqrt{g'H}$, where $g' = g\Delta\rho/\rho$ is the reduced gravity, $\Delta\rho$ is the density difference between the two layers and H is the thickness of the upper layer (Shin et al., 2004; Dale et al., 2008). Assuming a 2-layer problem in the observed frontal setup with $H = 30 \text{ m}$, as the average depth of the 15°C isotherm, and $g' = 5 \times 10^{-3} \text{ m s}^{-2}$ derived from densities calculated at 10 and 50 m depth, assuming a salinity of 35, the theoretical propagation speed c can be estimated to be 0.4 m s^{-1} , thus agreeing with the observed propagation speed. If the temperature anomalies in sections B and C represent an internal wave package propagating at the leading edge of a gravity current, the internal wave propagation speed estimates above qualify a density driven gravity current as a possible mechanism behind the abrupt degradation of the temperature front. In contrast to the other analyzed processes it is capable of explaining subsurface changes in the temperature field.

5 Comparison of buoyancy fluxes

Over the whole experiment, three of the four analyzed physical processes are comparable in terms of the associated vertical buoyancy fluxes (Fig. 9). The ratio

$$R_b = \frac{\langle w'b' \rangle_{Q_{net}>0} + \langle w'b' \rangle_{MLI} + \langle w'b' \rangle_{EBF>0}}{\langle w'b' \rangle_{Q_{net}<0} + \langle w'b' \rangle_{EBF<0}} \quad (1)$$

allows for a statement on the combined effect of the Ekman buoyancy flux, surface heating and MLI (Mahadevan et al., 2010; Taylor and Ferrari, 2011). The numerator only contains terms associated with stratification, i.e. positive buoyancy fluxes. For example the buoyancy flux associated with MLIs is always positive and thus appears only in the numerator. The EBF however changes sign during the experiment. During the parts of the experiment with positive EBF it will contribute to the term $\langle w'b' \rangle_{EBF>0}$ in the numerator. If the EBF is negative, its modulus will appear in the denominator as $\langle w'b' \rangle_{EBF<0}$.

The same applies to the surface heating buoyancy fluxes. As a result, if $R_b > 1$, the mixed layer is subject to restratification associated with a slumping of isopycnals, whereas $R_b < 1$ implies a destratification, i.e. mixing in the surface layer. During the time of the development of the coherent surface temperature anomalies (cross-frontal transects 7-11), the combination of the

three processes favor a restratification of the mixed layer (Fig. 9). Linear stability analysis confirms the existence of a shallow baroclinic mode, which shows growth rates of 0.5 d^{-1} on lengthscales of 8.7 km. The latter agrees well with the extent of the observed temperature anomalies and the mixed layer radius of deformation calculated from the initial CTD transect. While the temporal scale of the shallow mode is in agreement with the development of the surface temperature anomalies, its impact in the rapid decline of the temperature front around 00:00 on February 18 is probably low, as the growth rate at the initial phase of the instability seems too small. Further, the low associated buoyancy fluxes (Fig. 9) indicate that MLI may contribute only to a small degree to the observed change in the temperature gradient across the front.

In contrast, the buoyancy fluxes associated with surface heating and cross-frontal Ekman transport (Fig. 9) contribute to the changes in sign of the sum of the buoyancy flux (and to $R_b > 1$) during February 17. Even though the strength of the diabatic heating agrees well with the amplitude of the developing surface temperature anomaly, stronger than observed horizontal gradients in surface heating are required to induce the observed lateral differences in warming. Further, the nature of this buoyancy flux is purely vertical and thus unable to create horizontal gradients in the case of spatially uniform heating, opposed to buoyancy fluxes associated with MLI or Ekman dynamics, which are fully 3-dimensional.

The buoyancy flux related to a gravity current is mainly lateral. However, if the warm water spreads on top of the cold water on the onshore side of the front, a vertical buoyancy flux is induced. In a closed domain the mean vertical buoyancy flux can be estimated following $\partial E_p / \partial t \approx -\langle wb \rangle$ (Peltier and Caulfield, 2003; White and Helfrich, 2013), thus by comparing volume-averaged potential energies E_p at two different points in time t . In a 2-dimensional domain the volume-averaged potential energy is calculated as $E_p = (hd)^{-1} \int_d \int_0^h b z dz dx$, where d is the lateral distance and h is depth. Using a constant salinity value of 35 the buoyancy field is calculated for transects B and C. Considering the upper 70 m on the initially cold side of the front (i.e. only east of 52 km offshore) a vertical buoyancy flux of $2.7 \times 10^{-6} \text{ m}^2 \text{ s}^{-3}$ is estimated. Laterally extending the domain to the full transects B and C reduces the vertical buoyancy flux to $1.8 \times 10^{-6} \text{ m}^2 \text{ s}^{-3}$. As the transects B and C have no closed boundaries, the estimates carry large uncertainties. The pressure driven gravity current is however assumed to be fully captured by both transects so that its associated effect should be captured. In the context of a closed domain the subsurface temperature reduction on the initially warm side of the front could be associated with an upward suction of colder water balancing the downward pumping of surface water on the cold side of the front (Fig. 8).

The estimated flux due to the gravity current is much larger than the buoyancy fluxes associated with the other processes described above during the cross-frontal transects 12-14, regardless of the chosen cross-frontal width considered. Only the EBF during the beginning of the experiment is of the same order of magnitude.

6 Discussion

Gathering data from multiple ship surveys Friederich et al. (2008) observed oceanic outgassing of CO_2 in the Peruvian upwelling region throughout the year. On average the authors estimated a sea-to-air CO_2 flux of $5 \text{ mol m}^{-2} \text{ yr}^{-1}$. On seasonal timescales, the flux varied between 2.5 and $10 \text{ mol m}^{-2} \text{ yr}^{-1}$ associated with weak and strong upwelling periods, respectively. Although Friederich et al. (2008) focused on the large scale distribution of surface CO_2 fluxes and the associated mechanisms,

they further detected strong variability of CO₂ fluxes on short time and space scales ($\mathcal{O}(\text{hours-days})$ and $\mathcal{O}(\text{km})$), which contributes significantly to the overall CO₂ budget.

Motivated by their findings, the study presented here focuses on the pronounced submesoscale variability of surface CO₂ in the Peruvian upwelling region at 13.7° S. Our observations show CO₂ outgassing rates between 3.5 and 30 mol m⁻² yr⁻¹ which are in line with the outgassing signals observed by Friederich et al. (2008), even after accounting for the difference in converting our values from partial pressures to fugacities (difference usually about 3%). Our peak sea-air fluxes reaching up to 80 mmol m⁻² d⁻¹ are distinctly higher than the maximum flux of 12.4 mmol m⁻² d⁻¹ reported by Friederich et al. (2008) for a measurement campaign in the month of February. At the same time, our peak-flux is only slightly higher than maximum flux values reported from other months. The results from Friederich et al. (2008) were re-scaled to a much larger area (5° S - 15° S), have been subject of spatial extrapolation and smoothing, and were calculated with the sea-air gas exchange parameterization by Wanninkhof (1992) which tends to overestimate the gas transfer velocities (see Wanninkhof (2014)). Simply using the Wanninkhof (1992) parameterization instead of the Nightingale et al. (2000) parameterization yields 17% higher fluxes, already indicating that it is difficult to draw a direct comparison between both data sets. Nonetheless, both studies agree in that the near-coastal zone off Peru acts as a rather strong source of CO₂ to the atmosphere, and from our data it seems clear that the onshore side of the upwelling front could be associated with an important enhancement of CO₂ outgassing. The conditions observed in this study are not necessarily representative for February conditions. Many processes on different timescales can alter the upwelling frontal structure and intensity off Peru, for instance the state of the El Niño Southern Oscillation (Espinoza-Morriberón et al., 2017) or coastally trapped waves propagating along the Peruvian coast (Pietri et al., 2014). The aim of this study is rather to analyze a suite of processes involved in the evolution of the upwelling front and surface $f\text{CO}_2$ on short space and timescales ($\mathcal{O}(1 \text{ km})$, $\mathcal{O}(0.5 \text{ day})$).

The downfrontal wind is an important ingredient in maintaining tilted isopycnals in the surface layer. The EBF dominates all other buoyancy fluxes during the strong wind period (Fig. 9). In a study by Dale et al. (2008) a restratification of the mixed layer is observed in connection with a frontal decay in the upwelling system off Oregon on length scales comparable to those presented here. In their study, a reversal of the wind direction plays a crucial role in driving the frontal decay by inducing an Ekman transport down the cross-frontal pressure gradient. For the frontal decay presented here, the wind is always directed downfrontal and does not change significantly. The cross-frontal wind component is weak (mostly less than 3 m s⁻¹) and alternates in direction between onshore and offshore without any clear dominance (Fig. 4). As a result, Ekman transport and the associated buoyancy flux do not change direction. Still, the strong reduction in cross-frontal Ekman transport could potentially give way for other mechanisms.

Pronounced changes across the front are shown to occur in two steps after the distinct reduction in downfrontal wind speed with a time lag of about 9 hours. The first step is characterized by the gradual development and strengthening of coherent surface temperature anomalies, while the second is characterized by a sudden decline and even slight reversal of the temperature gradient. Transects B and C (Fig. 8) show that changes in the temperature field are thereby not limited to the surface layer, but reach down to 50 m. To identify the underlying processes, the frontal evolution is described above in a 2-dimensional framework, i.e. in the vertical/cross-frontal plane. The variability induced by along-frontal advection is neglected. This assumption

seems valid, as the along-frontal current velocities reduce close to zero in proximity to the surface (Fig. 7b,d,e). Further, the fact that the cross-frontal transects show coherent signals, even though not all cross-frontal transects were performed on the exact same track, but about 1 km apart, points towards a weak along-frontal flow variability. Still, the two dimensional framework allows for various hypotheses about the driving mechanisms behind the observed changes.

5 The analyses have shown that the diurnal surface heating is able to explain the majority of the mean increase in surface temperatures. During the phase of maximum heating the associated positive buoyancy flux into the ocean outweighs the permanent reduction in surface buoyancy by the downfrontal wind stress (Fig. 9). However, the spatially homogeneous heating is unable to account for the developing small-scale temperatures anomalies. As a result, submesoscale MLI have been investigated as they are shown to restratify the surface mixed layer and are thereby capable of generating lateral gradients and anomalies.

10 Linear stability analysis indeed shows the presence of a shallow baroclinic mode confined to the mixed layer (Fig. 10). While the length scale of this mode roughly meets the observed horizontal extent of the temperature anomalies and the mixed layer deformation radius, the instability seems to grow too slowly to be the dominant dynamical process involved in the frontal decay. Hence, also the vertical buoyancy fluxes associated with MLI are an order of magnitude smaller than those related to surface heating or Ekman dynamics (Fig. 9).

15 The low-latitude location of the experiment site at 13.77° S results in a rather long inertial time period of $T_{in} = 2\pi/f = 2.1$ days. Thus, the sudden changes observed from hydrographic sections B and C within a time span of 6 hours suggest that processes influenced by Earth's rotation, are potentially less important in the final weakening of the temperature front. Propagating buoyant plumes related to river discharge (Nash and Moum, 2005) or frontal zones in upwelling regimes (Walter et al., 2016) are common dynamical processes in continental shelf regions. In fact, Dale et al. (2008) also identified such

20 a pressure-driven gravity current propagating across the front, once the wind forcing had changed. For our case, using the limited amount of hydrographic information, a propagation speed of 0.4 m s^{-1} can be identified. This proves to match well with the theoretical estimate for a 2-layer system. The present stratification however complicates the distinction of a sharp density gradient to apply the gravity current theory. Further, stratified ambient water decreases the propagation speed of a gravity current compared to the two layer system (Ungarish and Huppert, 2002). Still, hinting towards the observation of a

25 gravity current, both transect B and C exhibit strong internal wave signals, which have been observed at the leading edge of such buoyant plumes (Nash and Moum (2005); Bourgault et al. (2016)). Of all mechanisms presented, the gravity current is the only one that may account for the fast changes up to 50 m depth. In contrast, the stability analysis suggests, that MLI are mainly active in the mixed layer and could only effect lower layers by interacting with the deep mode (Ramachandran et al., 2014; Capet et al., 2016).

30 In this study we set focus solely on the role of physical processes driving the small-scale distribution of $f\text{CO}_2$. We argue that the timescales considered here are too short to allow for significant contributions of biological processes in driving $f\text{CO}_2$ changes across the front. The strong correlation of surface temperature and $f\text{CO}_2$ imply that the $f\text{CO}_2$ variability is dominated by two processes: Firstly, the temperature dependent solubility of gases in seawater and secondly, warm offshore surface water pushing on top of CO_2 -enriched upwelled water, thus creating a mechanical barrier for air-sea gas exchange. However,

35 the weakening of the correlation over time (Fig. 3) indicates that other processes, such as biological activity, might become

increasingly important. A more thorough analysis from a biogeochemical perspective is needed, incorporating these effects (Mahadevan et al., 2004). Consistently, physical processes seem to be able to account for the small scale variability observed by Friederich et al. (2008) and understanding them could be crucial to establish a reliable CO₂ budget for the Peruvian upwelling region. Likewise, it is mandatory to have accurate observations of the near-shore wind field, as it proved to be an important
5 factor that contributes to the small-scale evolution of the upwelling front. Modern satellite wind products are still too coarse to resolve the submesoscale frontal variability or other small scale variations such as land-sea breezes or an enhanced near-shore wind stress curl. They are thus not fully reliable within 25 to 50 km from shore (Croquette et al., 2007; Albert et al., 2010).

7 Conclusions

High-resolution, underway measurements are a useful tool in observing submesoscale variability on scales of $\mathcal{O}(1)$ km. Pro-
10 nounced changes in the $f\text{CO}_2$ and temperature fields were observed across an upwelling front within hours, providing evidence of high short-term variability in the sea-air CO₂ exchange off Peru. We provide evidence of the complex submesoscale distribution of surface CO₂ in the Peruvian upwelling system and its tight connection to the strong variability in surface temperature. It thus appears that on these timescales the evolving $f\text{CO}_2$ distribution is controlled by physical processes.

Outgassing of CO₂ dropped from 80 mmol m⁻² d⁻¹ to less than 10 mmol m⁻² d⁻¹ within less than 24 hours. We showed
15 that this drastic change can be explained by physical processes associated with a weakening of the cross-frontal temperature gradient following a significant decrease in downfrontal (equatorward) windspeed. The initially geostrophically balanced front with a length scale of 10 km vanished within few hours, thereby removing a surface temperature difference of 1°C over 10 km. Hydrographic data shows pronounced changes in the temperature field at depths of up to 50 m. Despite the lack of direct onshore transport of warm water by Ekman dynamics, the wind played a major role in maintaining the front in the beginning of
20 the experiment. The decay of the downfrontal wind gave rise to the development of submesoscale mixed layer instabilities and potentially allowed for a gravity current to propagate down the cross-frontal pressure gradient. The mixed layer instabilities, however, appear to be too shallow and too slow to be able to account for the complete removal of the cross-frontal temperature gradient. Yet, the onset of a surface gravity current would be consistent with the observed changes in the subinertial period. In addition, our analysis shows that multiple processes act simultaneously and are likely to interact, thus complicating the
25 identification of a single, dominant mechanism responsible for the fast observed changes in surface $f\text{CO}_2$.

At present, a low CO₂ data coverage within the Peruvian upwelling region (e.g. in SOCAT, Bakker et al. (2016)) complicates the establishment of a reliable climatology, as done by Takahashi et al. (2014) or more recently Landschützer et al. (2017). From our study the importance of the wind and temperature variability on timescales of $\mathcal{O}(\text{hours})$ in setting the strength of sea-air CO₂ fluxes becomes obvious. When coupled with CO₂ measurements the use of sea surface temperature and wind products,
30 which capture the high temporal and spatial variability, could lead to improved future estimates of a CO₂ flux climatology off Peru. In order to understand the large scale impact of short-term variability of an upwelling ecosystem, a way forward would be the establishment of multi-platform observation networks in which continuous in situ data is complemented by satellite observations and measurements from autonomous platforms such as e.g. gliders, as for example conducted by Ohman et al.

(2013) in the California Current System. A further example are the moored CO₂ observations from Lefèvre et al. (2008) and Lefèvre and Merlivat (2012) which help to constrain regional budgets and variability of CO₂ for the Eastern Tropical Atlantic and could also be used to reliably estimate the net carbon community production in this area.

8 Data availability

- 5 According to the SFB 754 data policy (<https://www.sfb754.de/de/data>), all data associated with this publication are accessible upon publication under <https://doi.pangaea.de/10.1594/PANGAEA.881049>.

Author contributions. E. E. Köhn performed the analysis and wrote the manuscript. S. Thomsen designed the experiment and contributed to the manuscript. D. L. Arévalo-Martínez measured and provided the CO₂ data and contributed to the manuscript. T. Kanzow was chief scientist on M93, stimulated the analysis and gave scientific guidance. All authors reviewed and commented on the manuscript.

- 10 *Competing interests.* The authors declare that they have no conflict of interest.

- Acknowledgements.* This work is a contribution of the Sonderforschungsbereich 754 "Climate-Biogeochemistry Interactions in the Tropical Ocean" (www.sfb754.de), which is funded by the Deutsche Forschungsgemeinschaft (DFG). We are grateful to the Peruvian authorities for the permission to carry out scientific work in their national waters. Special thanks go to the captain and the crew of the R/V *Meteor* for their support during the M93 cruise. We are grateful to T. Steinhoff for making available the CO₂ sensor as well for his technical support during
- 15 the cruise. We further thank Liam Brannigan, Leah Johnson, Karl Bumke and the meteorologists of the DWD for helpful discussions of the results. D. L. Arévalo-Martínez received additional funding support through the BMBF funded SOPRAN II (FKZ 03F0611A) project, as well as the Future Ocean Excellence Cluster at Kiel University (CP0910), and the EU FP7 project InGOS (grant agreement 284274).

References

- Albert, A., Echevin, V., Lévy, M., and Aumont, O.: Impact of nearshore wind stress curl on coastal circulation and primary productivity in the Peru upwelling system, *Journal of Geophysical Research: Oceans*, 115, C12 033, doi:10.1029/2010JC006569, 2010.
- Arévalo-Martínez, D. L., Beyer, M., Krumbholz, M., Piller, I., Kock, A., Steinhoff, T., Körtzinger, A., and Bange, H. W.: A new method for continuous measurements of oceanic and atmospheric N₂O, CO and CO₂: performance of off-axis integrated cavity output spectroscopy (OA-ICOS) coupled to non-dispersive infrared detection (NDIR), *Ocean Science*, 9, 1071–1087, doi:10.5194/os-9-1071-2013, 2013.
- Arévalo-Martínez, D. L., Kock, A., Löscher, C. R., Schmitz, R. A., and Bange, H. W.: Massive nitrous oxide emissions from the tropical South Pacific Ocean, *Nature Geoscience*, 8, 530–533, doi:10.1038/ngeo2469, 2015.
- Bakker, D. C. E., Pfeil, B., Landa, C. S., Metzl, N., O'Brien, K. M., Olsen, A., Smith, K., Cosca, C., Harasawa, S., Jones, S. D., Nakaoka, S.-I., Nojiri, Y., Schuster, U., Steinhoff, T., Sweeney, C., Takahashi, T., Tilbrook, B., Wada, C., Wanninkhof, R., Alin, S. R., Balestrini, C. F., Barbero, L., Bates, N. R., Bianchi, A. A., Bonou, F., Boutin, J., Bozec, Y., Burger, E. F., Cai, W.-J., Castle, R. D., Chen, L., Chierici, M., Currie, K., Evans, W., Featherstone, C., Feely, R. A., Fransson, A., Goyet, C., Greenwood, N., Gregor, L., Hankin, S., Hardman-Mountford, N. J., Harlay, J., Hauck, J., Hoppema, M., Humphreys, M. P., Hunt, C. W., Huss, B., Ibáñez, J. S. P., Johannessen, T., Keeling, R., Kitidis, V., Körtzinger, A., Kozyr, A., Krasakopoulou, E., Kuwata, A., Landschützer, P., Lauvset, S. K., Lefèvre, N., Lo Monaco, C., Manke, A., Mathis, J. T., Merlivat, L., Millero, F. J., Monteiro, P. M. S., Munro, D. R., Murata, A., Newberger, T., Omar, A. M., Ono, T., Paterson, K., Pearce, D., Pierrot, D., Robbins, L. L., Saito, S., Salisbury, J., Schlitzer, R., Schneider, B., Schweitzer, R., Sieger, R., Skjelvan, I., Sullivan, K. F., Sutherland, S. C., Sutton, A. J., Tadokoro, K., Telszewski, M., Tuma, M., van Heuven, S. M. A. C., Vandemark, D., Ward, B., Watson, A. J., and Xu, S.: A multi-decade record of high-quality *f*CO₂ data in version 3 of the Surface Ocean CO₂ Atlas (SOCAT), *Earth System Science Data*, 8, 383–413, 2016.
- Bentamy, A. and Fillon, D. C.: Gridded surface wind fields from Metop/ASCAT measurements, *International Journal of Remote Sensing*, 33, 1729–1754, doi:10.1080/01431161.2011.600348, 2012.
- Boccaletti, G., Ferrari, R., and Fox-Kemper, B.: Mixed Layer Instabilities and Restratification, *Journal of Physical Oceanography*, 37, 2228–2250, doi:10.1175/JPO3101.1, 2007.
- Bourgault, D., Galbraith, P. S., and Chavanne, C. P.: Generation of internal solitary waves by frontally forced intrusions in geophysical flows, *Nature Communications*, 7, 13 606, doi:10.1038/ncomms13606, 2016.
- Brüggemann, N. and Eden, C.: Evaluating Different Parameterizations for Mixed Layer Eddy Fluxes induced by Baroclinic Instability, *Journal of Physical Oceanography*, 44, 2524–2546, doi:10.1175/JPO-D-13-0235.1, 2014.
- Capet, X., Roullet, G., Klein, P., and Maze, G.: Intensification of Upper-Ocean Submesoscale Turbulence through Charney Baroclinic Instability, *Journal of Physical Oceanography*, 46, 3365–3384, doi:10.1175/JPO-D-16-0050.1, 2016.
- Capone, D. G. and Hutchins, D. A.: Microbial biogeochemistry of coastal upwelling regimes in a changing ocean, *Nature Geoscience*, 6, 711–717, doi:10.1038/ngeo1916, 2013.
- Chaigneau, A., Gizolme, A., and Grados, C.: Mesoscale eddies off Peru in altimeter records: Identification algorithms and eddy spatio-temporal patterns, *Progress in Oceanography*, 79, 106–119, doi:10.1016/j.pocean.2008.10.013, 2008.
- Chavez, F. P., Takahashi, T., Cai, W.-J., Friederich, G., Hales, B., Wanninkhof, R., and Feely, R.: Coastal oceans, in: *The First State of the Carbon Cycle Report (SOCCR): The North American Carbon Budget and Implications for the Global Carbon Cycle*, edited by King, A. W., Dilling, L., Zimmerman, G. P., Fairman, D. M., Houghton, R. A., Marland, G., Rose, A. Z., and Wilbanks, T. J., A report by the U.S. Climate Change Science Program and the Subcommittee on Global Change Research, Washington, DC, 2007.

- Colas, F., McWilliams, J. C., Capet, X., and Kurian, J.: Heat balance and eddies in the Peru-Chile current system, *Climate Dynamics*, 39, 509–529, doi:10.1007/s00382-011-1170-6, 2012.
- Croquette, M., Eldin, G., Grados, C., and Tamayo, M.: On differences in satellite wind products and their effects in estimating coastal upwelling processes in the south-east Pacific, *Geophysical Research Letters*, 34, L11 608, doi:10.1029/2006GL027538, 2007.
- 5 Dale, A. C., Barth, J. A., Levine, M. D., and Austin, J. A.: Observations of mixed layer restratification by onshore surface transport following wind reversal in a coastal upwelling region, *Journal of Geophysical Research: Oceans*, 113, C01 010, doi:10.1029/2007JC004128, 2008.
- Dickson, A. G., Sabine, C. L., and Christian, J. R., eds.: Guide to best practices for ocean CO₂ measurements. PICES Special Publication 3, 191 pp., 2007.
- Espinoza-Morriberón, D., Echevin, V., Colas, F., Tam, J., Ledesma, J., Vásquez, L., and Graco, M.: Impacts of El Niño events on the Peruvian upwelling system productivity, *Journal of Geophysical Research: Oceans*, 122, 5423–5444, doi:10.1002/2016JC012439, 2017.
- 10 Fairall, C. W., Bradley, E. F., Godfrey, J. S., Wick, G. A., Edson, J. B., and Young, G. S.: Cool-skin and warm-layer effects on sea surface temperature, *Journal of Geophysical Research: Oceans*, 101, 1295–1308, doi:10.1029/95JC03190, 1996a.
- Fairall, C. W., Bradley, E. F., Rogers, D. P., Edson, J. B., and Young, G. S.: Bulk parameterization of air-sea fluxes for Tropical Ocean-Global Atmosphere Coupled-Ocean Atmosphere Response Experiment, *Journal of Geophysical Research: Oceans*, 101(C2), 3747–3764, 15 doi:10.1029/95JC03205, 1996b.
- Ferrari, R.: A frontal challenge for climate models., *Science*, 332, 316–317, doi:10.1126/science.1203632, 2011.
- Fox-Kemper, B., Ferrari, R., and Hallberg, R.: Parameterization of Mixed Layer Eddies. Part I: Theory and Diagnosis, *Journal of Physical Oceanography*, 38, 1145–1165, doi:10.1175/2007JPO3792.1, 2008.
- Friederich, G. E., Ledesma, J., Ulloa, O., and Chavez, F. P.: Air-sea carbon dioxide fluxes in the coastal southeastern tropical Pacific, *Progress in Oceanography*, 79(2-4), 156–166, doi:10.1016/j.pcean.2008.10.001, 2008.
- 20 Gruber, N.: Ocean biogeochemistry: Carbon at the coastal interface, *Nature*, 517, 148–149, doi:10.1038/nature14082, 2015.
- Haine, T. W. N. and Marshall, J.: Gravitational, Symmetric, and Baroclinic Instability of the Ocean Mixed Layer, *Journal of Physical Oceanography*, 28, 634–658, doi:10.1175/1520-0485(1998)028<0634:GSABIO>2.0.CO;2, 1998.
- Kao, T. W., Park, C., and Pao, H.-P.: Buoyant surface discharge and small-scale oceanic fronts: A numerical study, *Journal of Geophysical Research*, 82, 1747–1752, doi:10.1029/JC082i012p01747, 1977.
- 25 Körtzinger, A., Mintrop, L., Wallace, D. W., Johnson, K. M., Neill, C., Tilbrook, B., Towler, P., Inoue, H. Y., Ishii, M., Shaffer, G., et al.: The international at-sea intercomparison of *f*CO₂ systems during the R/V Meteor Cruise 36/1 in the North Atlantic Ocean, *Marine Chemistry*, 72, 171–192, 2000.
- Landschützer, P., Gruber, N., and C. E. Bakker, D.: An updated observation-based global monthly gridded sea surface pCO₂ and air-sea CO₂ flux product from 1982 through 2015 and its monthly climatology (NCEI Accession 0160558). Version 2.2. NOAA National Centers for Environmental Information. Dataset. [2017-07-11], 2017.
- 30 Lapeyre, G. and Klein, P.: Impact of the small-scale elongated filaments on the oceanic vertical pump, *Journal of Marine Research*, 64, 835–851, doi:10.1357/002224006779698369, 2006.
- Laruelle, G. G., Lauerwald, R., Pfeil, B., and Regnier, P.: Regionalized global budget of the CO₂ exchange at the air-water interface in continental shelf seas, *Global Biogeochemical Cycles*, 28, 1199–1214, doi:10.1002/2014GB004832, 2014.
- 35 Lefèvre, N. and Merlivat, L.: Carbon and oxygen net community production in the eastern tropical Atlantic estimated from a moored buoy, *Global biogeochemical cycles*, 26, 2012.

- Lefèvre, N., Guillot, A., Beaumont, L., and Danguy, T.: Variability of $f\text{CO}_2$ in the Eastern Tropical Atlantic from a moored buoy, *Journal of Geophysical Research: Oceans*, 113, 2008.
- Lévy, M., Ferrari, R., Franks, P. J. S., Martin, A. P., and Rivière, P.: Bringing physics to life at the submesoscale, *Geophysical Research Letters*, 39, doi:10.1029/2012GL052756, 2012.
- 5 Loginova, A. N., Thomsen, S., and Engel, A.: Chromophoric and fluorescent dissolved organic matter in and above the oxygen minimum zone off Peru, *Journal of Geophysical Research: Oceans*, 121, 7973–7990, doi:10.1002/2016JC011906, 2016.
- Mahadevan, A., Lévy, M., and Mémery, L.: Mesoscale variability of sea surface pCO_2 : What does it respond to?, *Global Biogeochemical Cycles*, 18, GB1017, doi:10.1029/2003GB002102, 2004.
- Mahadevan, A., Tandon, A., and Ferrari, R.: Rapid changes in mixed layer stratification driven by submesoscale instabilities and winds, *Journal of Geophysical Research*, 115, C03 017, doi:10.1029/2008JC005203, 2010.
- 10 McWilliams, J. C., Colas, F., and Molemaker, M. J.: Cold filamentary intensification and oceanic surface convergence lines, *Geophysical Research Letters*, 36, L18 602, doi:10.1029/2009GL039402, 2009.
- Merlivat, L., Gonzalez Davila, M., Caniaux, G., Boutin, J., and Reverdin, G.: Mesoscale and diel to monthly variability of CO_2 and carbon fluxes at the ocean surface in the northeastern Atlantic, *Journal of Geophysical Research*, 114, C03 010, doi:10.1029/2007JC004657, 15 2009.
- Meyer, J., Löscher, C. R., Lavik, G., and Riebesell, U.: Mechanisms of P^* Reduction in the Eastern Tropical South Pacific, *Frontiers in Marine Science*, 4, 1, doi:10.3389/fmars.2017.00001, 2017.
- Nash, J. D. and Moum, J. N.: River plumes as a source of large-amplitude internal waves in the coastal ocean, *Nature*, 437, 400–403, doi:10.1038/nature03936, 2005.
- 20 Nightingale, P. D., Malin, G., Law, C. S., Watson, A. J., Liss, P. S., Liddicoat, M. I., Boutin, J., and Upstill-Goddard, R. C.: In situ evaluation of air-sea gas exchange parameterizations using novel conservative and volatile tracers, *Global Biogeochemical Cycles*, 14(1), 373–387, doi:10.1029/1999GB900091, 2000.
- Ohman, M. D., Rudnick, D. L., Chekalyuk, A., Davis, R. E., Feely, R. A., Kahru, M., Jim, H.-J., Landry, M. R., Martz, T. R., Sabine, C. L., and Send, U.: Autonomous ocean measurements in the California Current Ecosystem, *Oceanography*, 26, 18–25, 2013.
- 25 Payne, R. E.: Albedo of the Sea Surface, *Journal of the Atmospheric Sciences*, 29, 959–970, doi:10.1175/1520-0469(1972)029<0959:AOTSS>2.0.CO;2, 1972.
- Peltier, W. R. and Caulfield, C. P.: Mixing efficiency in stratified shear flows, *Annual Review of Fluid Mechanics*, 35, 135–167, doi:10.1146/annurev.fluid.35.101101.161144, 2003.
- Penven, P., Echevin, V., Pasapera, J., Colas, F., and Tam, J.: Average circulation, seasonal cycle, and mesoscale dynamics of the Peru Current System: A modeling approach, *Journal of Geophysical Research*, 110, C10 021, doi:10.1029/2005JC002945, <http://doi.wiley.com/10.1029/2005JC002945>, 2005.
- 30 Pierrot, D., Neill, C., Sullivan, K., Castle, R., Wanninkhof, R., Lüger, H., Johannessen, T., Olsen, A., Feely, R. A., and Cosca, C. E.: Recommendations for autonomous underway pCO_2 measuring systems and data-reduction routines, *Deep Sea Research Part II: Topical Studies in Oceanography*, 56, 512–522, 2009.
- 35 Pietri, A., Echevin, V., Testor, P., Chaigneau, A., Mortier, L., Grados, C., and Albert, A.: Impact of a coastal-trapped wave on the near-coastal circulation of the Peru upwelling system from glider data, *Journal of Geophysical Research: Oceans*, 119, 2109–2120, 2014.
- Ramachandran, S., Tandon, A., and Mahadevan, A.: Enhancement in vertical fluxes at a front by mesoscale-submesoscale coupling, *Journal of Geophysical Research: Oceans*, 119, 8495–8511, doi:10.1002/2014JC010211, 2014.

- Resplandy, L., Lévy, M., D'Ovidio, F., and Merlivat, L.: Impact of submesoscale variability in estimating the air-sea CO₂ exchange: Results from a model study of the POMME experiment, *Global Biogeochemical Cycles*, 23, GB1017, doi:10.1029/2008GB003239, 2009.
- Rudnick, D. L.: On the skewness of vorticity in the upper ocean, *Geophysical Research Letters*, 28(10), 2045–2048, doi:10.1029/2000GL012265, 2001.
- 5 Shin, J., Dalziel, S., and Linden, P.: Gravity currents produced by lock exchange, *Journal of Fluid Mechanics*, 521, 1–34, 2004.
- Smith, S. D.: Coefficients for sea surface wind stress, heat flux, and wind profiles as a function of wind speed and temperature, *Journal of Geophysical Research: Oceans*, 93(C12), 15 467–15 472, doi:10.1029/JC093iC12p15467, 1988.
- Takahashi, T., Sutherland, S. C., Wanninkhof, R., Sweeney, C., Feely, R. A., Chipman, D. W., Hales, B., Friederich, G., Chavez, F., Sabine, C., Watson, A., Bakker, D. C., Schuster, U., Metzl, N., Yoshikawa-Inoue, H., Ishii, M., Midorikawa, T., Nojiri, Y., Körtzinger, A., Steinhoff, T., Hoppema, M., Olafsson, J., Arnarson, T. S., Tilbrook, B., Johannessen, T., Olsen, A., Bellerby, R., Wong, C., Delille, B., Bates, N., and de Baar, H. J.: Climatological mean and decadal change in surface ocean pCO₂, and net sea–air CO₂ flux over the global oceans, *Deep Sea Research Part II*, 56, 554 – 577, doi:10.1016/j.dsr2.2008.12.009, 2009.
- 10 Takahashi, T., Sutherland, S. C., Chipman, D. W., Goddard, J. G., Newberger, T., and Sweeney, C.: Climatological distributions of pH, pCO₂, total CO₂, alkalinity, and CaCO₃ saturation in the global surface ocean. ORNL/CDIAC-160, NDP-094., Carbon Dioxide Information Analysis Center, Oak Ridge National Laboratory, U.S. Department of Energy, Oak Ridge, Tennessee, doi:10.3334/CDIAC/OTG.NDP094, 2014.
- 15 Taylor, J. R. and Ferrari, R.: Ocean fronts trigger high latitude phytoplankton blooms, *Geophysical Research Letters*, 38, L23 601, doi:10.1029/2011GL049312, 2011.
- Thomas, L. N. and Lee, C. M.: Intensification of Ocean Fronts by Down-Front Winds, *Journal of Physical Oceanography*, 35, 1086–1102, doi:10.1175/JPO2737.1, 2005.
- 20 Thomas, L. N., Tandon, A., and Mahadevan, A.: Submesoscale Processes and Dynamics, in: *Ocean Modeling in an Eddy Regime*, edited by Hecht, M. W. and Hasumi, H., American Geophysical Union, Washington, D. C., doi:10.1029/177GM04, 2008.
- Thomsen, S., Eden, C., and Czeschel, L.: Stability Analysis of the Labrador Current, *Journal of Physical Oceanography*, 44, 445–463, doi:10.1175/JPO-D-13-0121.1, 2014.
- 25 Thomsen, S., Kanzow, T., Colas, F., Echevin, V., Krahnmann, G., and Engel, A.: Do submesoscale frontal processes ventilate the oxygen minimum zone off Peru?, *Geophysical Research Letters*, 43, 8133–8142, doi:10.1002/2016GL070548, 2016a.
- Thomsen, S., Kanzow, T., Krahnmann, G., Greatbatch, R. J., Dengler, M., and Lavik, G.: The formation of a subsurface anticyclonic eddy in the Peru-Chile Undercurrent and its impact on the near-coastal salinity, oxygen, and nutrient distributions, *Journal of Geophysical Research: Oceans*, 121, 476–501, doi:10.1002/2015JC010878, 2016b.
- 30 Ungarish, M. and Huppert, H. E.: On gravity currents propagating at the base of a stratified ambient, *Journal of Fluid Mechanics*, 458, 283–301, doi:10.1017/S0022112002007978, 2002.
- Walter, R. K., Stastna, M., Woodson, C. B., and Monismith, S. G.: Observations of nonlinear internal waves at a persistent coastal upwelling front, *Continental Shelf Research*, 117, 100–117, doi:10.1016/j.csr.2016.02.007, 2016.
- Wanninkhof, R.: Relationship between wind speed and gas exchange over the ocean, *Journal of Geophysical Research: Oceans*, 97, 7373–7382, doi:10.1029/92JC00188, 1992.
- 35 Wanninkhof, R.: Relationship between wind speed and gas exchange over the ocean revisited, *Limnology and Oceanography: Methods*, 12, 351–362, doi:10.4319/lom.2014.12.351, 2014.

- Weiss, R. F.: Carbon dioxide in water and seawater: the solubility of a non-ideal gas, *Marine Chemistry*, 2, 203–215, doi:10.1016/0304-4203(74)90015-2, 1974.
- Weiss, R. F. and Price, B. A.: Nitrous oxide solubility in water and seawater, *Marine Chemistry*, 8, 347–359, doi:10.1016/0304-4203(80)90024-9, 1980.
- 5 White, B. L. and Helfrich, K. R.: Rapid gravitational adjustment of horizontal shear flows, *Journal of Fluid Mechanics*, 721, 86–117, doi:10.1017/jfm.2013.41, 2013.

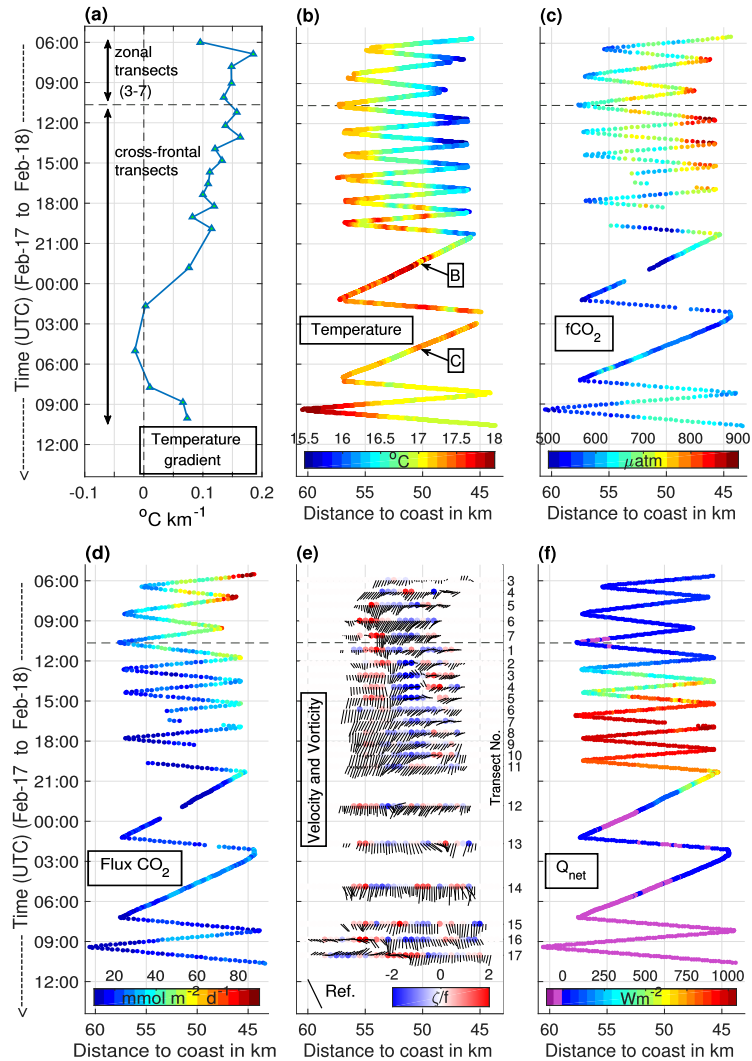


Figure 6. Hovmoeller diagrams of the cross-frontal surface temperature gradient (a), underway surface temperatures (b), surface $f\text{CO}_2$ (c), ocean-atmosphere CO_2 fluxes (d), mean current velocities in the upper 40 m (black lines) and vorticity (colored circles) (e) and diabatic surface heating (f) for the last five zonal transects and the subsequent 17 cross-frontal transects. The horizontal dashed line indicates the transition from zonal transects to repeated cross-frontal transects. Temperature gradients in (a) are calculated using a linear fit to the surface temperature transect shown in (b). In (b) the position of transects B and C is indicated. The vorticity of the vertically averaged velocity in (e) is calculated as $\zeta = \partial u_{al} / \partial y$ (Rudnick, 2001), where u_{al} is the along-front velocity and y is the cross-frontal distance, taken to be 2 km, comparable to the mixed layer deformation radius. The reference arrow in the bottom left corner anchored at 60 km from the coast indicates a flow with 0.3 m s^{-1} in the onshore (cross-front) and 0.3 m s^{-1} in the poleward along-front direction. The vorticity is normalized by the Coriolis parameter to give a proxy for the Rossby number. Velocity and vorticity are plotted at the time mean for each transect. Time is given in UTC.

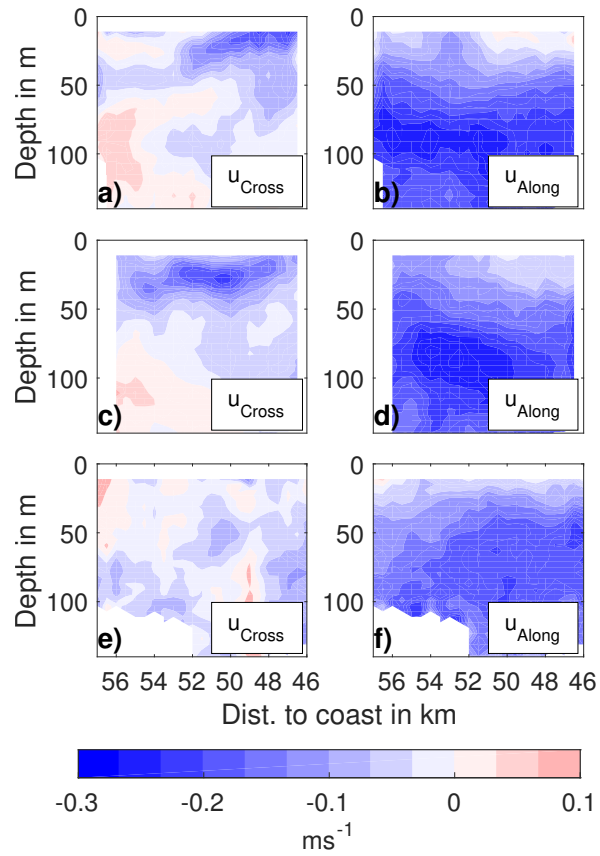


Figure 7. Mean cross- and along-front current velocities for cross-frontal transects 1-6 in (a) and (b), 7-11 in (c) and (d) and 12-17 in (e) and (f). Currents are horizontally binned onto a 500 m grid and subsequently averaged.

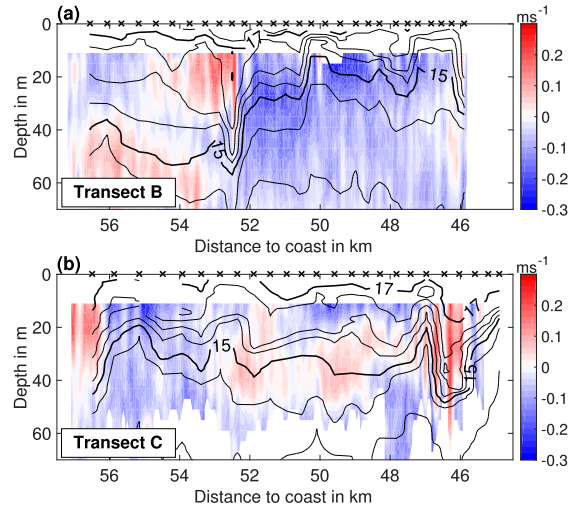


Figure 8. Temperature (black contour lines) and cross-front velocity (color-coded) for Transects B (a) and C (b) conducted as the 12th and 14th cross-frontal transect, starting on February 17 21:00 and February 18 03:00, respectively. Black crosses show the location of the temperature profiles from the microstructure probe. For both transects the ship moved away from the coast (right to left).

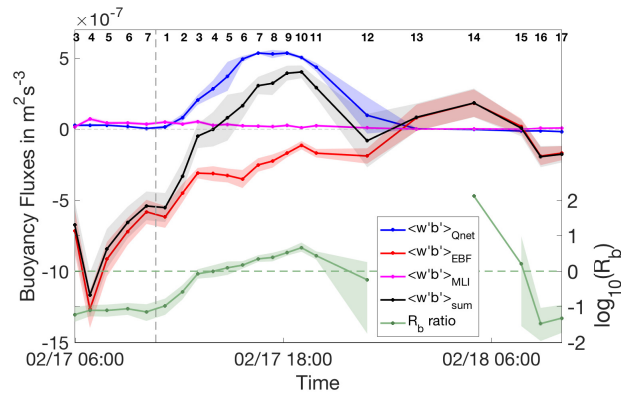


Figure 9. Vertical buoyancy fluxes associated with surface heating (blue), Ekman transport (red) and mixed layer instabilities (magenta). The shaded areas around the Ekman buoyancy flux (EBF) and the buoyancy flux associated with mixed layer instabilities (MLI) are accounting for uncertainties in the surface salinity gradient (see text for more details). The shaded uncertainty range for vertical buoyancy fluxes due to surface heating is given as one standard deviation obtained from sectional averaging. The sum of the three processes is given by the black line. The uncertainty is given as the maximum error resulting from the three processes. The R_b ratio (green) and its uncertainty are treated similarly. For cross-frontal transect 13 and 14 no R_b value or error can be stated due to the vanishing denominator in the definition of R_b . $\log_{10}(R_b) > 0$ points towards a net restratification, while $\log_{10}(R_b) < 0$ indicates a destabilization of the water column. For calculation details of all quantities see text. Time is given in UTC. The small black numbers on top indicate the respective zonal or cross-frontal transect number.

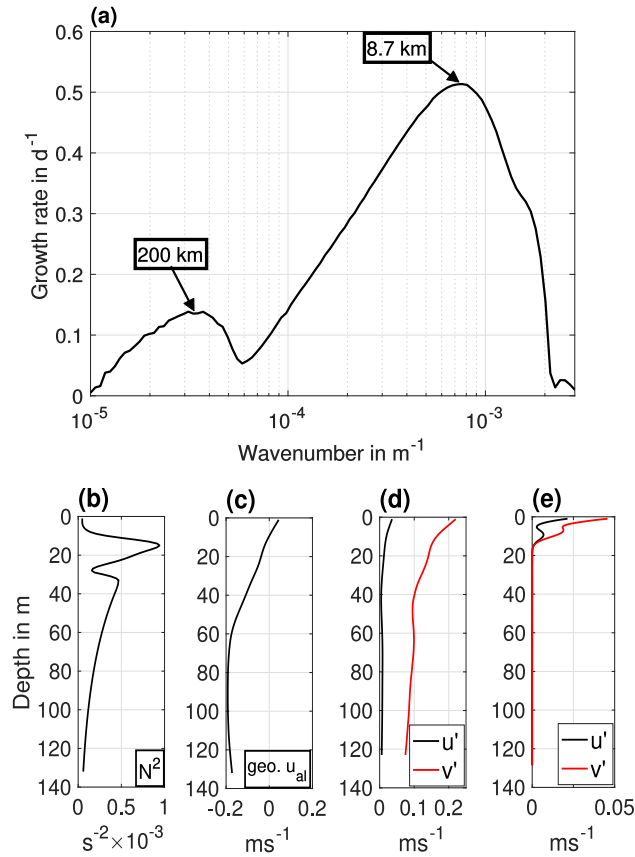


Figure 10. (a) Initial growth rate of baroclinic instabilities obtained from linear stability analysis, applied to the frontal state during the CTD section (transect A). The local maxima of the growth rate are labeled by their corresponding length scale in km. The smoothed stratification and geostrophic along-frontal velocity profiles used as the background state, are shown in panels (b) and (c). A deep mode at large horizontal scales (200 km) and a shallow mode, associated with mixed layer instabilities and short horizontal length scales (8.7 km) are present. The corresponding anomalies for the cross-front (u') and along-front (v') velocities are shown in panels (d) and (e) for the deep and shallow modes, respectively.

Submesoscale CO₂ variability across an upwelling front off Peru

Eike E. Köhn¹, Sören Thomsen¹, Damian L. Arévalo-Martínez¹, and Torsten Kanzow²

¹GEOMAR Helmholtz Centre for Ocean Research Kiel, Kiel, Germany

²Alfred-Wegener-Institute Helmholtz Centre for Polar and Marine Research, Bremerhaven, Germany

Correspondence to: Eike E. Köhn (ekoehn@geomar.de)

Abstract. While being a major source for atmospheric CO₂, the Peruvian upwelling region exhibits strong variability in surface $f\text{CO}_2$ on short spatial and temporal scales. Understanding the physical processes driving the strong variability is of fundamental importance for constraining the effect of marine emissions from upwelling regions on the global CO₂ budget. In this study, a frontal decay on length scales of $\mathcal{O}(10 \text{ km})$ was observed off the Peruvian coast following a pronounced decrease in downfrontal ([equatorward](#)) wind speed with a time lag of 9 hours. Simultaneously, the sea-to-air flux of CO₂ on the inshore (cold) side of the front dropped from up to 80 to 10 mmol m⁻² day⁻¹, while the offshore (warm) side of the front was constantly outgassing at a rate of 10-20 mmol m⁻² day⁻¹. Based on repeated ship transects the decay of the front was observed to occur in two phases. The first phase was characterized by a development of coherent surface temperature anomalies which gained in amplitude over 6-9 hours. The second phase was characterized by a disappearance of the surface temperature front within 6 hours. Submesoscale mixed layer instabilities were present but seem too slow to completely remove the temperature gradient in this short time period. Dynamics such as a pressure driven gravity current appear to be a likely mechanism behind the evolution of the front.

1 Introduction

Although the ocean generally acts as a net sink for atmospheric CO₂ (Takahashi et al., 2009), most low latitude eastern boundary upwelling systems (EBUS) are natural sources of CO₂ to the atmosphere (Chavez et al., 2007; Capone and Hutchins, 2013; Gruber, 2015). The distribution of CO₂ in such areas is complex and results from the interaction between cooling/warming at the surface, upwelling and mixing, biological activity, and riverine carbon and nutrient input (Laruelle et al., 2014; Gruber, 2015). As one of the four major EBUS, the Peruvian upwelling region is an important area for the exchange of climate relevant gases (e.g. CO₂, N₂O) between the ocean and the atmosphere (Friederich et al., 2008; Arévalo-Martínez et al., 2015). Hence, quantification of sea-to-air fluxes of CO₂ as well as their spatial and temporal variability [in the Peruvian upwelling region](#) is essential for constraining the global budget of CO₂ in a changing climate.

~~The High variability of~~ surface CO₂ in the Peruvian upwelling region is ~~highly-variable-observed~~ on short time $\mathcal{O}(\text{hours-days})$ and space $\mathcal{O}(\text{km})$ scales (~~Friederich et al., 2008~~), ~~due to driven by~~ both biological and physical processes ~~-(Friederich et al., 2008)~~. The sharp lateral temperature gradient, separating the newly upwelled, cold water from warm surface waters further offshore, allows for pronounced frontal processes, which manifest themselves in eddies and filaments (Penven et al., 2005; Chaigneau et al., 2008; McWilliams et al., 2009; Colas et al., 2012; Thomsen et al., 2016a). These submesoscale features, which go along

with Rossby numbers $Ro = \mathcal{O}(1)$, can develop strong vertical velocities in the upper ocean layer. Thus, surface fronts may enable the exchange of large amounts of heat and gas between the atmosphere and the subsurface ocean (Ferrari, 2011). However, ~~the small spatial and temporal scales involved make~~ submesoscale frontal processes are difficult to observe due to their small spatial and temporal scales. At the same time ~~model studies have put forward their importance~~ the importance of these dynamics for physical-biogeochemical coupling has been put forward by model studies, e.g. by ~~altering~~ altering the vertical transports of nutrients and organic carbon (Lapeyre and Klein, 2006; Lévy et al., 2012).

The link between the surface CO_2 distribution and the (sub-) mesoscale flow field was studied in the open ocean of the Northeast Atlantic by Merlivat et al. (2009), using both underway and lagrangian surface drifter measurements. During the measurement period, the study area was characterized by weak eddy kinetic energy. Still, submesoscale variability with large amplitude variations of surface CO_2 concentrations on horizontal length scales of $\mathcal{O}(10 \text{ km})$ was observed. This variability was successfully reproduced by the modelling study of Resplandy et al. (2009) but it does not seem to have a major effect on the model's overall CO_2 budget. The influence of submesoscale variability on the overall CO_2 budget might be stronger in the case of EBUS due to the ubiquitous existence of sharp fronts and filaments, i.e. in the case of a highly energetic (sub-) mesoscale flow field (McWilliams et al., 2009; Colas et al., 2012). However, so far no observations are available which describe the variability on the submesoscale off Peru.

In this study repeated measurements of CO_2 and physical properties across the upwelling front off Peru near 14° S are presented (see Fig. 1 for the large scale setting of the experiment). Throughout the two day experiment, we observed short-term fluctuations (timescales on $\mathcal{O}(\text{hours})$) of the surface temperature and velocity field. Simultaneously, surface CO_2 sea-to-air fluxes showed pronounced changes, implicating the importance of these timescales for the ocean-atmosphere gas exchange. The goal of this paper are to: 1) document the high-frequency variability across the upwelling front and 2) discuss possible physical driving mechanisms, improving our current understanding of the variability of surface CO_2 in the Peruvian upwelling region. ~~The field work was conducted during the RV Meteor cruise M93 in February/March 2013, and was carried out within the framework of the Research Collaborative Centre SFB754 (www.sfb754.de).~~

This paper is structured as follows: In section ~~2~~ 2-2 we present the ~~used experiment~~ the physical and biogeochemical datasets used for this study, as well as the methods employed for their analysis. Section 3 contains a description of ~~both the experiment and the~~ the initial state of the front. Observations from the ~~subsequent~~ following frontal evolution are presented in section 4. Subsequently, the changes ~~in~~ across the temperature front are analyzed in the context of various possible underlying dynamics, such as surface heating (Section 4.1), Ekman buoyancy fluxes (Section 4.2), submesoscale mixed layer instabilities (Section 4.3) or pressure driven gravity currents (Section 4.4). In section 5 these mechanisms are compared with respect to their associated buoyancy fluxes. Section 6 contains a discussion of the different mechanisms ~~and their likelihood in driving~~ which possibly drive the observed variability. The conclusions drawn from this study follow in section 7.

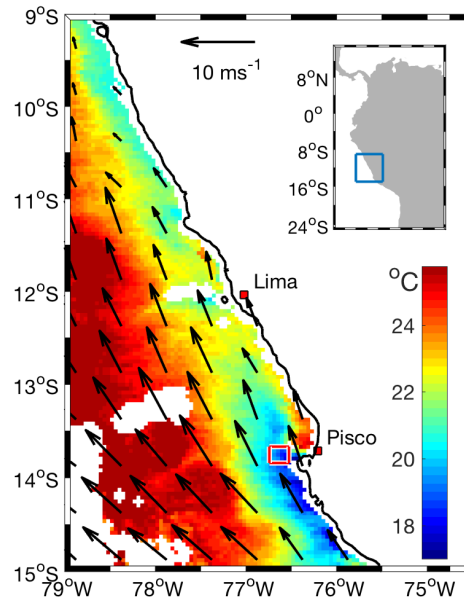


Figure 1. MODIS SST (color) and ASCAT (Advanced Scatterometer) wind field (arrows) off the Peruvian coast ~~of Peru~~ on February 16, 2013. The small red box shows the study region off ~~the coast of~~ Pisco.

2 Data and methods

2.1 Hydrographic and meteorological measurements

Near 14° S and 76°30' W the Peruvian upwelling region is characterized by a strong (quasi-) permanent upwelling cell (Fig. 1). The corresponding “upwelling front” was intensively sampled from February 16 to 18 during the RV *Meteor* cruise M93 in February/March 2013. The field work was carried out within the framework of the Collaborative Research Centre SFB754 “Climate-Biogeochemistry Interactions in the Tropical Ocean” (www.sfb754.de). The experiment’s procedure was as follows: Prior to the main experiment, a CTD section (transect “A”, black squares in Fig. 2) was conducted on February 16 from 10:00 to 15:00 (time always in UTC unless stated differently) to document the horizontal circulation and the initial vertical distribution of temperature, salinity, dissolved oxygen (O₂) and chlorophyll-a (Chl-*a*) across the front. Starting on February 17 at 04:00, the upwelling front was mapped by seven ~10 km long zonal transects. These were conducted from north to south in 1.8 km spacing (Fig. 2). Each zonal transect took about 45 minutes. From the highest and lowest surface temperature recorded, a cross-frontal axis was estimated. Subsequently, 17 cross-frontal transects were conducted along this axis to study the variability of the front on timescales of several hours. Among these, two high-resolution temperature sections “B” and “C” were conducted as cross-frontal transects 12 and 14. The high-resolution transects took 4.5 hours each to complete, while a

were measured at a height of ~~35.5~~35.3 m above the sea surface at a temporal resolution of 60 ~~seconds~~seconds. The surface wind stress was estimated from these measurements following Smith (1988). Underway ocean current velocity measurements with a vertical resolution of 4 m were obtained from a vessel-mounted 75 kHz ADCP (vmADCP). The shallowest vmADCP based current velocities were obtained in a bin centered at 11 m below the sea surface. The data was averaged in 1-minute-ensembles and smoothed using a 3-minute running mean. A 16.56° counterclockwise rotation is applied to transform the measured currents into along-front and cross-front velocities (note the frontal orientation in Fig. 2). As a result positive cross-front velocities are directed towards the coast and positive along-front velocities indicate an equatorward flow. Underway measurements of salinity are unavailable as the thermosalinograph's conductivity sensor failed to produce consistent results. Likewise, temperature and vmADCP measurements taken during periods of highly variable vessel speed and heading proved to be unreliable due to the influence of the ship. Thus, current measurements immediately before and after CTD stations are neglected in the following data analysis. During the analyzed transects the vessel speed was held at approximately constant 4 m s⁻¹ in order to achieve high quality ADCP data.

Hydrographic data *below* the surface were obtained from lowered conductivity, temperature and pressure (CTD) measurements. These are arranged in transect "A" consisting of four shallow CTD profiles located 7 km apart (black ~~dots~~squares in Fig. 2). The CTD was ~~also~~ equipped with a fluorometer and an oxygen sensor, allowing for ~~chlorophyll-*a* (Chl-*a*) and dissolved oxygen (and O₂)~~ measurements. A detailed description of the data processing, including the calibration of oxygen can be found in Thomsen et al. (2016b). As the Chl-*a* concentrations measured by the WET Labs (USA) fluorometer did not differ significantly from Chl-*a* concentrations determined from water samples (Meyer et al., 2017), no further calibration than the in-factory calibration was applied to the fluorometer data (see Loginova et al. (2016) for details). In order to obtain further subsurface hydrographic information, 53 temperature profiles organized in ~~two sections across the front~~ the two cross-frontal transects B and C with a horizontal resolution of 0.3 ~~0.5~~0.5 km were measured using the CTD sensors mounted on a microstructure profiler. During these measurements the speed of the vessel was reduced to about 0.75 m s⁻¹. ~~The two sections are thereafter referred to as transects "B" and "C".~~

Surface diabatic heating was calculated from underway measurements as $Q_{net} = Q_{lw} + Q_{sw} + Q_{sh} + Q_{lh}$, i.e. the sum of longwave and shortwave radiation as well as sensible and latent heat fluxes. Net shortwave radiation into the ocean was estimated using underway measurements of downward shortwave radiation under consideration of the surface albedo effect (Payne, 1972). Net longwave radiation into the ocean was calculated as the difference between the measured downward longwave radiation and outgoing longwave radiation estimated using Stefan-Boltzman's law (with an emissivity of 0.985) applied to the thermosalinograph's temperature measurements. Latent and sensible heat fluxes along the cruise track were calculated using bulk formulae including the Webb-correction to the latent heat flux (Fairall et al., 1996b). During the experiment an average flux of latent heat of 20 W m⁻² into the ocean was observed. This coincided with high relative humidity and partially foggy conditions. Neither a cool skin nor a warm skin correction is applied to the thermosalinograph's temperature measurements. A cool-skin would primarily form during night time, but is estimated to be on average less than 0.02 K cooler than the temperature measured by the thermosalinograph (Fairall et al., 1996a). A potentially larger warm-skin correction, which

would increase outgoing longwave radiation mainly during periods of strong insolation, is not applied. This error in heatflux is however small compared to the dominant heatflux related to shortwave radiation during daytime.

The large scale sea surface temperature (SST) was retrieved from NASA's OceanColor project as daily satellite MODIS Aqua und Terra SST data (<https://oceancolor.gsfc.nasa.gov/>). For the large scale wind field Advanced Scatterometer (ASCAT) wind data ([Bentamy and Fillon, 2012](#)) was taken from the Asia-Pacific Data-Research Center at the University of Hawai'i (<http://apdrc.soest.hawaii.edu/datadoc/ascat.php>). The spatial resolution of SST was 4 km, while the wind data was available on a 0.25° grid. ~~Nevertheless, it should be noted, that the~~ The ubiquitous presence of clouds during the main experiment period hindered an extensive use of remote sensing datasets.

2.2 Underway CO₂ measurements

CO₂ measurements were conducted by means of an underway system as described in Arévalo-Martínez et al. (2013). Seawater was drawn on board from a depth of about 6 m by means of a LOWARA submersible pump which was installed at the ship's moonpool. Atmospheric measurements were carried out every six hours by means of an AirCadet pump (Thermoscientific Inc., USA) which continuously brought air from 35 m height into the laboratory. Likewise, control measurements of standard gas mixtures with 201.0 and 602.4 ppm CO₂ were used in order to post-correct our data due to instrumental drift. The gas standards were prepared at Deuste Steininger GmbH (Mühlhausen, Germany) and were calibrated at the Max Planck Institute for Biogeochemistry (Jena, Germany) against the World Meteorological Organization standard scale. CO₂ data calibration as well as computation of CO₂ fugacities ($f\text{CO}_2$) was done according to the guidelines from Dickson et al. (2007). We report all seawater and atmospheric CO₂ values as 1-minute means. For this, we used a mean surface salinity from all CTD measurements of the M93 campaign (35.04), as salinity was not available from underway measurements. ~~The~~ A change in the mean salinity by 1 leads to a mean offset of 0.0055 μatm and has thus a small influence compared to temperature with an isochemical dependence of 15 μatm per °C (e.g. Körtzinger et al. (2000); Pierrot et al. (2009)). The uncertainty of the CO₂ measurements was hence about +/- 2 μatm . The air-sea flux of CO₂ was computed by using $F = kK_0(f\text{CO}_{2\text{sw}} - f\text{CO}_{2\text{air}})$, where k is the air-sea gas exchange coefficient, calculated using the parameterization of Nightingale et al. (2000) with wind speeds standardized to 10 m height (~~Garratt, 1977~~) (Smith, 1988). K_0 is the solubility of CO₂ in seawater, calculated with the equations and coefficients from Weiss (1974) and Weiss and Price (1980), and $f\text{CO}_{2\text{sw}}$ and $f\text{CO}_{2\text{air}}$ are the fugacities of CO₂ in seawater and atmosphere, respectively. The strongest correlation between the underway temperature and $f\text{CO}_2$ measurements was found at a time lag of 4 minutes ($r = -0.86$) (Fig. 3), which is probably due to the travel time for the seawater from the uptake to the underway CO₂ sensor. Thus CO₂ fugacities and fluxes are corrected for this time lag.

3 Physical and biogeochemical properties of the upwelling front

~~Near 14° S and 76°30' W the Peruvian upwelling region is characterized by a strong (quasi-) permanent upwelling cell (Fig. 1). The corresponding "upwelling front" was intensively sampled during the M93 cruise from February 16 to 18, 2013. The experiment's procedure was as follows: Prior to the main experiment (February 16 from 10:00 to 15:00), a CTD transect~~

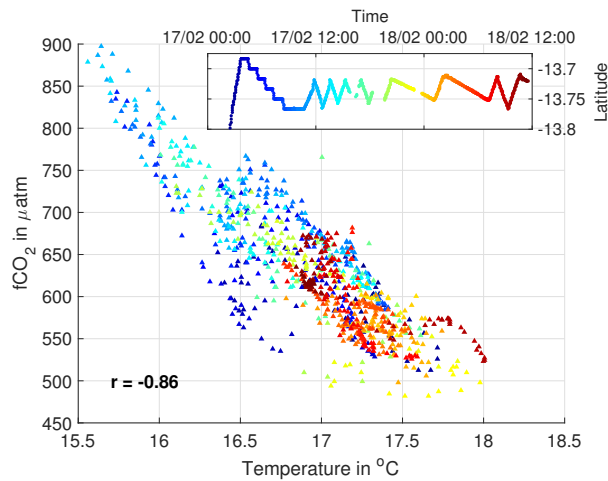


Figure 3. Correlation of surface temperature and $f\text{CO}_2$ during the main experiment. The $f\text{CO}_2$ values are **already**-corrected for a 4 minute time lag. The correlation value r is given in the bottom left corner. Data points are color-coded by their time of measurement. The top right box shows an orientation as to when the data was measured during the experiment. The color-coding carries the same information as the time axis.

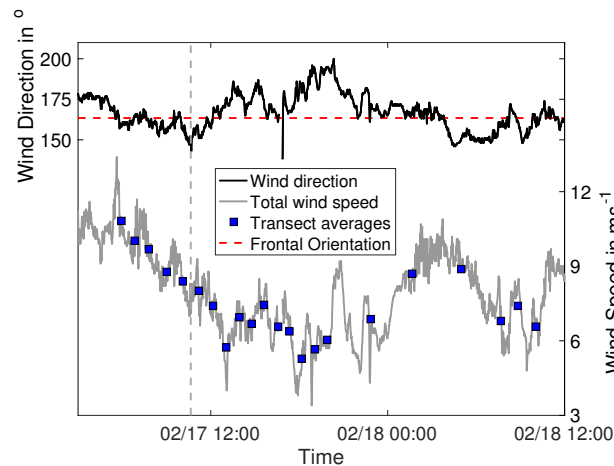


Figure 4. Time series of total wind speed (grey) and wind direction (black) from underway measurements at 35.3 m height. Blue rectangles show mean total wind speed for each zonal and cross-frontal transect. The dashed red line shows the (initial) frontal orientation deduced from the frontal mapping. The angle of 163.44° implicates the front running from south-south-east to north-north-west. The vertical dashed grey line indicates the transition from zonal to cross-frontal transects. Time is given in UTC.

(black-squares in Fig. 2) was conducted to document the horizontal circulation as well as the initial vertical distribution of temperature, salinity, O_2 and Chl- a across the front (Fig. 5). Starting on February 17 at 04:00, the upwelling front was mapped by seven ~ 10 long zonal transects. These were conducted from north to south in 1.8 spacing (Fig. 2). Each zonal transect

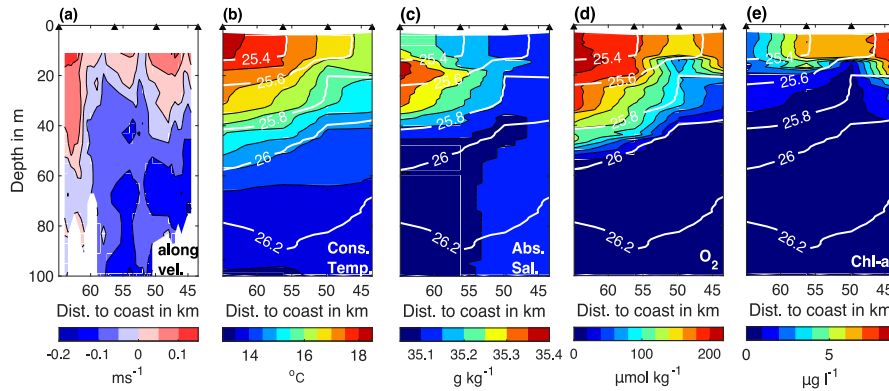


Figure 5. CTD Transect across the upwelling front before the main experiment conducted on February 16, 2013. Measured quantities contain along-frontal current velocities (a), conservative temperature (b), absolute salinity (c), O_2 (d) and Chl-*a* concentrations (e). Isopycnals are given by white lines in (b) - (e). Around CTD stations the along-frontal velocity is horizontally linearly interpolated.

took about 45 minutes. From the highest and lowest surface temperature recorded, a cross-frontal axis was estimated (dashed line in Fig. 2). Subsequently, 17 cross-frontal transects were conducted along this axis to study the variability of the front on timescales of several hours (Fig. 6). Among these, the high-resolution temperature sections B and C were conducted as cross-frontal transects 12 and 14. The high resolution transects took 4.5 hours each to complete, while a regular cross-frontal transect was completed in 40 minutes.

The experiment period can be divided into three different wind forcing regimes. The first regime is characterized by downfrontal (equatorward) winds with speeds of over above 10 m s^{-1} (Fig. 4). It lasts from the beginning of the experiment including the CTD transect (Fig. 5) until February 17 11:00, i.e. right after the beginning of the cross-frontal transects. During this phase, the front is characterized by a strong cross-frontal surface temperature gradient of about 1°C over 10 km (Fig. 6a). The CTD transect reveals the strong subsurface frontal signature in the temperature and salinity field (Fig. 5b,c). The mixed layer exhibits almost vertical isopycnals and is estimated to be about 15 m deep, using a $\Delta T = 0.2^\circ\text{C}$ criterion. The southward flowing Peru Chile Undercurrent (PCUC) weakens from $\sim 20 \text{ cm s}^{-1}$ at 80 meters depth towards the surface (Fig. 5a). The along-frontal velocity is low in the shallowest ADCP bin throughout the experiment (Fig. 7). As a result, lateral along-frontal advection is likely to play a minor role at the surface. In agreement with extensive upwelling of cold, nutrient rich waters during the strong wind period the Chl-*a* concentrations on the onshore side of the front were strongly enhanced with concentrations reaching $7 \mu\text{g l}^{-1}$ in the mixed layer (Fig. 5e). Simultaneously, the subsurface O_2 minimum was drawn closer to the surface on the onshore side of the front (Fig. 5d). Concentrations below $100 \mu\text{mol kg}^{-1}$ could be found at 15 m depth and values dropped below $20 \mu\text{mol kg}^{-1}$ already beneath $\sim 40 \text{ m}$. Further, a gradient in surface $f\text{CO}_2$ was discernible during the CTD transect (not shown) and during the zonal ship sections across the front (Fig. 2b), increasing from $600 \mu\text{atm}$ in offshore locations up to over $800 \mu\text{atm}$ on the onshore side of the front. During this period, peak sea-to-air CO_2 fluxes of over $80 \text{ mmol m}^{-2} \text{ d}^{-1}$ are measured on the cold side of the front (Fig. 6d).

~~Time series of total wind speed (grey) and wind direction (black) from underway measurements at 35.3 height. Blue rectangles shown mean total wind speed for each zonal and cross-frontal transect. The dashed red line shows the (initial) frontal orientation deduced from the frontal mapping. The vertical dashed grey line indicates the transition from zonal to cross-frontal transects. Time is given in UTC.~~

5 4 Cross-frontal changes after weakening of downfrontal winds

During the second wind period from 11:00 to 21:00 on February 17 the wind continues to blow in the downfrontal direction but drops to almost 5 m s^{-1} (Fig. 4). During this period the clear surface temperature gradient signal is disturbed by coherent anomalies appearing at 50 km off the coast (Fig. 6b). These anomalies grow in amplitude and lead to a break up of the clear temperature gradient at around 20:00. At the same time the strong outgassing of CO_2 is reduced on the onshore side of the front (Fig. 6d), while surface $f\text{CO}_2$ values remain rather high until about 18:00 (Fig. 6c). At the beginning of the transition to the low wind speed period, a strong offshore directed velocity signal is observed close to the surface on the onshore side of the front (Fig. 7a). The velocity maximum of up to 15 cm s^{-1} deepens with increasing distance from shore. During the wind minimum, maximum offshore velocities are found at 25-30 m depth, exceeding 20 cm s^{-1} (Fig. 7c). At the same time, the along-frontal velocity field exhibits a slight reduction in vertical shear (Fig. 7b,d).

At about 21:00 on February 17 the along-frontal (equatorward) wind begins to increase again and reaches about 9 m s^{-1} , defining the beginning of the third wind regime. Initially, the surface temperature gradient vanishes and even reverses slightly, before strengthening again towards February 18 09:00. Both high-resolution temperature transects (B and C) exhibit an average mixed layer depth of 3 and 5 m respectively (Fig. 8). The sections show that temperature changes are not limited to the surface layer but reach about 40-50 m deep. While the temperature field in transect B exhibits a clear frontal structure, the isotherms are close to horizontal in transect C, with exception of undulations associated with internal waves propagating onshore (e.g. at km 46 in Fig. 8b). As a result, the mean cross-frontal velocity field shows no longer any clear offshore directed velocity signal (Fig. 7e). Also the subsurface along-frontal (poleward) velocity maximum of the PCUC appears to be weaker (Fig. 7f). During this last phase the outgassing of CO_2 is at its minimum with fluxes less than $20 \text{ mmol m}^{-2} \text{ d}^{-1}$ despite the again increased wind speeds (Fig. 6d). $f\text{CO}_2$ remains at $\sim 600 \mu\text{atm}$ during this phase and increases only slightly along the last two transects during which the front starts to reform.

Figure 3 shows the correlation of surface temperature and $f\text{CO}_2$ during the main experiment. The high negative correlation indicates the governing effect of temperature on the CO_2 field. Especially during the beginning of the experiment the high $f\text{CO}_2$ values are only found on the cold side of the front. Towards the end of the experiment the clear correlation signal breaks up. The changes in temperature and $f\text{CO}_2$ are observed over the course of $\mathcal{O}(\text{hours})$, giving phytoplankton only a short time window to react. It is thus likely that physical processes are mainly responsible for the measured variability in surface $f\text{CO}_2$. In the following part of this study, we analyze the observed changes across the upwelling front in the context of physical processes that could be responsible for driving the observed $f\text{CO}_2$ variability.

4.1 Surface heat fluxes

The changes across the front are observed within a 24 hour period. The wind begins to drop at 11:00 on February 17 (06:00 ~~LT~~local time) and the temperature gradient fully vanishes 14 hours later at 01:00 on February 18 (Fig. 6a). As this time period matches well with the diurnal cycle of solar insolation, it could be hypothesized that differential heating throughout the day causes the reduction of the cross-frontal temperature gradient. Figure 6f shows the diurnal cycle of net surface heat flux. During the zonal transects the ocean surface is heated on average by 50 W m^{-2} . ~~In~~Due to the absence of solar insolation, this heatflux is mostly maintained by latent and sensible heat fluxes *into* the ocean, overcoming the ocean's weak heat loss ~~due to~~ caused by outgoing long wave radiation (individual heat flux components not shown). At around 12:00 (07:00 local time) the net heat flux into the ocean begins to strengthen, associated with an intensification of solar insolation. During the fourth and the beginning of the fifth cross-frontal transect the heat flux into the ocean is hampered due to irregularities in the incoming shortwave radiation. The net heat flux reaches its peak of 1010 W m^{-2} at 18:00 (13:00 local time) and reduces subsequently. From 23:00 (18:00 local time) onwards, the net heat flux fluctuates around 0 W m^{-2} . During the last cross-frontal transects the surface is continuously cooled by less than 50 W m^{-2} . During the phase of strongest heating, the heat flux shows only small lateral differences of mostly less than 50 W m^{-2} across the temperature front. Further, no clear pattern of slightly stronger heating on the cold side of the front is discernible. As a result, a uniform warming of the surface waters is expected. Sectional averaging of the first 13 cross-frontal transects, corresponding to the time period of incoming solar radiation, shows an increase of the transects' mean temperature of 0.8°C . From $\Delta Q = \rho_r c_p V \Delta T$ with the reference density $\rho_r = 1035 \text{ kg m}^{-3}$ and a heat capacity $c_p = 4000 \text{ J kg}^{-1} \text{ m}^{-3}$ it can be roughly estimated that over the same time period of 14.5 hours the average net heat flux causes a warming of a surface water column of volume V with unit area and 10 m depth by 0.6°C . Thus, the background temperature increase is most likely linked to the surface heat fluxes. The small scale temperature anomalies develop during the phase of strong heating (Fig. 6b). Using the same calculation as above the maximum heatflux of 1010 W m^{-2} can warm the surface water by almost 0.1°C per hour. Even though this roughly corresponds to the amplitude of the temperature anomalies, the lateral homogeneity of the net surface heat flux ~~makes it difficult~~ prohibits to attribute the development of the anomalies to surface heating.

The temperature front finally vanishes during a phase of almost no net surface heat flux. The high-resolution temperature transects B and C (Fig. 8) show, that during this phase, cooling takes place on the offshore side of the front, while the onshore side is significantly warmed over a period of 6 hours. On the onshore side, temperature changes of $\sim 2^\circ\text{C}$ occur up to ~ 40 m depth. A heatflux of $\sim 3800 \text{ W m}^{-2}$ is required to heat a water column of 40 m by 0.5°C using the rough estimate above. Likewise, a comparably strong cooling is required on the offshore side of the front in order to explain the observed temperature changes. Neither the two heatfluxes nor the associated strong cross-frontal gradient are within the range of the observed values.

The net surface heat flux can be converted into a vertical buoyancy flux following $\langle w'b' \rangle_{Q_{net}} = \alpha g Q_{net} / (\rho c_p)$, where w' is the vertical velocity anomaly, b' is the buoyancy anomaly, g is the gravitational acceleration and α is the thermal expansion coefficient. Due to the lack of data, the calculation of the surface density ρ requires an assumption about the salinity. The initial CTD section shows a surface salinity varying between ~~35.05~~ 35.1 and 35.2 (Fig. 5c). Thus, the surface water density ρ

is calculated using a constant salinity of 35.1, yielding an uncertainty of density in the range of 0.1 kg m^{-3} and in vertical buoyancy fluxes of 1%. The mean values of $\langle w'b' \rangle_{Q_{net}}$ for each transect are shown in Fig. 9. During both, night and day time, the surface layer gains buoyancy. In the night this vertical buoyancy flux is weak, with a rate of less than $1 \times 10^{-8} \text{ m}^2 \text{ s}^{-3}$. During the day, vertical buoyancy fluxes of more than $5 \times 10^{-7} \text{ m}^2 \text{ s}^{-3}$ act to stratify the surface layers.

5 While surface heat fluxes are shown to contribute to the overall evolution of the temperature field, ~~the observed heat fluxes do not yield the required strong gradients across the front and on even shorter length scales~~ they cannot explain the across-frontal variability. Especially, the observed temperature changes below the surface layer seem to be unconnected to surface heating. Thus, dynamical processes are investigated in the following to understand the reduction of the cross-frontal temperature gradient.

10 4.2 Ekman transport

Throughout the experiment the wind speed changed significantly from almost 12 m s^{-1} to 4 m s^{-1} , while the wind direction stayed almost parallel to the front in the same direction as the frontal jet, i.e. downfrontal (Fig. 4). The cross-frontal Ekman velocity is calculated as $u_{Ek} = \tau_0 / (f \rho_0 H_{ML})$, where $\tau_0 = \rho_{air} (c_d u_{10}^2)$ is the neutral along-frontal surface wind stress. The drag coefficient c_d and the along-frontal wind speed at 10 m height u_{10} are calculated following Smith (1988). The mean density within the Ekman layer ρ_0 is approximated by the surface density ρ . Assuming a mixed layer depth $H_{ML} = 10 \text{ m}$ Ekman current velocities reach up to 0.5 m s^{-1} and are always directed offshore (figure not shown). During the period of the developing surface temperature anomalies, the Ekman velocity drops to $\sim 0.1 \text{ m s}^{-1}$, agreeing with the observed cross-front velocities close to the surface (Fig. 7a,c). The large uncertainties in surface salinity lead to only minor errors in Ekman velocity of less than 10^{-3} m s^{-1} . The choice of the mixed layer depth has a far larger impact due to the inverse proportionality. For example choosing $H_{ML} = 5 \text{ m}$ leads to Ekman velocities larger by a factor of 2. The clear offshore direction of the Ekman transport is ~~however not put into question~~ not affected by these uncertainties.

The wind driven Ekman transport is associated with a non-geostrophic overturning circulation in the vertical/cross-frontal plane (Thomas et al., 2008). For such an overturning circulation it is possible to infer the associated vertical buoyancy flux $\langle w'b' \rangle$. The Ekman buoyancy flux (EBF) is given by $\langle w'b' \rangle_{EBF} = \tau_0 \cdot \nabla b / (\rho_0 f)$ (Thomas and Lee, 2005), where f is the Coriolis parameter. ∇b is the cross-frontal buoyancy gradient, taken as the slope from a linear fit to the surface buoyancy across the front. Buoyancy is calculated as $b = -g(\rho - \rho_r) / \rho_r$ using a reference density $\rho_r = 1035 \text{ kg m}^{-3}$.

Calculating the buoyancy gradient with a constant salinity value of 35.1 g kg^{-1} is likely to yield an error for the Ekman buoyancy fluxes as the initial CTD transect indicates a cross-frontal surface salinity gradient of $-5 \times 10^{-3} \text{ g kg}^{-1} \text{ km}^{-1}$. Hence, this salinity gradient is imposed onto the mean value of 35.1 g kg^{-1} to estimate the cross-frontal buoyancy gradient. Figure 9 shows the buoyancy fluxes calculated for each transect. The EBF is enclosed by an uncertainty range related to the surface salinity gradient. The edges of this uncertainty range stem from the case of no cross-frontal salinity gradient and of double the initially observed cross-frontal gradient.

The downfrontal wind drives a continuous Ekman transport from the cold to the warm side of the front, thus acting to keep the isopycnals strongly tilted, rather than directly transporting warm water onshore. Correspondingly, the EBF is predominantly

negative, signifying a destratification within the surface layer, inhibiting the slumping of isopycnals. During the cross-frontal transects, the EBF weakens drastically from $-1 \times 10^{-6} \text{ m}^2 \text{ s}^{-3}$ to $-2 \times 10^{-7} \text{ m}^2 \text{ s}^{-3}$. Only during cross-frontal transects 13-15 the buoyancy flux changes sign, which goes along with the turnaround of the surface temperature gradient (Fig. 6a) while the Ekman velocity continues to be directed offshore. Afterwards, during the reformation of the front towards the end of the experiment on February 18, the EBF returns to negative values.

The results above show, that the weakening of the temperature front is not directly caused by onshore Ekman transport. Still, the reduction in downfrontal (equatorward) wind speed and the associated weakening in offshore Ekman transport can change the frontal stability. During most of the experiment's duration, the EBF inhibited a slumping of isopycnals. However, this flux weakened over the course of the experiment, potentially allowing other processes such as surface heat fluxes or mixed layer instabilities to become more important.

4.3 Mixed layer instabilities (MLIs)

Baroclinic instabilities confined to the mixed layer are referred to as submesoscale mixed layer instabilities (MLI) (Haine and Marshall, 1998; Boccaletti et al., 2007). They act to restratify the mixed layer by extracting potential energy from horizontal density gradients within the vertically well mixed surface layer and convert this into eddy kinetic energy, by formation of mixed layer eddies which accomplish the cross-frontal transport and exchange. With their short timescales of $\mathcal{O}(f^{-1})$ submesoscale MLI are thought to be efficient in converting lateral density fronts to a stratified mixed layer. Their horizontal scales are given by $L = NH_{ML}/f$, where $N = \sqrt{g/\rho(\partial\rho/\partial z)}$ is the small but non-vanishing stratification within the mixed layer (Thomas et al., 2008). Based on the initial CTD transect A (shown in Fig. 5) this lengthscale L is calculated to be $2.5 \pm 1.5 \text{ km}$. The large error is accounting for the uncertainties in the mean mixed layer stratification, which is estimated to be $N \approx (6 \pm 4) \times 10^{-3} \text{ s}^{-1}$. The inverse of the growth rate of MLI ($2\pi/f$) can be used as the associated time-scale timescale which amounts to ~ 2.1 days in the present case. The proximity of the study region to the equator associated with relatively long inertial timescales, makes it possible to capture well the variability by means of underway measurements.

Repeated observations of coherent surface temperature anomalies and their intensification between 15:00 and 20:00 on February 17 around 50 kilometers away from the coast might indicate the development of MLI (Fig. 6b). Preceding their appearance are small anomalies in the current field averaged over the upper 40 m (Fig. 6e). There, the mostly southbound flow is reversing and weakly flowing northward, producing large relative vorticity values (cross-frontal transects 3, 4, 5). This points towards eddying structures which could be associated with MLI. The mixed layer depth, estimated by a $\Delta T = 0.2^\circ\text{C}$ criterion, shows a shallowing throughout the experiment. While the average mixed layer depth is 15 m during the CTD transect A it reduces to 3 and 5 m during transects B and C, respectively. We applied Linear Stability Analysis (LSA) linear stability analysis, which provides vertical modes of the growth of baroclinic instabilities (Brüggemann and Eden, 2014; Thomsen et al., 2014) to the laterally averaged stratification and geostrophic current shear profile from the initial CTD section (Fig. 10b,c). This analysis reveals the existence of both, a deep mesoscale mode and a shallow mode, confined to the mixed layer (Fig. 10a,d,e). The horizontal length scale of the deep mode is about 200 km, while it is only 8.7 km for the shallow mode. This length scale is of the same order of magnitude as the expected mixed layer deformation radius L and the size of the observed

surface temperature anomalies. The initial growth rate of the shallow mode calculated from [LSA-linear stability analysis](#) is 0.5 day^{-1} . Once the instabilities grow too large, nonlinearities dominate the instability process and [LSA-linear stability analysis](#) may not provide a useful description of the evolution of the instabilities (Thomsen et al., 2014). However, the calculated growth rate is relatively slow compared to the observed rapid decline of the cross-frontal temperature gradient. Also the [LSA-inferred](#) shallow mode is limited to $\sim 15 \text{ m}$ depth, i.e. the mixed layer (Fig. 10e). Thus, instability-induced changes of the velocity field at 30 m depth would require an interaction with the deep mode (Fig. 10d), ~~which according to LSA shows no large cross-front velocity anomalies.~~

Similar to Ekman dynamics, a secondary overturning circulation is driven by MLI. It is important to note, that while an EBF is associated with strong diapycnal mixing, pure mixed layer instabilities are of an adiabatic nature. According to Fox-Kemper et al. (2008) the vertical buoyancy flux due to MLI given by $\langle w'b' \rangle_{MLI} = CH_{ML}^2 (\nabla b)^2 / |f|$ (where $C = 0.08$ is a constant) always tends to reduce the lateral temperature gradient. Throughout the experiment the $\langle w'b' \rangle_{MLI}$ values are positive, indicating a restratification of the mixed layer. However, the buoyancy flux associated with MLI is in general about 10 times smaller than the EBF. During the stable front the buoyancy flux associated with MLI $\langle w'b' \rangle_{MLI}$ is less than $1 \times 10^{-7} \text{ m}^2 \text{ s}^{-3}$ and reduces afterwards. Calculations are done with $H_{ML} = 15 \text{ m}$ based on the CTD transect. This is likely to be an upper bound for the mixed layer depth during the main experiment, as transects B and C show a much shallower mixed layer. Both [LSA-linear stability analysis](#) and buoyancy flux estimates imply that MLI are present, acting to restratify the mixed layer, but seem to be too slow and too confined to the surface layer, such that observed changes at depth cannot be explained by MLI alone.

4.4 Surface gravity current

In the presence of lateral density gradients, an unforced surface mixed layer is subject to pressure driven gravity currents, where lighter water spreads on top of the denser waters on timescales below the inertial period, i.e. independent of rotational effects (e.g. Kao et al. (1977)). The observed ~~reduction-decrease~~ in downfrontal wind speed could therefore give rise to the spreading of a buoyant plume down the temperature gradient. The rapid decline and even a slight reversal of the temperature front is captured well by transects B and C (Fig. 8). Within 6 hours the structure of both the temperature and cross-frontal velocity fields changed significantly. While transect B still shows a pronounced (subsurface) frontal signature, the isotherms in transect C are close to being horizontal. The temperature field in transect C is subject to distortion through internal waves. At km 46, the undulating isotherms go along with an oscillating signal in cross-front velocity, agreeing with internal waves propagating up the continental shelf. The strong depression of isotherms at km 57 could be the onset of another internal wave signal. In transect B, the temperature and velocity field exhibit a strong anomaly at km 52.5. There, a narrow but strong depression of the temperature field coincides with a region of strong convergence in the cross-frontal direction. Unlike in transect C, the attribution of the depression of the isotherms to an internal wave signal is not straightforward as the velocity field does not show an oscillating behaviour in the vicinity of the depression. ~~However, this~~ [This](#) might be attributed to aliasing of the signal due to too few hydrographic observations, which do not capture the short period of the internal waves.

Any temperature-density (here temperature) front is associated with a cross-frontal pressure gradient. In coastal upwelling regimes, this pressure gradient is largely in geostrophic balance manifesting itself in an along-frontal jet. However, if the wind field setting up the frontal system becomes too weak, the tilted isopycnals might start to slump, with the light surface waters offshore pushing over the denser surface water located further onshore. Thus, baroclinic temperature fronts can be eroded by gravity currents flowing down the pressure gradient across the front. Observations from river plumes show that the head of a gravity current may excite large-amplitude internal waves (Nash and Moum, 2005). These are either arrested at the leading edge of the gravity current or may propagate ahead of it if the current's advection speed is lower than that of the wave propagation speed. Assuming that the anomaly signals in transect B (at km 52.5) and C (at km 46) belong to the same internal wave package that propagates at the leading edge of the gravity current, a propagation speed of 0.4 m s^{-1} is estimated using a time difference of 4.5 hours and a distance of 6.5 km. In a simple 2-layer model, the propagation speed of the gravity current in deep ambient fluid is given by $c = \sqrt{g'H}$, where $g' = g\Delta\rho/\rho$ is the reduced gravity, $\Delta\rho$ is the density difference between the two layers and H is the thickness of the upper layer (Shin et al., 2004; Dale et al., 2008). Assuming a 2-layer problem in the observed frontal setup with $H = 30 \text{ m}$, as the average depth of the 15°C isotherm, and $g' = 5 \times 10^{-3} \text{ m s}^{-2}$ derived from densities calculated at 10 and 50 m depth, assuming a salinity of 35, the theoretical propagation speed c can be estimated to be 0.4 m s^{-1} , thus agreeing with the observed propagation speed. If the temperature anomalies in sections B and C represent an internal wave package propagating at the leading edge of a gravity current, the internal wave propagation speed estimates above qualify a density driven gravity current as a possible mechanism behind the abrupt degradation of the temperature front. In contrast to the other analyzed processes it is capable of explaining subsurface changes in the temperature field.

5 Comparison of buoyancy fluxes

Over the whole experiment, three of the four analyzed physical processes are comparable in terms of the associated vertical buoyancy fluxes (Fig. 9). The ratio

$$R_b = \frac{\langle w'b' \rangle_{Q_{net}>0} + \langle w'b' \rangle_{MLI} + \langle w'b' \rangle_{EBF>0}}{\langle w'b' \rangle_{Q_{net}<0} + \langle w'b' \rangle_{EBF<0}} \quad (1)$$

allows for a statement on the combined effect of the Ekman buoyancy flux, surface heating and MLI (Mahadevan et al., 2010; Taylor and Ferrari, 2011). The numerator only contains terms associated with stratification, i.e. positive buoyancy fluxes. For example the buoyancy flux associated with MLIs is always positive and thus appears only in the numerator. The EBF however changes sign during the experiment. During the parts of the experiment with positive EBF it will contribute to the term $\langle w'b' \rangle_{EBF>0}$ in the numerator. If the EBF is negative, its modulus will appear in the denominator as $\langle w'b' \rangle_{EBF<0}$. The same applies to the surface heating buoyancy fluxes. As a result, if $R_b > 1$, the mixed layer is subject to restratification associated with a slumping of isopycnals, whereas $R_b < 1$ implies a destratification, i.e. mixing in the surface layer. During the time of the development of the coherent surface temperature anomalies (cross-frontal transects 7-11), the combination of the three processes favor a restratification of the mixed layer (Fig. 9). Linear stability analysis confirms the existence of a shallow baroclinic mode, which shows growth rates of 0.5 d^{-1} on lengthscales of 8.7 km. The latter agrees well with the extent of the

observed temperature anomalies and the mixed layer radius of deformation calculated from the initial CTD transect. While the temporal scale of the shallow mode is in agreement with the development of the surface temperature anomalies, its impact in the rapid decline of the temperature front around 00:00 on February 18 is probably low, as the growth rate at the initial phase of the instability seems too small. Further, the low associated buoyancy fluxes (Fig. 9) indicate that MLI may contribute only to a small degree to the observed ~~variability~~ change in the temperature gradient across the front.

In contrast, the buoyancy fluxes associated with surface heating and cross-frontal Ekman transport (Fig. 9) contribute to the changes in sign of the sum of the buoyancy flux (and to $R_b > 1$) during February 17. Even though the strength of the diabatic heating agrees well with the amplitude of the developing surface temperature anomaly, stronger than observed horizontal gradients in surface heating are required to induce the observed lateral differences in warming. Further, the nature of this buoyancy flux is purely vertical and thus unable to create horizontal gradients in the case of spatially uniform heating, opposed to buoyancy fluxes associated with MLI or Ekman dynamics, which are fully 3-dimensional.

The buoyancy flux related to a gravity current is mainly lateral. However, if the warm water spreads on top of the cold water on the onshore side of the front, a vertical buoyancy flux is induced. In a closed domain the mean vertical buoyancy flux can be estimated following $\partial E_p / \partial t \approx -\langle wb \rangle$ (Peltier and Caulfield, 2003; White and Helfrich, 2013), thus by comparing volume-averaged potential energies E_p at two different points in time t . In a 2-dimensional domain the volume-averaged potential energy is calculated as $E_p = (hd)^{-1} \int_d \int_0^h b z dz dx$, where d is the lateral distance and h is depth. Using a constant salinity value of 35 the buoyancy field is calculated for transects B and C. Considering the upper 70 m on the initially cold side of the front (i.e. only east of 52 km offshore) a vertical buoyancy flux of $2.7 \times 10^{-6} \text{ m}^2 \text{ s}^{-3}$ is estimated. Laterally extending the domain to the full transects B and C reduces the vertical buoyancy flux to $1.8 \times 10^{-6} \text{ m}^2 \text{ s}^{-3}$. As the transects B and C have no closed boundaries, the estimates carry large uncertainties. The pressure driven gravity current is however assumed to be fully captured by both transects so that its associated effect should be captured. In the context of a closed domain the subsurface temperature reduction on the initially warm side of the front could be associated with an upward suction of colder water balancing the downward pumping of surface water on the cold side of the front (Fig. 8).

The estimated flux due to the gravity current is much larger than the buoyancy fluxes associated with the other ~~above~~ analyzed processes ~~processes described above~~ during the cross-frontal transects 12-14, regardless of the chosen cross-frontal width considered. Only the EBF during the beginning of the experiment is of the same order of magnitude.

6 Discussion

Gathering data from multiple ship surveys Friederich et al. (2008) observed oceanic outgassing of CO_2 in the Peruvian upwelling region throughout the year. On average the authors estimated a sea-to-air CO_2 flux of $5 \text{ mol m}^{-2} \text{ yr}^{-1}$. On seasonal timescales, the flux varied between 2.5 and $10 \text{ mol m}^{-2} \text{ yr}^{-1}$ associated with weak and strong upwelling periods, respectively. Although Friederich et al. (2008) focused on the large scale distribution of surface CO_2 fluxes and the associated mechanisms, they further detected strong variability of CO_2 fluxes on short time and space scales ($\mathcal{O}(\text{hours-days})$ and $\mathcal{O}(\text{km})$), which contributes significantly to the overall CO_2 budget.

Motivated by their findings, the study presented here focuses on the pronounced submesoscale variability of surface CO₂ in the Peruvian upwelling region at 13.7° S. Our observations show CO₂ outgassing rates between 3.5 and 30 mol m⁻² yr⁻¹ which are in line with the outgassing signals observed by Friederich et al. (2008), even after accounting for the difference in converting our values from partial pressures to fugacities (difference usually about 3%). Our peak sea-air fluxes reaching up to 80 mmol m⁻² d⁻¹ are distinctly higher than the maximum flux of 12.4 mmol m⁻² d⁻¹ reported by Friederich et al. (2008) for a measurement campaign in the month of February. At the same time, our peak-flux is only slightly higher than maximum flux values reported from other months. ~~It should be pointed out, however, that the~~ The results from Friederich et al. (2008) ~~are~~ were re-scaled to a much larger area (5° S - 15° S), have been subject of spatial extrapolation and smoothing, and were calculated with ~~a~~ the sea-air gas exchange parameterization by Wanninkhof (1992) which tends to overestimate the gas transfer velocities (see Wanninkhof (2014)). ~~Hence,~~ Simply using the Wanninkhof (1992) parameterization instead of the Nightingale et al. (2000) parameterization yields 17% higher fluxes, already indicating that it is difficult to draw a direct comparison between both data sets. Nonetheless, both studies agree in that the near-coastal zone off Peru acts as a rather strong source of CO₂ to the atmosphere, and from our data it seems clear that the onshore side of the upwelling front could be associated with an important enhancement of CO₂ outgassing. ~~We analyzed~~ The conditions observed in this study are not necessarily representative for February conditions. Many processes on different timescales can alter the upwelling frontal structure and intensity off Peru, for instance the state of the El Niño Southern Oscillation (Espinoza-Morriberón et al., 2017) or coastally trapped waves propagating along the Peruvian coast (Pietri et al., 2014). The aim of this study is rather to analyze a suite of processes involved in the evolution of the upwelling front and surface fCO₂ on short ~~time and space scales~~ space and timescales (O(1)km), O(0.5)day). The following conclusions can be drawn from the results: day).

The downfrontal wind is an important ingredient in maintaining tilted isopycnals in the surface layer. The EBF dominates all other buoyancy fluxes during the strong wind period (Fig. 9). In ~~the~~ a study by Dale et al. (2008) a restratification of the mixed layer is observed in connection with a frontal decay in the upwelling system off Oregon on length scales comparable to those presented here. In their study, a reversal of the wind direction plays a crucial role in driving the frontal decay by inducing an Ekman transport down the cross-frontal pressure gradient. For the frontal decay presented here, the wind is always directed ~~down-frontal~~ downfrontal and does not change significantly. The cross-frontal wind component is weak (mostly less than 3 m s⁻¹) and alternates in direction between onshore and offshore without any clear dominance (Fig. 4). As a result, Ekman transport and the associated buoyancy flux do not change direction. Still, the strong reduction in cross-frontal Ekman transport could potentially give way for other mechanisms.

Pronounced changes across the front are shown to occur in two steps after the distinct reduction in downfrontal wind speed with a time lag of about 9 hours. The first step is characterized by the gradual development and strengthening of coherent surface temperature anomalies, while the second is characterized by a sudden decline and even slight reversal of the temperature gradient. Transects B and C (Fig. 8) show that changes in the temperature field are thereby not limited to the surface layer, but reach down to 50 m. To identify the underlying processes, the frontal evolution is described above in a 2-dimensional framework, i.e. in the vertical/cross-frontal plane. The variability induced by along-frontal advection is neglected. This assumption seems valid, as the along-frontal current velocities reduce close to zero in proximity to the surface (Fig. 7b,d,e). Further, the fact

that the cross-frontal transects show coherent signals, even though not all cross-frontal transects were performed on the exact same track, but about 1 km apart, points towards a weak along-frontal flow variability. Still, the two dimensional framework allows for various hypotheses about the driving mechanisms behind the observed changes.

The analyses have shown that the diurnal surface heating is able to explain the majority of the mean increase in surface temperatures. During the phase of maximum heating the associated positive buoyancy flux into the ocean outweighs the permanent reduction in surface buoyancy by the ~~down-frontal~~ downfrontal wind stress (Fig. 9). However, the spatially homogeneous heating is unable to account for the developing small-scale temperatures anomalies. As a result, submesoscale MLI have been investigated as they are shown to restratify the surface mixed layer and are thereby capable of generating lateral gradients and anomalies. LSA-Linear stability analysis indeed shows the presence of a shallow baroclinic mode confined to the mixed layer (Fig. 10). While the length scale of this mode roughly meets the observed horizontal extent of the temperature anomalies and the mixed layer deformation radius, the instability seems to grow too slowly to be the dominant dynamical process involved in the frontal decay. Hence, also the vertical buoyancy fluxes associated with MLI are an order of magnitude smaller than those related to surface heating or Ekman dynamics (Fig. 9).

The low-latitude location of the experiment site at 13.77° S results in a rather long inertial time period of $T_{in} = 2\pi/f = 2.1$ days. Thus, the sudden changes observed from hydrographic sections B and C within a time span of 6 hours suggest that processes influenced by Earth's rotation, are potentially less important in the final weakening of the temperature front. Propagating buoyant plumes related to river discharge (Nash and Moum, 2005) or frontal zones in upwelling regimes (Walter et al., 2016) are common dynamical processes in continental shelf regions. In fact, Dale et al. (2008) also identified such a pressure-driven gravity current propagating across the front, once the wind forcing had changed. For our case, using the limited amount of hydrographic information, a propagation speed of 0.4 m s^{-1} can be identified. This proves to match well with the theoretical estimate for a 2-layer system. The present stratification however complicates the distinction of a sharp density gradient to apply the gravity current theory. Further, stratified ambient water decreases the propagation speed of a gravity current compared to the two layer system (Ungarish and Huppert, 2002). Still, hinting towards the observation of a gravity current, both transect B and C exhibit strong internal wave signals, which have been observed at the leading edge of such buoyant plumes (Nash and Moum (2005); Bourgault et al. (2016)). Of all mechanisms presented, the gravity current is the only one that may account for the fast changes up to 50 m depth. In contrast, the stability analysis suggests, that MLI are mainly active in the mixed layer and could only effect lower layers by interacting with the deep mode (Ramachandran et al., 2014; Capet et al., 2016).

In this study we set focus solely on the role of physical processes driving the small-scale distribution of $f\text{CO}_2$. We argue that the timescales considered here are too short to allow for significant contributions of biological processes in driving $f\text{CO}_2$ changes across the front. The strong correlation of surface temperature and $f\text{CO}_2$ imply that the $f\text{CO}_2$ variability is dominated by two processes: Firstly, the temperature dependent solubility of gases in seawater and secondly, warm offshore surface water pushing on top of CO_2 -enriched upwelled water, thus creating a mechanical barrier for air-sea gas exchange. However, the weakening of the correlation over time (Fig. 3) indicates that other processes, such as biological activity, might become increasingly important. A more thorough analysis from a biogeochemical perspective is needed, incorporating these effects

(Mahadevan et al., 2004). Consistently, physical processes seem to be able to account for the small scale variability observed by Friederich et al. (2008) and understanding them could be crucial to establish a reliable CO₂ budget for the Peruvian upwelling region. Likewise, it is mandatory to have accurate observations of the near-shore wind field, as it proved to be an important factor that contributes to the small-scale evolution of the upwelling front. Modern satellite wind products are still too coarse to
5 resolve the submesoscale frontal variability or other small scale variations such as land-sea breezes or an enhanced near-shore wind stress curl and They are thus not fully reliable within 25 to 50 km from shore (Croquette et al., 2007; Albert et al., 2010).

7 Conclusions

High-resolution, underway measurements are ~~demonstrated to be~~ a useful tool in observing ~~the~~ submesoscale variability on scales of $\mathcal{O}(1)$ km. Pronounced changes in the $f\text{CO}_2$ and temperature fields were observed across an upwelling front within
10 hours, providing evidence of high short-term variability in the sea-air CO₂ exchange off Peru. We provide evidence of the complex submesoscale distribution of surface CO₂ in the Peruvian upwelling system and its tight connection to the strong variability in surface temperature. It thus appears that on these timescales the evolving $f\text{CO}_2$ distribution is controlled by physical processes.

Outgassing of CO₂ dropped from 80 mmol m⁻² d⁻¹ to less than 10 mmol m⁻² d⁻¹ within less than 24 hours. We showed
15 that this drastic change can be explained by physical processes associated with a weakening of the cross-frontal temperature gradient following a significant decrease in downfrontal (equatorward) windspeed. The initially geostrophically balanced front with a length scale of 10 km vanished within few hours, thereby removing a surface temperature difference of 1°C over 10 km. Hydrographic data shows pronounced changes in the temperature field at depths of up to 50 m. Despite the lack of direct onshore transport of warm water by Ekman dynamics, the wind played a major role in maintaining the front in the beginning
20 of the experiment. The decay of the ~~down-frontal~~ downfrontal wind gave rise to the development of submesoscale mixed layer instabilities and potentially allowed for a gravity current to propagate down the cross-frontal pressure gradient. The mixed layer instabilities, however, appear to be too shallow and too slow to be able to account for the complete removal of the cross-frontal temperature gradient. Yet, the onset of a surface gravity current would be consistent with the observed changes in the subinertial period. In addition, our analysis shows that multiple processes act simultaneously and are likely to interact, thus
25 complicating the identification of a single, dominant mechanism responsible for ~~fast the~~ the fast observed changes in surface $f\text{CO}_2$.

At present, a low CO₂ data coverage within the Peruvian upwelling region (e.g. in SOCAT, Bakker et al. (2016)) complicates the establishment of a reliable climatology, as done by Takahashi et al. (2014) or more recently Landschützer et al. (2017). From our study the importance of the wind and temperature variability on timescales of $\mathcal{O}(\text{hours})$ in setting the strength of
30 sea-air CO₂ fluxes becomes obvious. When coupled with CO₂ measurements the use of sea surface temperature and wind products, which capture the high temporal and spatial variability, could lead to improved future estimates of a CO₂ flux climatology off Peru. In order to understand the large scale impact of short-term variability of an upwelling ecosystem, a way forward would be the establishment of multi-platform observation networks in which continuous in situ data is complemented

by satellite observations and measurements from autonomous platforms such as e.g. gliders, as for example conducted by Ohman et al. (2013) in the California Current System. A further example are the moored CO₂ observations from Lefèvre et al. (2008) and Lefèvre and Merlivat (2012) which help to constrain regional budgets and variability of CO₂ for the Eastern Tropical Atlantic and could also be used to reliably estimate the net carbon community production in this area.

5 8 Data availability

~~The used data sets are stored in the Kiel Ocean Science Information System (OSIS, https://portal.geomar.de/kdmi_datamanagement@geomar.de) and can be accessed upon request.~~ According to the SFB 754 data policy (<https://www.sfb754.de/de/data>), all data associated with this publication ~~will be published at a world data center (www.ioda.info)~~ are accessible upon publication under [https://doi.pangaea.de; search-projects:sfb754](https://doi.pangaea.de/search-projects:sfb754) when the paper is accepted and published/10.1594/PANGAEA.881049.

- 10 *Author contributions.* E. E. Köhn performed the analysis and wrote the manuscript. S. Thomsen designed the experiment and contributed to the manuscript. D. L. Arévalo-Martínez measured and provided the CO₂ data and contributed to the manuscript. T. Kanzow was chief scientist on M93, stimulated the analysis and gave scientific guidance. All authors reviewed and commented on the manuscript.

Competing interests. The authors declare that they have no conflict of interest.

- Acknowledgements.* This work is a contribution of the Sonderforschungsbereich 754 "Climate-Biogeochemistry Interactions in the Tropical Ocean" (www.sfb754.de), which is funded by the Deutsche Forschungsgemeinschaft (DFG). We are grateful to the Peruvian authorities for the permission to carry out scientific work in their national waters. Special thanks go to the captain and the crew of the R/V *Meteor* for their support during the M93 cruise. We are grateful to T. Steinhoff for making available the CO₂ sensor as well for ~~its~~his technical support during the cruise. We further thank Liam Brannigan ~~and Leah Johnson~~, Leah Johnson, Karl Bumke and the meteorologists of the DWD for helpful discussions of the results. D. L. Arévalo-Martínez received additional funding support through the BMBF funded SOPRAN II (FKZ 20 03F0611A) project, as well as the Future Ocean Excellence Cluster at Kiel University (CP0910), and the EU FP7 project InGOS (grant agreement 284274).

References

- Albert, A., Echevin, V., Lévy, M., and Aumont, O.: Impact of nearshore wind stress curl on coastal circulation and primary productivity in the Peru upwelling system, *Journal of Geophysical Research: Oceans*, 115, C12 033, doi:10.1029/2010JC006569, 2010.
- Arévalo-Martínez, D. L., Beyer, M., Krumbholz, M., Piller, I., Kock, A., Steinhoff, T., Körtzinger, A., and Bange, H. W.: A new method for continuous measurements of oceanic and atmospheric N₂O, CO and CO₂: performance of off-axis integrated cavity output spectroscopy (OA-ICOS) coupled to non-dispersive infrared detection (NDIR), *Ocean Science*, 9, 1071–1087, doi:10.5194/os-9-1071-2013, 2013.
- Arévalo-Martínez, D. L., Kock, A., Löscher, C. R., Schmitz, R. A., and Bange, H. W.: Massive nitrous oxide emissions from the tropical South Pacific Ocean, *Nature Geoscience*, 8, 530–533, doi:10.1038/ngeo2469, 2015.
- Bakker, D. C. E., Pfeil, B., Landa, C. S., Metzl, N., O'Brien, K. M., Olsen, A., Smith, K., Cosca, C., Harasawa, S., Jones, S. D., Nakaoka, S.-I., Nojiri, Y., Schuster, U., Steinhoff, T., Sweeney, C., Takahashi, T., Tilbrook, B., Wada, C., Wanninkhof, R., Alin, S. R., Balestrini, C. F., Barbero, L., Bates, N. R., Bianchi, A. A., Bonou, F., Boutin, J., Bozec, Y., Burger, E. F., Cai, W.-J., Castle, R. D., Chen, L., Chierici, M., Currie, K., Evans, W., Featherstone, C., Feely, R. A., Fransson, A., Goyet, C., Greenwood, N., Gregor, L., Hankin, S., Hardman-Mountford, N. J., Harlay, J., Hauck, J., Hoppema, M., Humphreys, M. P., Hunt, C. W., Huss, B., Ibáñez, J. S. P., Johannessen, T., Keeling, R., Kitidis, V., Körtzinger, A., Kozyr, A., Krasakopoulou, E., Kuwata, A., Landschützer, P., Lauvset, S. K., Lefèvre, N., Lo Monaco, C., Manke, A., Mathis, J. T., Merlivat, L., Millero, F. J., Monteiro, P. M. S., Munro, D. R., Murata, A., Newberger, T., Omar, A. M., Ono, T., Paterson, K., Pearce, D., Pierrot, D., Robbins, L. L., Saito, S., Salisbury, J., Schlitzer, R., Schneider, B., Schweitzer, R., Sieger, R., Skjelvan, I., Sullivan, K. F., Sutherland, S. C., Sutton, A. J., Tadokoro, K., Telszewski, M., Tuma, M., van Heuven, S. M. A. C., Vandemark, D., Ward, B., Watson, A. J., and Xu, S.: A multi-decade record of high-quality *f*CO₂ data in version 3 of the Surface Ocean CO₂ Atlas (SOCAT), *Earth System Science Data*, 8, 383–413, 2016.
- Bentamy, A. and Fillon, D. C.: Gridded surface wind fields from Metop/ASCAT measurements, *International Journal of Remote Sensing*, 33, 1729–1754, doi:10.1080/01431161.2011.600348, 2012.
- Boccaletti, G., Ferrari, R., and Fox-Kemper, B.: Mixed Layer Instabilities and Restratification, *Journal of Physical Oceanography*, 37, 2228–2250, doi:10.1175/JPO3101.1, 2007.
- Bourgault, D., Galbraith, P. S., and Chavanne, C. P.: Generation of internal solitary waves by frontally forced intrusions in geophysical flows, *Nature Communications*, 7, 13 606, doi:10.1038/ncomms13606, 2016.
- Brüggemann, N. and Eden, C.: Evaluating Different Parameterizations for Mixed Layer Eddy Fluxes induced by Baroclinic Instability, *Journal of Physical Oceanography*, 44, 2524–2546, doi:10.1175/JPO-D-13-0235.1, 2014.
- Capet, X., Roullet, G., Klein, P., and Maze, G.: Intensification of Upper-Ocean Submesoscale Turbulence through Charney Baroclinic Instability, *Journal of Physical Oceanography*, 46, 3365–3384, doi:10.1175/JPO-D-16-0050.1, 2016.
- Capone, D. G. and Hutchins, D. A.: Microbial biogeochemistry of coastal upwelling regimes in a changing ocean, *Nature Geoscience*, 6, 711–717, doi:10.1038/ngeo1916, 2013.
- Chaigneau, A., Gizolme, A., and Grados, C.: Mesoscale eddies off Peru in altimeter records: Identification algorithms and eddy spatio-temporal patterns, *Progress in Oceanography*, 79, 106–119, doi:10.1016/j.pocean.2008.10.013, 2008.
- Chavez, F. P., Takahashi, T., Cai, W.-J., Friederich, G., Hales, B., Wanninkhof, R., and Feely, R.: Coastal oceans, in: *The First State of the Carbon Cycle Report (SOCCR): The North American Carbon Budget and Implications for the Global Carbon Cycle*, edited by King, A. W., Dilling, L., Zimmerman, G. P., Fairman, D. M., Houghton, R. A., Marland, G., Rose, A. Z., and Wilbanks, T. J., A report by the U.S. Climate Change Science Program and the Subcommittee on Global Change Research, Washington, DC, 2007.

- Colas, F., McWilliams, J. C., Capet, X., and Kurian, J.: Heat balance and eddies in the Peru-Chile current system, *Climate Dynamics*, 39, 509–529, doi:10.1007/s00382-011-1170-6, 2012.
- Croquette, M., Eldin, G., Grados, C., and Tamayo, M.: On differences in satellite wind products and their effects in estimating coastal upwelling processes in the south-east Pacific, *Geophysical Research Letters*, 34, L11 608, doi:10.1029/2006GL027538, 2007.
- 5 Dale, A. C., Barth, J. A., Levine, M. D., and Austin, J. A.: Observations of mixed layer restratification by onshore surface transport following wind reversal in a coastal upwelling region, *Journal of Geophysical Research: Oceans*, 113, C01 010, doi:10.1029/2007JC004128, 2008.
- Dickson, A. G., Sabine, C. L., and Christian, J. R., eds.: Guide to best practices for ocean CO₂ measurements. PICES Special Publication 3, 191 pp., 2007.
- Espinoza-Morriberón, D., Echevin, V., Colas, F., Tam, J., Ledesma, J., Vásquez, L., and Graco, M.: Impacts of El Niño events on the Peruvian upwelling system productivity, *Journal of Geophysical Research: Oceans*, 122, 5423–5444, doi:10.1002/2016JC012439, 2017.
- 10 Fairall, C. W., Bradley, E. F., Godfrey, J. S., Wick, G. A., Edson, J. B., and Young, G. S.: Cool-skin and warm-layer effects on sea surface temperature, *Journal of Geophysical Research: Oceans*, 101, 1295–1308, doi:10.1029/95JC03190, 1996a.
- Fairall, C. W., Bradley, E. F., Rogers, D. P., Edson, J. B., and Young, G. S.: Bulk parameterization of air-sea fluxes for Tropical Ocean-Global Atmosphere Coupled-Ocean Atmosphere Response Experiment, *Journal of Geophysical Research: Oceans*, 101(C2), 3747–3764, 15 doi:10.1029/95JC03205, 1996b.
- Ferrari, R.: A frontal challenge for climate models., *Science*, 332, 316–317, doi:10.1126/science.1203632, 2011.
- Fox-Kemper, B., Ferrari, R., and Hallberg, R.: Parameterization of Mixed Layer Eddies. Part I: Theory and Diagnosis, *Journal of Physical Oceanography*, 38, 1145–1165, doi:10.1175/2007JPO3792.1, 2008.
- Friederich, G. E., Ledesma, J., Ulloa, O., and Chavez, F. P.: Air-sea carbon dioxide fluxes in the coastal southeastern tropical Pacific, *Progress in Oceanography*, 79(2-4), 156–166, doi:10.1016/j.pocean.2008.10.001, 2008.
- 20 Garratt, J. R.: Review of Drag Coefficients over Oceans and Continents, *Monthly Weather Review*, 105, 915–929, doi:10.1175/1520-0493(1977)105<0915:RODCOO>2.0.CO;2, 1977.
- Gruber, N.: Ocean biogeochemistry: Carbon at the coastal interface, *Nature*, 517, 148–149, doi:10.1038/nature14082, 2015.
- Haine, T. W. N. and Marshall, J.: Gravitational, Symmetric, and Baroclinic Instability of the Ocean Mixed Layer, *Journal of Physical Oceanography*, 28, 634–658, doi:10.1175/1520-0485(1998)028<0634:GSABIO>2.0.CO;2, 1998.
- 25 Kao, T. W., Park, C., and Pao, H.-P.: Buoyant surface discharge and small-scale oceanic fronts: A numerical study, *Journal of Geophysical Research*, 82, 1747–1752, doi:10.1029/JC082i012p01747, 1977.
- Körtzinger, A., Mintrop, L., Wallace, D. W., Johnson, K. M., Neill, C., Tilbrook, B., Towler, P., Inoue, H. Y., Ishii, M., Shaffer, G., et al.: The international at-sea intercomparison of *f*CO₂ systems during the R/V Meteor Cruise 36/1 in the North Atlantic Ocean, *Marine Chemistry*, 30 72, 171–192, 2000.
- Landschützer, P., Gruber, N., and C. E. Bakker, D.: An updated observation-based global monthly gridded sea surface pCO₂ and air-sea CO₂ flux product from 1982 through 2015 and its monthly climatology (NCEI Accession 0160558). Version 2.2. NOAA National Centers for Environmental Information. Dataset. [2017-07-11], 2017.
- Lapeyre, G. and Klein, P.: Impact of the small-scale elongated filaments on the oceanic vertical pump, *Journal of Marine Research*, 64, 35 835–851, doi:10.1357/002224006779698369, 2006.
- Laruelle, G. G., Lauerwald, R., Pfeil, B., and Regnier, P.: Regionalized global budget of the CO₂ exchange at the air-water interface in continental shelf seas, *Global Biogeochemical Cycles*, 28, 1199–1214, doi:10.1002/2014GB004832, 2014.

- Lefèvre, N. and Merlivat, L.: Carbon and oxygen net community production in the eastern tropical Atlantic estimated from a moored buoy, *Global biogeochemical cycles*, 26, 2012.
- Lefèvre, N., Guillot, A., Beaumont, L., and Danguy, T.: Variability of $f\text{CO}_2$ in the Eastern Tropical Atlantic from a moored buoy, *Journal of Geophysical Research: Oceans*, 113, 2008.
- 5 Lévy, M., Ferrari, R., Franks, P. J. S., Martin, A. P., and Rivière, P.: Bringing physics to life at the submesoscale, *Geophysical Research Letters*, 39, doi:10.1029/2012GL052756, 2012.
- Loginova, A. N., Thomsen, S., and Engel, A.: Chromophoric and fluorescent dissolved organic matter in and above the oxygen minimum zone off Peru, *Journal of Geophysical Research: Oceans*, 121, 7973–7990, doi:10.1002/2016JC011906, 2016.
- Mahadevan, A., Lévy, M., and Mémery, L.: Mesoscale variability of sea surface pCO_2 : What does it respond to?, *Global Biogeochemical Cycles*, 18, GB1017, doi:10.1029/2003GB002102, 2004.
- Mahadevan, A., Tandon, A., and Ferrari, R.: Rapid changes in mixed layer stratification driven by submesoscale instabilities and winds, *Journal of Geophysical Research*, 115, C03 017, doi:10.1029/2008JC005203, 2010.
- McWilliams, J. C., Colas, F., and Molemaker, M. J.: Cold filamentary intensification and oceanic surface convergence lines, *Geophysical Research Letters*, 36, L18 602, doi:10.1029/2009GL039402, 2009.
- 15 Merlivat, L., Gonzalez Davila, M., Caniaux, G., Boutin, J., and Reverdin, G.: Mesoscale and diel to monthly variability of CO_2 and carbon fluxes at the ocean surface in the northeastern Atlantic, *Journal of Geophysical Research*, 114, C03 010, doi:10.1029/2007JC004657, 2009.
- Meyer, J., Löscher, C. R., Lavik, G., and Riebesell, U.: Mechanisms of P^* Reduction in the Eastern Tropical South Pacific, *Frontiers in Marine Science*, 4, 1, doi:10.3389/fmars.2017.00001, 2017.
- 20 Nash, J. D. and Moum, J. N.: River plumes as a source of large-amplitude internal waves in the coastal ocean, *Nature*, 437, 400–403, doi:10.1038/nature03936, 2005.
- Nightingale, P. D., Malin, G., Law, C. S., Watson, A. J., Liss, P. S., Liddicoat, M. I., Boutin, J., and Upstill-Goddard, R. C.: In situ evaluation of air-sea gas exchange parameterizations using novel conservative and volatile tracers, *Global Biogeochemical Cycles*, 14(1), 373–387, doi:10.1029/1999GB900091, 2000.
- 25 Ohman, M. D., Rudnick, D. L., Chekalyuk, A., Davis, R. E., Feely, R. A., Kahru, M., Jim, H.-J., Landry, M. R., Martz, T. R., Sabine, C. L., and Send, U.: Autonomous ocean measurements in the California Current Ecosystem, *Oceanography*, 26, 18–25, 2013.
- Payne, R. E.: Albedo of the Sea Surface, *Journal of the Atmospheric Sciences*, 29, 959–970, doi:10.1175/1520-0469(1972)029<0959:AOTSS>2.0.CO;2, 1972.
- Peltier, W. R. and Caulfield, C. P.: Mixing efficiency in stratified shear flows, *Annual Review of Fluid Mechanics*, 35, 135–167, doi:10.1146/annurev.fluid.35.101101.161144, 2003.
- 30 Penven, P., Echevin, V., Pasapera, J., Colas, F., and Tam, J.: Average circulation, seasonal cycle, and mesoscale dynamics of the Peru Current System: A modeling approach, *Journal of Geophysical Research*, 110, C10 021, doi:10.1029/2005JC002945, <http://doi.wiley.com/10.1029/2005JC002945>, 2005.
- Pierrot, D., Neill, C., Sullivan, K., Castle, R., Wanninkhof, R., Lüger, H., Johannessen, T., Olsen, A., Feely, R. A., and Cosca, C. E.: Recommendations for autonomous underway pCO_2 measuring systems and data-reduction routines, *Deep Sea Research Part II: Topical Studies in Oceanography*, 56, 512–522, 2009.
- Pietri, A., Echevin, V., Testor, P., Chaigneau, A., Mortier, L., Grados, C., and Albert, A.: Impact of a coastal-trapped wave on the near-coastal circulation of the Peru upwelling system from glider data, *Journal of Geophysical Research: Oceans*, 119, 2109–2120, 2014.

- Ramachandran, S., Tandon, A., and Mahadevan, A.: Enhancement in vertical fluxes at a front by mesoscale-submesoscale coupling, *Journal of Geophysical Research: Oceans*, 119, 8495–8511, doi:10.1002/2014JC010211, 2014.
- Resplandy, L., Lévy, M., D’Ovidio, F., and Merlivat, L.: Impact of submesoscale variability in estimating the air-sea CO₂ exchange: Results from a model study of the POMME experiment, *Global Biogeochemical Cycles*, 23, GB1017, doi:10.1029/2008GB003239, 2009.
- 5 Rudnick, D. L.: On the skewness of vorticity in the upper ocean, *Geophysical Research Letters*, 28(10), 2045–2048, doi:10.1029/2000GL012265, 2001.
- Shin, J., Dalziel, S., and Linden, P.: Gravity currents produced by lock exchange, *Journal of Fluid Mechanics*, 521, 1–34, 2004.
- Smith, S. D.: Coefficients for sea surface wind stress, heat flux, and wind profiles as a function of wind speed and temperature, *Journal of Geophysical Research: Oceans*, 93(C12), 15 467–15 472, doi:10.1029/JC093iC12p15467, 1988.
- 10 Takahashi, T., Sutherland, S. C., Wanninkhof, R., Sweeney, C., Feely, R. A., Chipman, D. W., Hales, B., Friederich, G., Chavez, F., Sabine, C., Watson, A., Bakker, D. C., Schuster, U., Metzl, N., Yoshikawa-Inoue, H., Ishii, M., Midorikawa, T., Nojiri, Y., Körtzinger, A., Steinhoff, T., Hoppema, M., Olafsson, J., Arnarson, T. S., Tilbrook, B., Johannessen, T., Olsen, A., Bellerby, R., Wong, C., Delille, B., Bates, N., and de Baar, H. J.: Climatological mean and decadal change in surface ocean pCO₂, and net sea–air CO₂ flux over the global oceans, *Deep Sea Research Part II*, 56, 554 – 577, doi:10.1016/j.dsr2.2008.12.009, 2009.
- 15 Takahashi, T., Sutherland, S. C., Chipman, D. W., Goddard, J. G., Newberger, T., and Sweeney, C.: Climatological distributions of pH, pCO₂, total CO₂, alkalinity, and CaCO₃ saturation in the global surface ocean. ORNL/CDIAC-160, NDP-094., Carbon Dioxide Information Analysis Center, Oak Ridge National Laboratory, U.S. Department of Energy, Oak Ridge, Tennessee, doi:10.3334/CDIAC/OTG.NDP094, 2014.
- Taylor, J. R. and Ferrari, R.: Ocean fronts trigger high latitude phytoplankton blooms, *Geophysical Research Letters*, 38, L23 601, doi:10.1029/2011GL049312, 2011.
- 20 Thomas, L. N. and Lee, C. M.: Intensification of Ocean Fronts by Down-Front Winds, *Journal of Physical Oceanography*, 35, 1086–1102, doi:10.1175/JPO2737.1, 2005.
- Thomas, L. N., Tandon, A., and Mahadevan, A.: Submesoscale Processes and Dynamics, in: *Ocean Modeling in an Eddying Regime*, edited by Hecht, M. W. and Hasumi, H., American Geophysical Union, Washington, D. C., doi:10.1029/177GM04, 2008.
- 25 Thomsen, S., Eden, C., and Czeschel, L.: Stability Analysis of the Labrador Current, *Journal of Physical Oceanography*, 44, 445–463, doi:10.1175/JPO-D-13-0121.1, 2014.
- Thomsen, S., Kanzow, T., Colas, F., Echevin, V., Krahnmann, G., and Engel, A.: Do submesoscale frontal processes ventilate the oxygen minimum zone off Peru?, *Geophysical Research Letters*, 43, 8133–8142, doi:10.1002/2016GL070548, 2016a.
- Thomsen, S., Kanzow, T., Krahnmann, G., Greatbatch, R. J., Dengler, M., and Lavik, G.: The formation of a subsurface anticyclonic eddy 30 in the Peru-Chile Undercurrent and its impact on the near-coastal salinity, oxygen, and nutrient distributions, *Journal of Geophysical Research: Oceans*, 121, 476–501, doi:10.1002/2015JC010878, 2016b.
- Ungarish, M. and Huppert, H. E.: On gravity currents propagating at the base of a stratified ambient, *Journal of Fluid Mechanics*, 458, 283–301, doi:10.1017/S0022112002007978, 2002.
- Walter, R. K., Stastna, M., Woodson, C. B., and Monismith, S. G.: Observations of nonlinear internal waves at a persistent coastal upwelling 35 front, *Continental Shelf Research*, 117, 100–117, doi:10.1016/j.csr.2016.02.007, 2016.
- Wanninkhof, R.: Relationship between wind speed and gas exchange over the ocean, *Journal of Geophysical Research: Oceans*, 97, 7373–7382, doi:10.1029/92JC00188, 1992.

- Wanninkhof, R.: Relationship between wind speed and gas exchange over the ocean revisited, *Limnology and Oceanography: Methods*, 12, 351–362, doi:10.4319/lom.2014.12.351, 2014.
- Weiss, R. F.: Carbon dioxide in water and seawater: the solubility of a non-ideal gas, *Marine Chemistry*, 2, 203–215, doi:10.1016/0304-4203(74)90015-2, 1974.
- 5 Weiss, R. F. and Price, B. A.: Nitrous oxide solubility in water and seawater, *Marine Chemistry*, 8, 347–359, doi:10.1016/0304-4203(80)90024-9, 1980.
- White, B. L. and Helfrich, K. R.: Rapid gravitational adjustment of horizontal shear flows, *Journal of Fluid Mechanics*, 721, 86–117, doi:10.1017/jfm.2013.41, 2013.

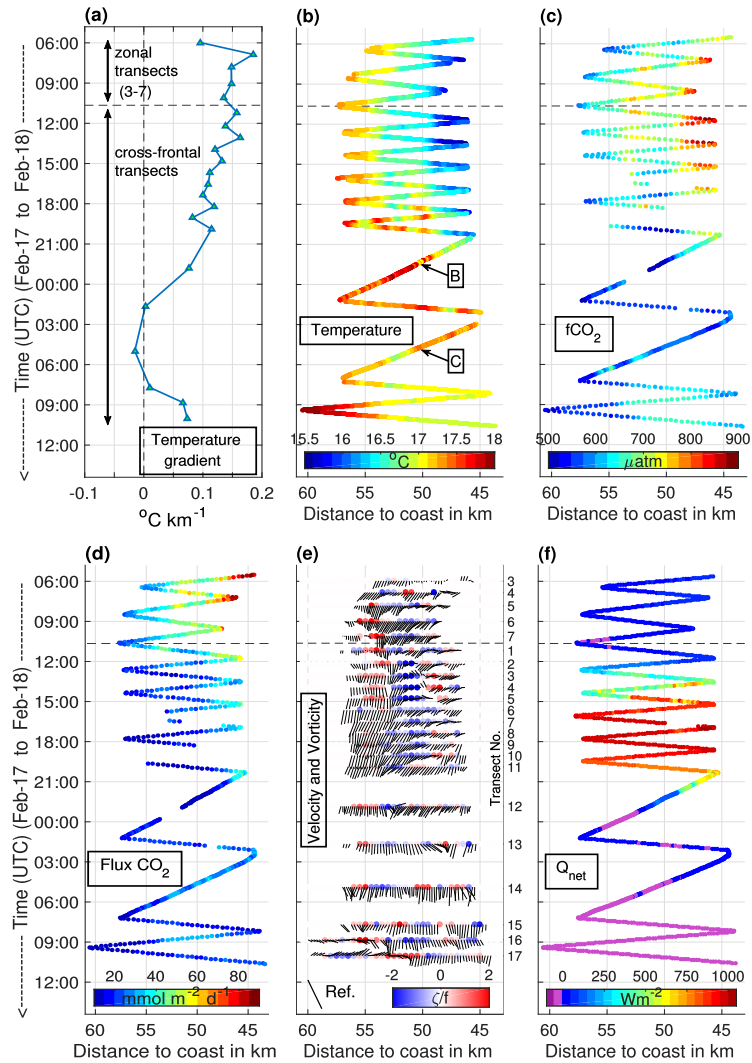


Figure 6. Hovmoeller diagrams of the cross-frontal surface temperature gradient (a), underway surface temperatures (b), surface $f\text{CO}_2$ (c), ocean-atmosphere CO_2 fluxes (d), mean current velocities in the upper 40 m (black lines) and vorticity (colored circles) (e) and diabatic surface heating (f) for the last five zonal transects and the subsequent 17 cross-frontal transects. The horizontal dashed line indicates the transition from zonal transects to repeated cross-frontal transects. Temperature gradients in (a) are calculated using a linear fit to the surface temperature transect shown in (b). In (b) the position of transects B and C is indicated. The vorticity of the vertically averaged velocity in (e) is calculated as $\zeta = \partial u_{al} / \partial y$ (Rudnick, 2001), where u_{al} is the along-front velocity and y is the cross-frontal distance, taken to be 2 km, comparable to the mixed layer deformation radius. The reference arrow in the bottom left corner anchored at 60 km from the coast indicates a flow with 0.3 m s^{-1} in the onshore (cross-front) and 0.3 m s^{-1} in the southward-poleward along-front direction. The vorticity is normalized by the Coriolis parameter to give a proxy for the Rossby number. Velocity and vorticity are plotted at the time mean for each transect. Time is given in UTC.

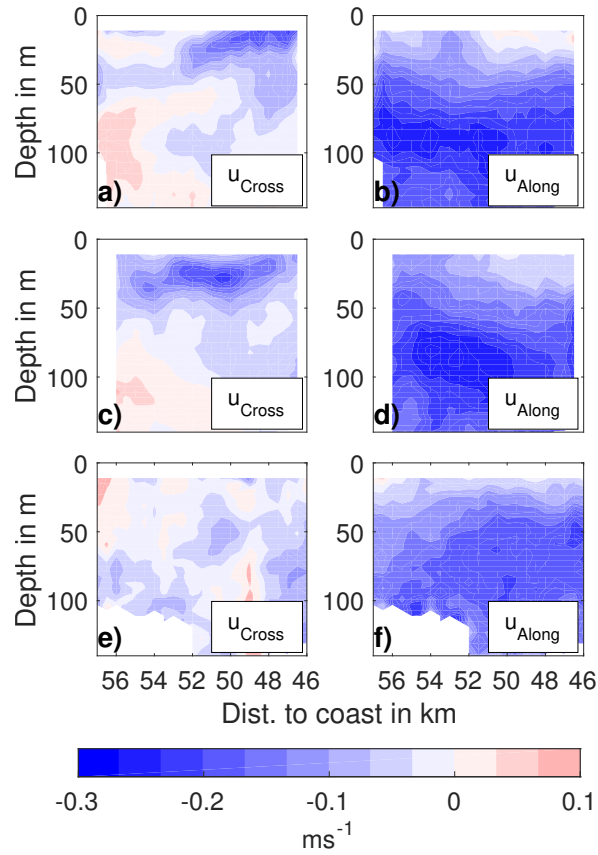


Figure 7. Mean cross- and along-front current velocities for cross-frontal transects 1-6 in (a) and (b), 7-11 in (c) and (d) and 12-17 in (e) and (f). Currents are horizontally binned onto a 500 m grid and subsequently averaged.

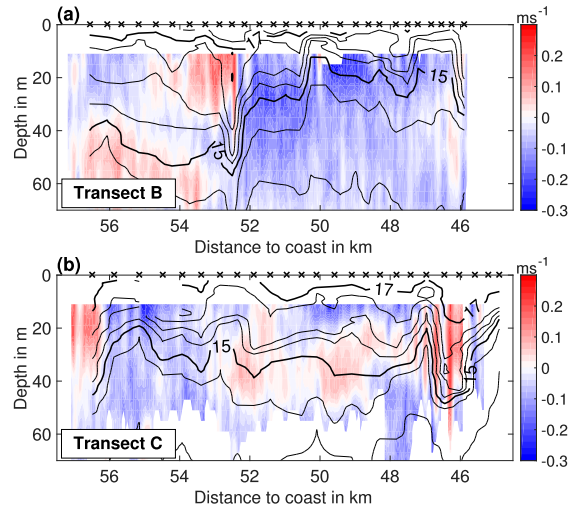


Figure 8. Temperature (black contour lines) and cross-front velocity (color-coded) for Transects B (a) and C (b) conducted as the 12th and 14th cross-frontal transect, starting on February 17 21:00 and February 18 03:00, respectively. Black crosses show the location of the temperature profiles from the microstructure probe. For both transects the ship moved away from the coast (right to left).

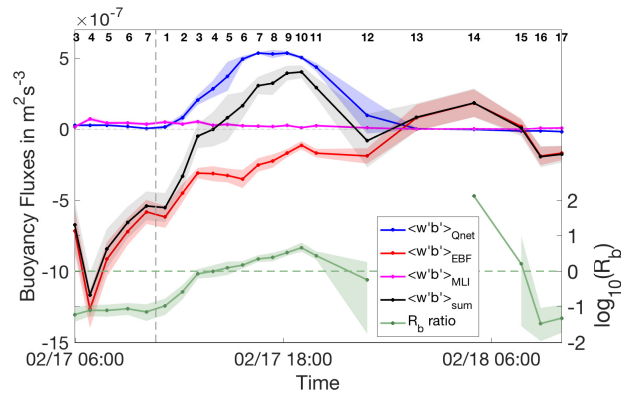


Figure 9. Vertical buoyancy fluxes associated with surface heating (blue), Ekman transport (red) and mixed layer instabilities (magenta). The uncertainty range for shaded areas around the Ekman buoyancy fluxes flux (EBF) and the buoyancy fluxes flux associated with mixed layer instabilities (MLI) is-are accounting for uncertainties in the surface salinity gradient (see text for more details). The shaded uncertainty range for vertical buoyancy fluxes due to surface heating is given as one standard deviation obtained from sectional averaging. The sum of the three processes is given by the black line. For The uncertainty is given as the maximum error resulting from the three processes. The R_b ratio the errors (green) and its uncertainty are omitted treated similarly. For cross-frontal transect 13 and 14 no R_b value or error can be stated due to the vanishing denominator in the definition of R_b . $\log_{10}(R_b) > 0$ points towards a net restratification, while $\log_{10}(R_b) < 0$ indicates a destabilization of the water column. For calculation details of all quantities see text. Time is given in UTC. The small black numbers on top indicate the respective zonal or cross-frontal transect number.

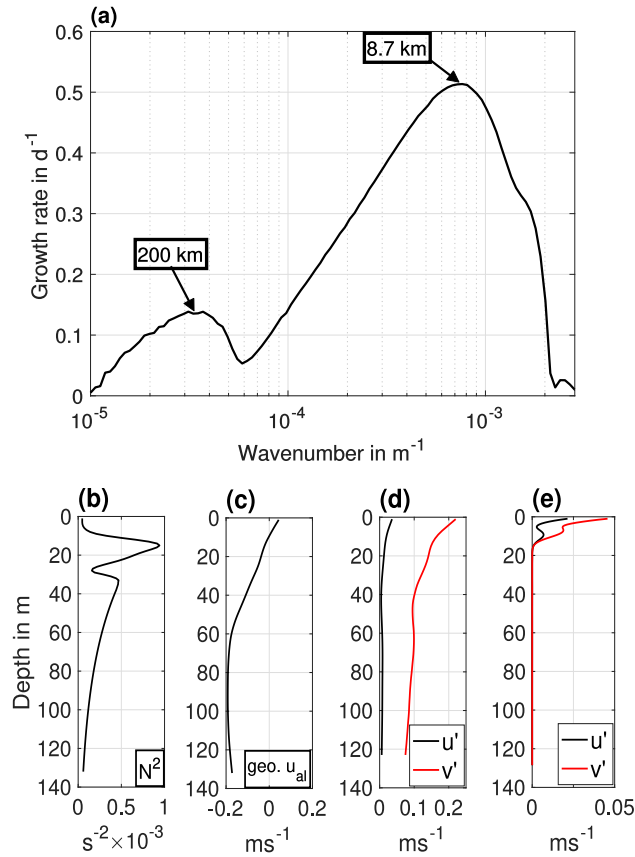


Figure 10. (a) Initial growth rate of baroclinic instabilities obtained from linear stability analysis, applied to the frontal state during the CTD section (transect A). The local maxima of the growth rate are labeled by their corresponding length scale in km. The smoothed stratification and geostrophic along-frontal velocity profiles used as input the background state, are shown in panels (b) and (c). A deep mode at large horizontal scales (200 km) and a shallow mode, associated with mixed layer instabilities and short horizontal length scales (8.7 km) are present. The corresponding anomalies for the cross-front (u) and along-front (v) velocities are shown in panels (d) and (e) for the deep and shallow modes, respectively.